

2014

X-ray radiography and fluorescence for liquid distribution and mixing measurements in impinging jet sprays

Benjamin Robert Halls
Iowa State University

Follow this and additional works at: <https://lib.dr.iastate.edu/etd>

 Part of the [Mechanical Engineering Commons](#)

Recommended Citation

Halls, Benjamin Robert, "X-ray radiography and fluorescence for liquid distribution and mixing measurements in impinging jet sprays" (2014). *Graduate Theses and Dissertations*. 14156.
<https://lib.dr.iastate.edu/etd/14156>

This Dissertation is brought to you for free and open access by the Iowa State University Capstones, Theses and Dissertations at Iowa State University Digital Repository. It has been accepted for inclusion in Graduate Theses and Dissertations by an authorized administrator of Iowa State University Digital Repository. For more information, please contact digirep@iastate.edu.

**X-ray radiography and fluorescence for liquid distribution
and mixing measurements in impinging jet sprays**

by

Benjamin Robert Halls

A dissertation submitted to the graduate faculty
in partial fulfillment of the requirements for the degree of

DOCTOR OF PHILOSOPHY

Major: Mechanical Engineering

Program of Study Committee:
Terrence R. Meyer, Major Professor
Theodore J. Heindel
Song Zhang
Song-Charng Kong
Hui Hu

Iowa State University

Ames, Iowa

2014

Copyright © Benjamin Robert Halls, 2014. All rights reserved.

DEDICATION

I dedicate this dissertation to my Aunt Karen. After her passing I learned how much she would brag about me to her friends and other relatives about my academic success. Now I have the chance to brag about her. She always loved and inspired everyone in her life including me. She encouraged me to do my best in school and out in the world. Her adventurous spirit and numerous travels motivated me to join Engineers Without Borders and travel abroad.

TABLE OF CONTENTS

	Page
NOMENCLATURE	iv
ACKNOWLEDGEMENTS	vi
ABSTRACT	viii
CHAPTER 1 INTRODUCTION	1
Chapter 1 Background	1
Chapter 1 Literature Review	12
Chapter 1 Proposed Research	22
CHAPTER 2 EXPERIMENTAL FACILITIES	26
Chapter 2 Mass Distribution	26
Chapter 2 Liquid Mixing	43
Chapter 2 Spray System	51
CHAPTER 3 RESULTS AND DISCUSSION	57
Chapter 3 Mass Distribution	57
Chapter 3 Liquid Mixing	93
CHAPTER 4 UNCERTAINTY ANALYSIS	130
Chapter 4 Uncertainty Propagation	130
Chapter 4 Sources of Uncertainty	132
CHAPTER 5 CONCLUSIONS	140
Chapter 5 Mass Distribution	140
Chapter 5 Liquid Mixing	146
REFERENCES	151
APPENDIX A LIQUID MIXING STUDY	161
APPENDIX B SPRAY SYSTEM STANDARD OPERATING PROCEDURE....	181

NOMENCLATURE

2θ	impingement angle
α	attenuation coefficient
γ	surface tension
Φ	mixing factor
ψ	detector response function
ν	kinematic viscosity
τ	transmission
A	Attenuation of incident beam
APS	Advanced Photon Source
b	local mixture ratio
B	total mixture ratio
EPL	Equivalent Path Length
F_{salt}	Fluorescence signal for each salt
FJ	free jet length (non-dimensional)
FWHM	Full Width Half Max
$h\nu$	photon energy
I	intensity
I_0	incident intensity
m, b	polynomial coefficients
m	local mass
M	total mass

R_{salt}	Reabsorption for each salt
Re	Reynolds number
RPL	Reabsorption Path Length
SNR	Signal to Noise Ratio
w	local mass flow rate
W	global mass flow rate
We	Weber number
Z	atomic number

ACKNOWLEDGEMENTS

I would like to thank my parents for all of the love and support they provided along the way. They would let me try anything and never worried if I would fail. My sister worried that I would fail, but would always wait to tell me until afterwards.

I thank my advisor, Dr. Terry Meyer, for his guidance and the experience of working in his lab as a research assistant and the opportunities he provided me to travel to many conferences. I am particularly thankful for the summer internship he helped me arrange at Wright-Patterson Air Force Base; it is now where I am starting my career. I am appreciative for my advisory committee: Dr. Heindel, for use of his laboratory and help with x-ray imaging; Dr. Zhang, for his collaboration on structured light measurements; and Dr. Kong and Dr. Hu for their help in steering my research to gain insight in diagnostic methods as well as fundamental fluid mechanics.

I would also like to thank all of my teachers, coaches, and mentors from grade school to high school for their support, advice, and encouragement along the way. Mr. Jorgensen encouraged me to attend a summer camp on Mechanical Engineering in middle school. Dr. Buege pushed all of his students especially me to think critically inside and outside the class room. Mr. Wilauer was my favorite teacher; in one phrase - he gave me the answer to my confidence. And of course Ms. P, who told me not to pursue a career in science but rather one in philosophy... I got half that message.

Throughout the numerous years I have spent in college and graduate school, I had the opportunity to work for and with some pretty great people. Professor Kraemer was my undergraduate advisor and was always available for professional assistance, even after I

graduated. Mr. Andrasko taught me about working as an engineer and keeping the management happy. Dr. Coil gave me my first experiences in spray research and thought I should pursue graduate school. Dr. Kastengren's tireless efforts at the APS really helped shape my measurements and success as a student. Dr. Musclus and Sandia National Laboratory awarded me a week long internship on measurement uncertainty. Dr. Roy and Dr. Gord gave me the opportunity to work at the Air Force Research Laboratory as a summer intern and I look forward to continue working alongside both of them.

The graduate students, Dr. Joe Miller, Chloe Dedic, Mark Ceconi, Harish Sumbramani, Jordan Tiarks, Patrick Sanderson, Dan Stoecklein, Daniel Diaz, Dr. Praveen Kumar, Dr. Miao Li, and post-docs Dr. James Michael and Dr. Prabhakar Venkateswaran, in our lab helped me with many technical and non-technical issues. I am grateful for their friendship and support. I am also thankful for the undergraduates and the assistance they provided in my lab. A special thanks to any of the aforementioned that were so lucky as to travel to the APS with me.

I owe a great deal of gratitude to the Army Research Office and the Air Force Research Laboratory for the support they provided through funding, and review meetings to help guide my work. Purdue University helped a lot with technical support and hardware for the spray systems.

ABSTRACT

The merging of unstable liquid jets, approaching with high momentum, results in atomization and liquid mixing within a rapidly deforming impingement zone. The complex geometry and high index-of-refraction gradients that occur near the point of impingement present a particularly difficult environment for optical interrogation. X-ray based diagnostics are performed to determine the liquid mass distribution and liquid mixing in the spray utilizing x-ray attenuation and x-ray fluorescence, respectively. Radiography and computed tomography are employed to determine the mass distribution through single-shot, high-speed, and three-dimensional attenuation measurements using broadband x-ray tube sources. The variable attenuation coefficients are compared to a model to account for beam hardening in the x-ray energy spectrum. The accuracy and precision of the techniques are evaluated through a comparison with data from a narrowband synchrotron-based x-ray source. The Advanced Photon Source (APS) at Argonne National Laboratory is used to generate high-fidelity time-averaged and time-resolved point-wise data for the evaluation of the broadband tube sources. X-ray fluorescence measurements quantify the mixing in the impinging jet spray using the APS. Fluorescent tracers are tailored to allow for the direct measurement of the mass distribution of each fluid and thus mixing. The advantages, limitations, and optimization of each technique are discussed, and recommendations for improving performance are presented. A parametric study is performed to determine the effects of spray geometry, flow conditions, and fluid properties, including viscoelasticity in non-Newtonian fluids.

CHAPTER I

INTRODUCTION

Background

The spray breakup process of Newtonian and non-Newtonian liquids into smaller ligaments and droplets is an integral part of many applications in several industries. These applications and industries include: spray cooling and powdered metals in the production and processing industries; propellant injection in combustion devices; aerosol drug delivery in medicine; and soil/crop treatment in agriculture (Lefebvre 1981, Ashgriz, 2011, and Meyer 2012). The specific need to understand mass distribution and mixing of fuels and oxidizers to enhance our understanding of combustion is important for many reasons. For example, combustion is responsible for approximately 70% of energy consumption in the United States, and liquid fuels comprise a high percentage of transportation fuels and nearly all of aviation propulsion (Energy Review, 2012 and Epstein, 2012). Liquid fuels are critical because of their availability, energy density, ease of storage, and ease of delivery into the combustion system. Likewise, the delivery of liquid fuels must be carefully designed to address challenges associated with inefficiencies, regulated emissions, and safety concerns. In the case of gas turbines and rocket engines, instabilities can inhibit potential increases in performance and efficiency. A thorough understanding of the spray process can reveal sources of inefficiency and instability as well as help to validate predictive models to aid in the design of future combustion devices.

The spray process is fundamentally unsteady and spans a wide range of spatial and temporal scales. Spray behavior is also coupled dynamically with the local flow field such

that direct quantitative evaluation becomes difficult. This complexity has prevented the development of predictive models and necessitated continued advancement in methods for experimental investigation. Sprays have been studied for many years, and the knowledge of sprays depends upon the capabilities of advanced spray diagnostic techniques. The use of novel diagnostics has led to a deeper understanding of sprays and allowed for more effective spray devices and spray models with increased fidelity. Once validated through experiments, spray models can be utilized to test numerous spray configurations to aid in the design process of new spray systems.

Despite significant progress, the highly turbulent combustion chamber at high temperatures, very high pressures, and potentially dangerous nature of strong oxidizers and fuels poses a difficult set of challenges to investigating spray processes (Kuo, 1995; Sutton and Biblarz, 2001; Yang et al., 2004; Yang and Anderson, 1995). Liquid propulsion devices can be simplified to two main processes: spray injection and breakup followed by combustion and gas acceleration. The injector can be isolated from the combustion chamber and a simplified spray breakup process can be investigated, thereby mitigating many of the aforementioned issues and yielding relevant results. Previous work has shown that these measurements in the absence of combustion but at high temperatures and high pressures are still relevant to understanding the fundamental processes.

Once separating the spray injection and breakup process from combustion and gas acceleration, non-evasive diagnostics can be more easily implemented to probe the spray without perturbing the flowfield and changing the underlying phenomena. Further development of these diagnostic tools will help reveal key phenomena, including spray dynamics, mass distribution, and fuel-oxidizer mixing in sprays leading to combustion. In

propulsion applications, recent studies of aerated jets, jets in crossflow, and supercritical injection have employed various optical imaging techniques, including shadowgraphy, Mie scattering, holography, laser-induced fluorescence, structured illumination, optical connectivity, and ballistic imaging (e.g., Berrocal et al., 2012; Charalampous et al., 2008; Jung et al., 2003; Lin et al., 2001; Linne et al., 2005; Meyer et al., 2010; Sallam et al., 2006; Santangelo and Sojka, 1994). These techniques have been used to reveal valuable information on liquid breakup processes, although measurement of the liquid mass distribution can be impaired by the complex optical interaction with liquid structures of varying size, shape, and number density. Techniques based on phase Doppler interferometry (Bachalo, 1980) or diffraction (Dobbins et al., 1963) can provide droplet velocity and size distributions, which can then be used to infer liquid mass distributions; however, an alternative approach is required in regions that are dominated by a significant fraction of non-spherical liquid structures. Hence, while optical techniques provide valuable information under a wide range of spray conditions, x-ray radiography may be the only practical method of measuring the liquid mass distribution in otherwise difficult sprays (Linne, 2013).

Unlike visible light, which is strongly scattered from aerosols, droplets, and other liquid structures, the interaction of low-energy (~ 10 keV) x-rays with sprays is primarily through absorption and weak scattering. This greatly simplifies the analysis as the attenuation signal can be related to the liquid mass density in the path of the x-rays with minimal sensitivity to the droplet size, shape, and number density. This gives a greater scope for quantitative measurements of liquid mass distribution with x-ray techniques than with most other optical techniques. Much of the recent work in advancing x-ray spray imaging has taken place at the Advanced Photon Source (APS) located at the Argonne National

Laboratory. Synchrotron x-ray sources such as the APS provide a highly-collimated, tunable, low-energy x-ray beam with sufficient flux for radiography to be performed over a wide range of liquid path lengths. This has yielded time-resolved, highly accurate attenuation measurements under a variety of spray conditions (e.g., Cai et al., 2003; Kastengren and Powell, 2007; Lin et al., 2011; MacPhee et al., 2002; Poola et al., 2000; Powell et al., 2000; Qun et al., 2007; Schumaker et al., 2012).

In addition to minimizing the effects of x-ray scattering through the use of low-energy x-rays, the narrowband nature of the APS x-rays allows them to propagate through liquid media without significant deviation in the attenuation coefficient. The synchrotron differs from conventional tube sources that produce x-rays with higher energies (~100 keV) that can increase scattering and reduce image contrast. In general, the scattering and absorption of x-rays scale as the inverse square and inverse cube of photon energy, respectively, leading to increased scattering contributions at higher photon energy. Furthermore, the broadband nature of x-rays from tube sources may induce the preferential attenuation of x-rays within certain photon energy ranges along the line of sight, causing so-called spectral beam hardening for long path lengths. Despite these challenges, many sprays of practical interest have path lengths of millimeters or less, and it may be possible to minimize or avoid the effects of multiple scattering and preferential attenuation of x-rays for various photon energies.

It is of interest, therefore, to determine if under certain conditions a broadband, high-energy x-ray tube source can reproduce quantitative data on liquid mass distributions as determined from a narrowband, low-energy x-ray source. Tube sources can be more readily employed in various laboratories for studying propulsion and other industrial applications of

sprays because they are relatively compact and require a much smaller capital investment. They are also readily employed for time-averaged, two-dimensional radiography and three-dimensional computed tomography (CT) (Meyer et al., 2010). Meyer et al. (2008, 2010), for example, showed that the broadband x-ray attenuation coefficient through 10 mm of water seeded with potassium iodide (KI) as a contrast enhancing agent, increases linearly up to KI concentrations of 15% by mass, indicating minimal influence from the effects of beam hardening. To the best of the author's knowledge, however, a direct validation of liquid mass distributions (2-D or 3-D) measured using broadband x-ray sources has not yet been presented for atomizing sprays (Heindel, 2011). Application of polychromatic sources for investigation of instantaneous or time-averaged spray structure has been presented by a number of researchers, (Woodward et al. 1995, Birk et al. 2003, Meyer et al. 2008, 2010, Halls 2012, 2012, 2014). Continuous wave tube sources have also been used with high-speed linear sensors and intensified high-speed cameras by Char et al. (1989), Lim (2013), and Halls et al. (2014, 2014).

Radiography utilizing flash tube sources has been used to show similar quantitative spray behavior. The broadband spectrum of tube sources results in higher energy photons (~100 keV) which increase photon scattering and reduces attenuation decreasing image contrast. In general, the absorption and scattering of x-rays scale as the inverse cube and inverse square of photon energy, respectively. The broad spectrum leads to a wide range of mass attenuation coefficients. The preferential attenuation of low energy photons, or spectral beam hardening, shifts the output spectrum and can require the use of a variable attenuation coefficient. Application of polychromatic sources for investigation of instantaneous spray

structure has been presented by a number of researchers, including (Birk et al., 2003; Robert et al., 2010; Halls et al., 2013, 2013).

While x-ray tube sources offer a laboratory scale approach to high speed attenuation measurements and have been proven useful in radiography, stereography, and computed tomography, more work is need to account for spectral beam hardening to achieve quantitative results. Moreover, low path lengths can make it difficult to achieve high contrast single-shot and high-speed imaging of liquid sprays, especially for continuous x-ray sources in which the photon flux is limited by the exposure time of the detection system. For example, impinging-jet injectors used to mix fuels and oxidizers in rocket propulsion can form liquid sheets as thin as 10 μm , and interrogating such thin features with x-rays requires sufficient absorption to achieve the required contrast between the liquid sheet and surrounding air. Hence, additional work is required to investigate the ability of broadband x-ray sources to accurately measure the mass distribution in such sprays.

Gamma ray densitometry has also been applied to multiphase flow measurement and spray measurement (Ruff and Faeth, 1989).

In addition to studying primary breakup processes, it is also important in the case of liquid fuels and oxidizers to investigate the mixing rate within a very complex optical environment. Prior efforts to measure the mixing of impinging jets have employed techniques such as mechanical patternation (Elverum and Morey in 1959; Somogyi and Feiler, 1959; Hoehn, 1972; Nurick, 1976; and Ashgriz et al., 2001) and laser-induced fluorescence (McDonnell et al., 1999; and Yuan and Huang, 2012). These measurements were all made significantly below the impingement point, where gas initiation and chemical reactions would originate in impinging jets of hypergolic propellants. Three mixing regimes

have been previously identified from these downstream measurements. In reflective mixing, the jets do not have sufficient momentum to coalesce, and their trajectories do not cross. At higher momentum conditions, transmissive mixing occurs because of the dual effect of high impact velocity and the presence of jet instabilities that allow ligaments from each liquid to pass through the opposing liquid to the opposite side of the liquid sheet. This occurs through jet fragmentation within the impingement zone. At sufficiently high jet momenta, this regime may reduce initial mixing because the liquids separate after impact, but an increase in post atomization turbulent dispersion typically leads to improved overall mixing. Residing between reflective and transmissive mixing is a thoroughly mixed condition (Rupe, 1953 and Ashgriz et al., 2001). Because of the difficulty in making direct observations near the impingement point, these mixing phenomena have been inferred from measurements in the droplet field after jet merging and primary breakup have taken place. Mechanical patternators are ineffective in regions where the jets have not fully broken up into droplets, and laser induced fluorescence and attenuation techniques suffer from complex refraction patterns at the highly deformed phase interfaces that develop near the impingement point. This ultimately limits fundamental understanding and detailed model validation of the unsteady mixing process for these and other types of jet mixing applications.

To study the mixing of liquid jets, therefore, is difficult to achieve with optical and mechanical techniques, and additional diagnostics development work is needed. A possible approach, proposed here, is to utilize a narrowband source to excite specific atoms using high photon flux and to differentiate individual liquid streams with the subsequent fluorescence photons. Previous efforts at the APS have shown the potential for x-ray fluorescence to study gas-phase mixing, as well as distinguish multiple fluids in static mixtures. However, the use

of x-ray fluorescence for studying the mixing within a dynamic fluid system, such as an impinging jet rocket spray, requires further study.

The need for advanced diagnostics is necessary in understanding these phenomena in liquid rocket engines that require the propellants to rapidly mix and atomize while entering the combustion chamber (Kuo, 1995; Sutton and Biblarz, 2001; Yang et al., 2004; Yang and Anderson, 1995). Efficient propellant mixing and atomization results in greater combustion efficiency and thus more compact combustion chambers. Various injection methods exist including liquid-liquid swirl, where two counter swirling liquids meet inside the injector; pintle, where two liquids meet on the outer surface of the injector; and impinging jets, where the two liquids meet at some distance from the injector surface. A specific type of liquid rocket engine is the hypergolic rocket engine. A hypergolic rocket does not require an external ignition source, but relies on the reaction of the fuel and oxidizer to provide the heat for ignition (Sutton and Biblarz, 2001; Yang et al., 2004; Yang and Anderson, 1995). In the case of the hypergolic rockets, impinging liquid jets are the only safe way to inject, mix, and ignite the propellants.

There are several variations of the impinging jet injector. The common variations are the number of jets and whether the jets are like or unlike fluids. If the jets are like fluids, they flow the same fluid through the same size orifice at the same velocity. A simple hypergolic injector may employ an unlike doublet, where a fuel jet and oxidizer jet impinge. The orifice diameter or jet velocity may differ to match momentum, stoichiometry or a compromise of both. In the current study a like-doublet impinging jet injector has been studied to maintain a simple experimental spray.

The like-doublet impinging jet injector has several key characteristics defining the flow behavior. The characteristics include; liquid properties, jet flow dynamics, and impingement angle. The fluid properties of importance are the kinematic viscosity, and surface tension. The jet flow dynamics are controlled by the internal and external flows. The internal flow is determined by the orifice entrance, length, diameter, and liquid velocity. These characteristics define the velocity profile, turbulence, and any potential cavitation bubbles. For the current discussion, the effects of cavitation will be considered to be negligible. The external flow is then dictated by the internal flow at the exit of the orifice and the distance to the impingement zone. Over the course of the fluid flow from the orifice exit to impingement zone the velocity profile relaxes due to the lack of a shear force, the small turbulent structures are dampened, the larger turbulent structures can grow, and the effective jet diameter can increase. When the jets impinge the fluid conserves momentum and spreads in the plane perpendicular to the jets. The impingement angle determines how the two jets will spread upon impingement, at larger angles a wide thin sheet is formed and at smaller angles a narrow thin sheet is formed. The culmination of these characteristics defines the breakup regime.

Impinging jets can undergo several distinct breakup regimes when considering Newtonian fluid properties. They range from a closed rim sheet, to an unstable wavy sheet, and fully developed, depending on Reynolds number. Shown in Figure 1-1 Li and Ashgriz, (2006) describe the regimes for an impingement angle of 60 degrees.

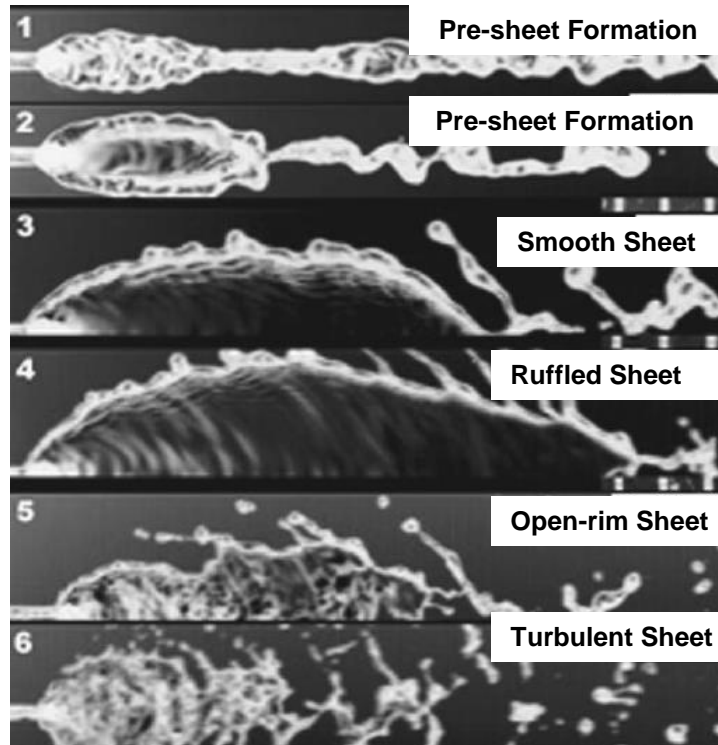


Figure 1-1. Breakup regimes as described by Li and Ashgriz (2006).

At low Reynolds number, the jets impinge and a closed rim spray is formed, the rims of the sheet act as jets and re-impinge generating a cascade of orthogonal sheets that decrease in size until the liquid undergoes large droplet breakup. As the Reynolds number is increased the size of the liquid sheet grows until it becomes too large to dampen instabilities. Weak impact waves form at the impingement zone and the instability disrupts the rims ability to re-impinge. The rim opens and large droplets are formed below the sheet. The instabilities grow with the increase in Reynolds number. The rim becomes less pronounced as the opening widens, and larger more frequent impact waves are present. With further increases in Reynolds number the wavy sheet breakup length decreases until the fully developed regime, in which the only intact liquid structure remains within the impingement zone, from which droplets are ejected.

The breakup regimes can be quite different for non-Newtonian fluids, and particularly gels. Of particular interest in this work is the breakup of gels formed using hydroxypropyl cellulose. The shear thinning behavior of this gel causes a range of Reynolds number to be present in a single spray due to the relationship between shear stress and viscosity. The viscoelastic behavior of the gel gives the fluid a “memory” and can cause a stretch fluid element to spring back. These two phenomena make it quite difficult for the fluid to breakup into droplets and ligaments. To obtain significant breakup of the gelled liquid jets, the velocities must be quite high and driven by pressures that are an order of magnitude higher than that of pure water.

The various breakup regimes of the impinging jet spray make it very interesting from a diagnostics standpoint. The lower Reynolds number regimes exhibit a stable sheet with a thick rim structure that can coalesce or break into large non-spherical droplets downstream; measuring the sheet thickness and non-spherical droplet volumes can be difficult with traditional diagnostics. As the Reynolds number increases the sheet becomes increasingly unstable with impact waves forming at the impingement surface. Making an unperturbed measurement of these waves including their volume, frequency, and velocity would be beneficial understanding phenomena revealed under combusting conditions, for which instabilities may develop. As the Reynolds number is further increased, the liquid sheet recedes towards the impingement point and a dense droplet field forms. Multiply scattered photons can disrupt mass distribution measurements when using optical wavelengths, necessitating use of x-ray based measurements. As revealed in previous work, mixing phenomena can occur at different rates and probably through different mechanisms. Being able to track each fluid from the impingement point through the full breakup of the liquid

sheet would reveal dynamics and increase the understanding of the mixing mechanics and potential combustion performance of impinging jet injectors.

Hence, the current work focuses on advancing the scientific basis for the use of new x-ray based diagnostics to study liquid jet breakup regimes covering a wide range of Reynolds numbers, investigate liquid jet mixing in the near-field of the jet exit and impingement regions, evaluate the effects of non-Newtonian flow physics, and develop an understanding of the controlling non-dimensional parameters. New diagnostics to be investigated include quantitative broadband tube-source x-ray radiography and computed tomography, quantitative instantaneous two-dimensional flash x-ray radiography, high-speed broadband x-ray imaging, and synchrotron x-ray based tracer fluorescence.

Literature Review

Advancements in spray diagnostics and their application to impinging jet sprays have been well documented through the literature. A selection of these articles that pertain or are of particular interest to the current research goals are highlighted and discussed. The research topics of discussion are: optical spray diagnostics; x-ray spray diagnostics, impinging jets, the mass distribution and sheet thickness of impinging jets, mixing within impinging jets, gelled impinging jets, and hypergolic impinging jets.

A myriad of optical and laser based diagnostics have been employed and developed for spray breakup. Techniques based on optical wavelengths can be used to determine droplet properties such as droplet size, velocity, number density, and location. The Malvern technique based on diffraction was coupled with a transmission technique to determine the aggregate size and concentration of droplets in a spray (Dobbins et al., 1963). Phase-Doppler

Interferometry, developed by Bachalo (1980) can be used to determine the droplet size, velocity, and number density at a particular point in the spray. A collimated beam of light can be used to image the first and second derivative of the index of refraction using the Schlieren and shadowgraph techniques. Spray imaging using shadowgraphy and Schlieren is reviewed in a book by G. Settles (2001). Planar laser measurements are made using Mie scatter or fluorescence; the applicability of this technique and the effects of attenuation are discussed by Sick and Stojkovic (2001). Fraunhofer diffraction patterns are used to determine the distance a particle or droplet is from the focal plane in holographic imaging. Focused-image holography has been used to determine the three dimensional position of droplets during spray breakup (Santangelo and Sojka, 1994).

The previously mentioned spray diagnostics are limited by multiply scattered photons and large liquid structures to downstream locations in the spray where primary breakup has already occurred. Outlined in a review paper, Linne (2013) discusses several techniques specifically tailored for the near-field dense region of the spray and suggests that x-ray diagnostics may be the only way to directly measure mass distribution within a spray.

Optically dense sprays are defined as sprays or regions of sprays and spray formation that are difficult to measure with traditional diagnostics. Advanced diagnostics are broadening our understanding of sprays by unveiling the dense regions of sprays. Traditional shadowgraphy and other attenuation methods breakdown at optical densities between 1 and 2 (based on log₁₀ scale). An advanced technique was developed to differentiate the photons that are scattered multiple times and those that propagate nearly straight through the spray—Ballistic imaging, developed by Linne et al. (2005) uses an ultrafast time gate to reject photons that are scattered and therefore take a longer time to get through the spray. A second

method of spatially differentiating multiply scattered photons is to employ a known structured pattern to the illumination source. Berrocal et al. (2008) developed structured light illumination to account for and remove the effects in planar Mie scatter and planar laser induced fluorescence techniques. To isolate the continuous liquid structures emanating from the injector, (Charalampous et al., 2009) developed optical connectivity or light tube imaging to illumine just the intact liquid structure and allow discrimination of the dense droplet cloud surrounding the core structure.

To avoid the effects of scattering and refraction, a higher energy penetrating radiation can be used. X-ray diagnostics can be divided into two categories: synchrotron x-rays, requiring a large installation and tube source x-rays readily available for laboratory-based experiments.

Synchrotron light sources produce a brilliant, directed source of Bremsstrahlung radiation over a range of x-ray energies. The x-ray beam can be energy tuned via a monochromator, collimated with slits, and focused with grazing mirrors. The ability to tune the source allows for the application of several techniques including radiography, phase contrast, small-angle x-ray scattering, and fluorescence.

Synchrotron radiography has been employed by many researchers to study a large variety of sprays (Kastengren and Powell, 2007; Poola et al., 2000). The high photon flux and focused beam allow for time-resolved spray measurements of low absorbing materials. Transient automotive sprays were studied by Cai et al. (2003) and Powell et al. (2000). Swirl coaxial injectors have been studied using time-averaged radiography (Schumaker et al., 2012) and time-resolved measurements have been used to investigate droplet dynamics (Lightfoot et al., 2012).

X-ray phase contrast imaging was used by Lin et al. (2011) to study jet sprays. The higher x-ray energies in phase contrast imaging expose phase discontinuities to image ligaments and droplets. Small-angle and ultra-small-angle x-ray scattering have been used for measurements in sprays with very small and dense droplet fields (Lin et al., 2008). The relatively narrow line widths of the x-ray beam allow for an energy resolved detector to differentiate between elastically scattered photons and fluorescent photons emitted from inner shell electrons. Thus x-ray fluorescence can easily differentiate two fluids allowing for measurements of mixing; turbulent mixing in an argon jet was shown by Kastengren et al. (2011).

Tube source measurements use a polychromatic cone beam from a metallic anode and are available for laboratory scale measurements. The tube sources are not collimated or energy tuned, so the experiments must be carefully designed to account for these drawbacks. The tube sources are used in measurements across the multiphase flow measurement field, reviewed by Heindel (2011). Continuous-wave sources have been used for time-averaged radiography of sprays; by rotating the source and detector or the spray, three-dimensional spray images can be generated using computed tomography. Industrial sources and medical sources with rotating anodes for increased flux have been used by Meyer et al. (2008) and Coletti et al. (2014), respectively. X-ray measurements were coupled with PDPA and Mie scatter results by Balweski et al. (2012), who measured the mass distribution in the dense and dilute regions of the spray. By employing high-speed detectors, radiography measurements have been made at 2 kHz with an intensified detector. Char et al. (1989) made measurements of slot injectors with long path lengths and compared these with visible light images.

Multiple tube sources were used to image a spray onto high-speed linear detectors and measure time-resolved planar slices of the spray at 1 kHz (Lim et al., 2013).

A second type of tube source emits a pulse of energy, and a flash of x-rays approximately 70 ns in duration is produced. These sources have been used to achieve time-resolved images of sprays. Birk et al. (2003) imaged evaporating sprays and compared their results with shadowgraphy; the flash images revealed the inner core structure that was otherwise hidden by multiply scattered photons from the exterior of the spray. Flash x-rays of high pressure dodecane sprays were made by Robert et al. (2010). X-ray diagnostics present new capabilities that can be applied to sprays that require further study, such as the impinging jet injector.

Impinging-jet sprays have been studied quite extensively, however to the best of the author's knowledge, x-ray diagnostics have not been previously explored. In the mid-20th century, breakup regimes and impact waves were examined. Heidmann and Humphrey (1951) measured fluctuations in the impact waves; Heidmann (1957) measured breakup frequencies and started to categorize the regimes. The sheet instabilities were determined to be from instabilities in the jets exiting the nozzle as well as aerodynamic influences that led to the intermittent breakup of ligaments and droplets. The frequency of the waves in the sheet increased with an increase in jet velocity or a decrease in impingement angle. Four spray patterns were observed. The closed rim pattern exhibits a small liquid sheet with thick liquid rim; the rim eventually impinges and forms drops downstream. The periodic drop pattern has a rim where droplets develop and are thrown off tangentially. In the open rim pattern, the rim breaks into droplets as seen in single liquid jets. The highest velocity regime is the fully developed pattern with waves emanating from the point of impingement; the waves then

break into ligaments and droplets. Changes in the spray relating to the jet behavior were studied by Dombrowski and Hooper (1964), who investigated the differences between laminar and turbulent jets. They showed the relationship between sheet velocity and jet velocity to be close to that of the axial velocity component for turbulent jets, and they described a relationship between the drop size and the product of the velocity and sine of the impingement half angle.

Quantities of particular interest in this work are mass distribution and liquid sheet or film thickness. Analytical film thickness models were developed by Miller (1961) and Hasson and Peck (1964). Interferometry was applied to measure the film thickness by Fukui and Sato (1972) and Choo and Kang (2001). The experiments and models agree qualitatively in the comparisons and quantitatively in some cases. The liquid sheet is observed to become thinner as impingement angle is increased, while the change is negligible with jet diameter for similar conditions. Laser-sheet measurements perpendicular to the axial direction have been used to determine the mass distribution of the droplet field, with attenuation and fluorescence being utilized by Mallory and Sojka (2012) and Jung et al. (2003), respectively. In these works, the mass distribution measurements showed a concentrated area in the center of the spray.

To enhance the knowledge of how the mass is distributed within the spray requires knowledge of how the two liquids are mixing once they come in contact. Mechanical patternators were used to make downstream measurements and quantify various mixing regimes, such as reflective mixing, transmissive mixing, and an intermediate regime termed well-mixed. Initial measurements were made by Rupe (1953), who determined that a 45 degree included angle between the approaching jets was effective for mixing. Rupe (1956)

also determined flow parameters needed to achieve uniform mixture ratios; for example, matching momentum and jet diameter produced better mixing, as shown in Equation 1.

$$\frac{\delta_1 V_1^2 D_1}{\delta_2 V_2^2 D_2} = 1 \quad (1)$$

The mixing was most uniform when the ration in Equation 1 was equal to one. Here, δ is the liquid density, V is the jet velocity, and D is the jet diameter. Similar studies were performed by Elverum and Morey (1959) also using patternators to investigate the optimum mixture ratio in unlike injectors. Another mixing technique was explored by Somogyi and Feiler (1959) using dyed fluids and the transmission of various colors of light to determine mixture ratio in each droplet. They showed doublet impinging jets outperformed triplet impinging jets in mixing. Hoehn studied orifice shape alignment and cavitation and their effects on mixing (1972) and discovered non-circular orifices may be better for mixing but are more sensitive to alignment. They also found that cavitation was not an enhancement to mixing in cold flow studies. Similar studies by Nurick (1976) also showed that cavitation reduces mixing performance and that non-circular orifices are not as affected by cavitation. Ashgriz et al. (2001) reviewed the previous measurements of mixing and added measurements of miscible and immiscible fluids. They described mixing regimes and potential mechanisms for mixing, including momentum and the steadiness of the jet prior to impact; they diagramed the process in Figure 1-2. The mixing regimes were reflective, where the momentum was too low for the jets to penetrate each other, transmissive, where the jets had sufficient momentum to pass through each other, and postulated the well mixed regime, where the liquids combined and mixed perfectly.

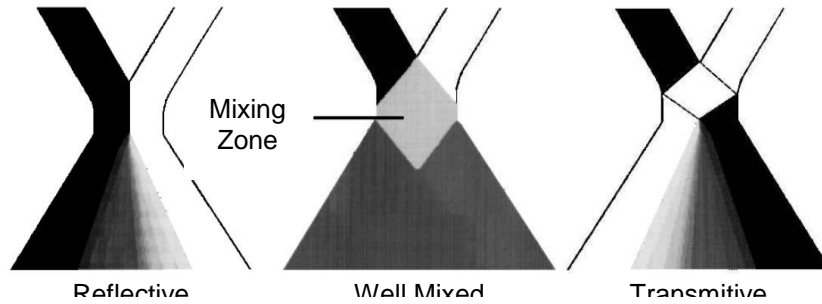


Figure 1-2. Mixing regimes as described by Rupe, 1953 and Ashgriz et al. (2001). (image from Ashgriz et al., 2001).

Laser induced fluorescence was employed to make mixing measurements by McDonnell et al. (1999). The scaling between the cold and hot fire tests was determined to be the Reynolds number. Yuan and Huang again used laser induced fluorescence to make mixing measurements and related them to liquid jet stability. Fluctuations in the mixing change as the free jet length changes due to changes in the free jet instability, Figure 1-3.

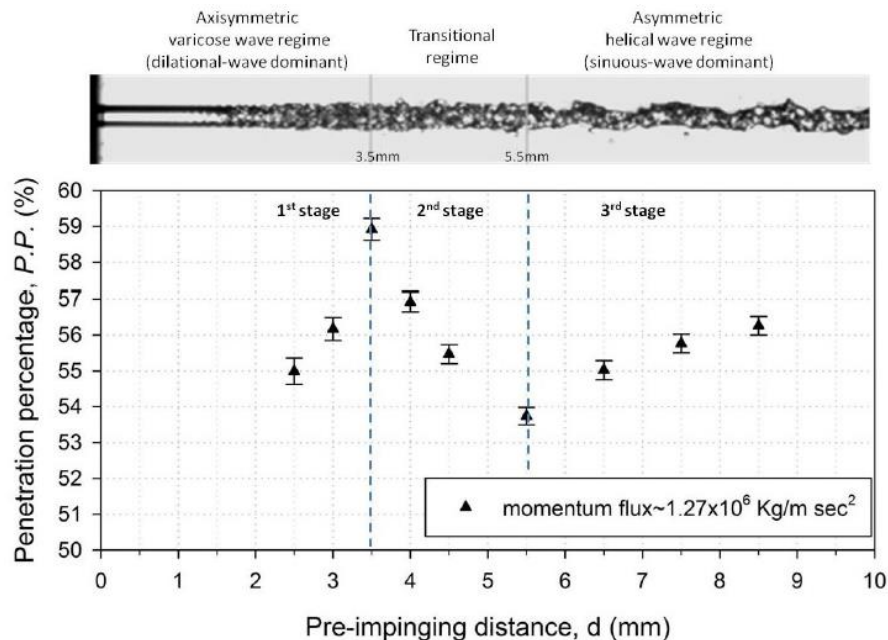


Figure 1-3. Changes in mixing seen as a function of free jet length or pre-impingement distance (Yuan and Huang, 2012).

Of particular interest to the author is the use of gelled simulants, to investigate mass distribution and mixing. Particulate gels made with aluminum were investigated by Kampen et al. (2007). The gel sheets would atomize with up to 40% Al, and three breakup regimes were described being ray shaped, ligand, and fully developed. Cellulosic gel sprays were studied by Mallory and Sojka (2012), where no droplet break up was observed. The elasticity of polymer gels was studied by Coil (2009), defining a steadiness and disturbances. The addition of nano-particles to gel was studied by Baek et al. (2011), finding similar breakup regimes as Kampen et al. (2007). A comparison between polymer and particulate gels was made by Negri et al. (2013), characterizing the different breakup regimes. Shown in Figure 1-4 the breakup of the particulate gel (a) is drastically different from the stringy wavy sheet of the polymer gel (b) which fails to fully break up.

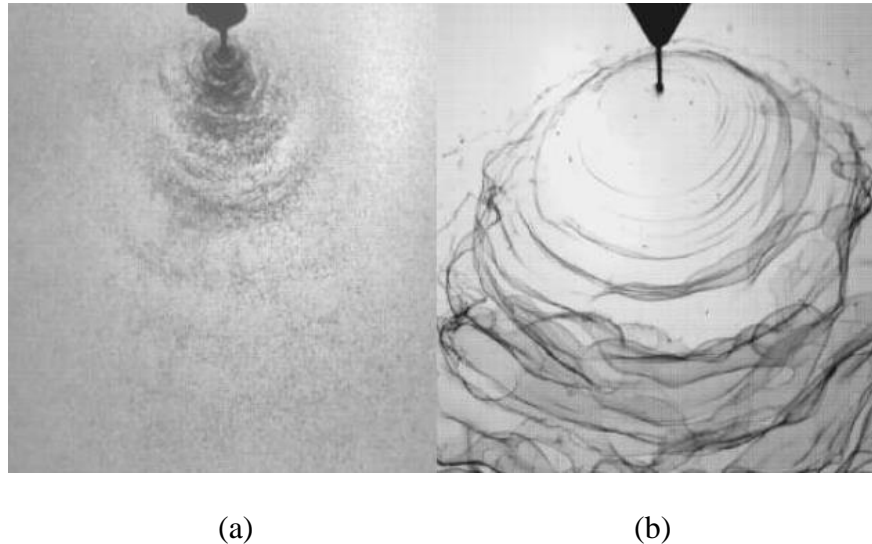


Figure 1-4. Two shadowgraphs of gelled impinging jets are shown, (a) shows the breakup of a particulate gel, and (b) shows the sheet formation of the polymer gel (Negri et al. 2013).

Newtonian and no-Newtonian mixing models were published by Chen and Yang (2011) and Chen et al. (2012), neither model shows transmissive mixing. Lower fidelity

models, that describe overall mass distribution, are currently be developed and validated by the author, Baldwin et al. (2014).

Impinging jet atomization is commonly used in propulsion devices that rely on hypergolic ignition and combustion. Knowledge of the fuel and oxidizer distribution and mixing is critical to understand propulsion performance and safety. When hypergolic propellants are injected they start to generate gases, and when they meet and begin to react more gases are formed. This gas generation can inhibit the two jets from meeting and mixing and has been shown in several experiments by Lawver, (1968); Houseman, (1968); and Campbell et al. (1971). These studies show two distant regimes. In the first regime the jets meet and the reaction occurs predominantly between the two jets and little mixing occurs. If the jet velocity is increased or propellant temperature is decreased more mixing can occur and the combustion zone is highly mixed and more uniform. These velocity trends agree with the non-reacting physics previously discussed. Nurick and Clapp (1969) showed that the cold flow results agreed very well with hot fire tests if appropriate simulants are used. The gas generation has been shown to enhance the mixing of propellants so long as it is not a dominating factor seen by Houseman in 1970, where the optimal performance is similar but not exactly Rupe's conclusions on mixing performance. Exiplex fluorescence was applied in 1997 by Feikema and Smith, where they concluded the combustion process was mixing limited due to the short chemical time scales. More recent hypergolic ignition have included gelled hypergolic propellants, the findings suggest that matching the rheology between the gels can yield similar ignition delays to take up in gelled hypergolic propellants (Dennis et al., 2011). The ignition of non-volatile gelled fuels has been investigated by Coil (2010) measuring ignition delay in drop tests, splash plate tests, and impingement tests.

As shown the impinging jet spray has been studied quite extensively, but remains an excellent candidate for the application of x-ray measurements to quantify mass distribution and mixing in the near field region. It has also been shown that based on previous studies, the non-reacting measurements can provide powerful insights to what may occur in an operating engine.

Proposed Research

X-ray spray diagnostics were proposed to make mass distribution and mixing measurements within impinging jet sprays. X-ray based diagnostics are less susceptible to scattering and refraction within a turbid media and have been previously show to be an excellent diagnostic tool for spray research. The like-doublet impinging jets spray displays characteristics of large liquid structures and dense droplet fields. The proposed experiments utilize polychromatic x-ray tube sources for 2D and 3D imaging, and a narrow band synchrotron source for path averaged point measurements.

Tube source diagnostics are shown to be capable of time-averaged, time-resolved, and high-speed quantitative measurements of liquid mass distribution within an impinging jet spray. Under certain conditions it is desirable to enhance the contrast of the images by doping the water with potassium iodide (KI). The effects of KI are studied and discussed. The use of polychromatic sources and sprays with a high variation of liquid path length renders the use of a single coefficient inaccurate. The lower energy x-rays are preferentially attenuated resulting in a high energy or “harder” beam exiting the spray. This phenomenon known as spectral beam hardening is modelled and accounted for through the use of a variable attenuation coefficient dependent on the level of transmission. These measurements are

validated against the Advanced Photon Source, a bending magnet synchrotron source at Argonne National Laboratory.

Measurements within sprays using a broadband flash x-ray tube source are compared with narrowband x-rays from the APS. Time-resolved liquid mass distributions measured from two-dimensional radiographs using the flash source are compared with time-resolved raster-scanned point measurements from the APS for different locations within the breakup and atomization regions. Static measurements to investigate the potential effects of spectral beam hardening for different contrast agent concentrations in water provide information on the feasibility, accuracy, challenges, and potential strategies for utilizing broadband x-ray tube in quantitative time-resolved spray measurements. Following Taylor's Hypothesis, a spectral analysis was performed (Taylor, 1938). The spatial frequency is captured from the single-shot time-resolved radiographs, and using the sprays velocity it is compared to the temporal frequencies of a single local time-trace.

The ability to achieve high-speed radiography at up to 20 kHz using a continuous x-ray tube source for relatively low path lengths is pertinent to measure realistic flows. Simultaneously, high-speed optical imaging at 20 kHz is also used to capture qualitative features of the spray structure at high resolution and image contrast for comparison. A continuous x-ray tube source projects a radiograph onto a scintillator and intensified CMOS camera, and a continuous visible source coupled with a second CMOS camera captures radiographs and backlit images, respectively, at 20 kHz. Challenges including the broadband spectrum, pseudo point source, and low flux relative to synchrotron sources require close attention to the imaging system used. To increase the attenuation of the spray, potassium

iodide (KI) dissolved in solution is used as a contrast enhancing agent. The imaging system is designed to optimize both the x-ray imaging and visible light images.

X-ray fluorescence using the APS source is advanced to measure the mixing of two impinging fluids. These measurements are made in the near-field impingement zone where mechanical and laser based measurements are not feasible. The major obstacles of acquiring quantitative mixing data are relating the signal to a liquid mass and overcoming the challenges of the fluorescence signal being reabsorbed by the spray en route to the detector.

X-ray radiography and fluorescence are used to address these challenges and to enable measurements in the impingement region itself, thereby providing direct observation of the processes leading to the mixing of unstable liquid jets. Because the primary interaction of low-energy (≤ 10 keV) x-rays with sprays is through absorption and weak scattering, the attenuation signal can be related to the path-length-integrated liquid density along the path of the x-ray beam with minimal uncertainty. X-ray radiography has been demonstrated with high spatial resolution and signal-to-noise ratio in studies of liquid injection into ambient gas environments using line-of-sight x-ray attenuation.

The feasibility of utilizing x-ray fluorescence as a means to study the mixing behavior of impinging liquid jets, particularly in the complex near-field region, to overcome the challenges associated with mechanical patternators and optical techniques is investigated. The simultaneous measurement of x-ray attenuation and fluorescence allows for the differentiation of the two liquids and the determination of line-of-sight mass distribution before, during, and after jet impact. Like radiography, x-ray fluorescence benefits from insensitivity to phase interferences, but has the added advantage of allowing each fluid to be uniquely identified using an element (added as a tracer) that fluoresces at a particular, known

x-ray energy. By seeding the two liquid streams with different tracer elements, the liquids that originate from each jet can be tracked simultaneously with high dynamic range. In this way, two liquids with similar x-ray attenuation cross-sections can be excited with the same x-ray source and differentiated by their characteristic fluorescent emission. The experimental errors incurred using this technique are investigated and the removal of such errors are addressed using two possible methods.

After quantifying the system and accounting for reabsorption, measurements are conducted to study the effects of several parameters of the like-doublet impinging jet injector. Those parameters include: the rheology of the fluid, investigating the effects of non-Newtonian shear thinning gels; and the geometry of the injector coupled with various flow velocities to investigate the effects of impingement angle, momentum, and free jet instabilities. The experimental facilities are defined, the results are discussed, the associated errors and uncertainties are analyzed, conclusions are drawn, and future measurements within this area are discussed.

CHAPTER II

EXPERIMENTAL FACILITIES

Mass Distribution

The mass distribution measurements were made relating the ratio of attenuated x-rays to a liquid path length using the Beer-Lambert Law. The distribution of mass is quantified as an equivalent path length. The mass at each location would be determined through the path length multiplied by the integration area multiplied by the density. The total mass at each horizontal location can vary based on the vertical velocity of the spray. A slower moving spray will have more mass at the given horizontal location.

These liquid path lengths represent the mass distribution and were determined using radiography and computed tomography. Measurements were made with a narrow band synchrotron and broad band tube source. A challenge with tube sources is the attenuation coefficients of materials changes with photon energy. The spectra of the absorbing species are shown in Figure 2-1. Methods by which this broad spectra is dealt with is discussed.

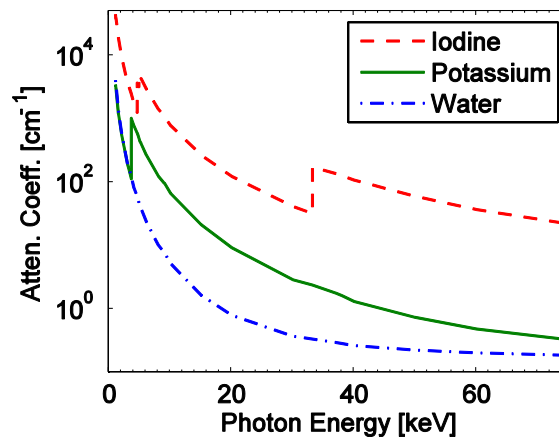


Figure 2-1. Attenuation coefficient vs. photon energy of the absorbing species, (Hubbell and Seltzer, 1995).

Advanced Photon Source Radiography

The x-ray source for the APS 7-BM beamline employed in this work is a synchrotron bending magnet, which provides a nearly collimated, polychromatic x-ray beam. This beamline consists of two enclosures. The first enclosure (7BM-A) contains slits to condition the beam size and a double multilayer monochromator ($\Delta E/E = 1.4\%$) to create a monochromatic beam. The energy range of the monochromator is 5.1–12 keV. The second enclosure (7BM-B) houses a pair of Kirkpatrick-Baez focusing mirrors (Eng et al., 1998), the experimental spray equipment, and the x-ray detector. Further details regarding the beamline setup are given by Kastengren et al. (2012). Figure 2-2 diagrams the hutches and the x-ray beam path.

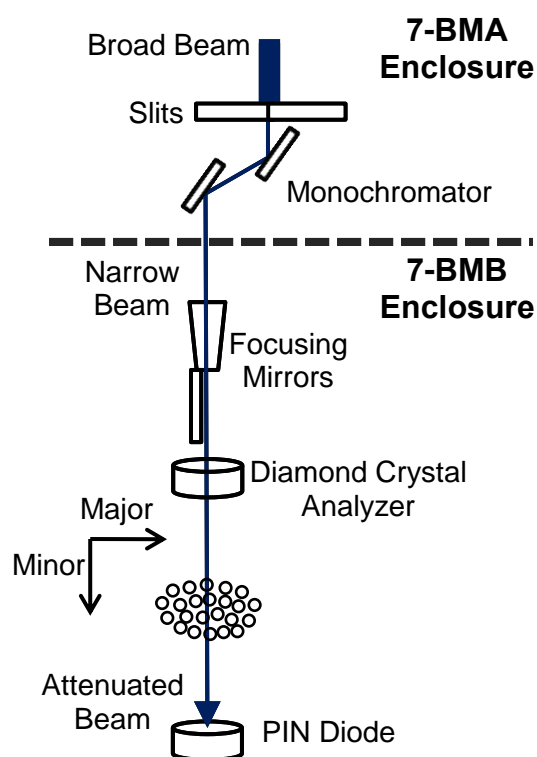


Figure 2-2. Diagram of beamline 7BM, Advanced Photon Source, Argonne National Laboratory.

The current APS experiments use a focused x-ray beam with full width at half maximum (FWHM) dimensions of 5 μm (vertical) \times 6 μm (horizontal) at 10 keV photon energy; with 1.6×10^{10} photons per second flux at the detector. The detector is an unbiased, 300- μm thick silicon PIN diode with 89% of the x-ray photons being absorbed.

Time-Averaged Measurements

The PIN diode output was amplified with a transimpedance amplifier and normalized by a beam intensity monitor. The signal is time-averaged over a 1 second integration time. Data points collected from the raster-scanned spray were mapped to a two-dimensional grid that was slightly larger than the spray to allow for background normalization. The point measurements were dark-current subtracted and flat-field normalized. The signal was converted to an equivalent path length (EPL) of liquid along the line of sight and compiled into two-dimensional, interpolated images via MATLAB. Because of the relatively small focal spot size, the spatial resolution of the interpolated images was limited by the raster scan spacing, which was a minimum of 50 μm near the jet centerline.

Time-Resolved Measurements

The PIN diode output was amplified with a transimpedance amplifier and recorded on an oscilloscope and normalized by diamond crystal analyzer positioned up stream of the spray to correct for modulations in beam intensity. Data were collected as path averaged local time-traces at 2.5 MHz for a period of 5 seconds. The dark current was subtracted from all data points and points far from the spray were used as background for flat-field normalization. The signal was converted to an equivalent path length (EPL) of liquid along the line of sight.

Continuous Wave Tube Source Radiography

The Iowa State University (ISU) X-ray Flow Visualization Laboratory is capable of 16-bit radiography, stereography, and computed tomography (CT), as described in previous publications (Heindel et al., 2007, 2008). Twin LORAD LPX200 portable sealed tube sources produce cone beams and are positioned ninety degrees apart on a movable rotation ring, as shown in Figure 2-3. The supply voltage and current can be varied from 10 to 200 kV and 0.1 to 10.0 mA, respectively, with 900 W maximum electrical output per source from a copper anode. Opposite of one source is a cesium-iodide phosphor screen coupled to an Apogee Alta U9 camera via a 50 mm, f/1.2 lens. The CCD camera is monochromatic, 16-bit, with 3072×2048 pixels. Unlike the APS beam, in which the focal spot is placed in the spray, the focal spot of the tube source x-rays is at the 1.5 mm source anode.

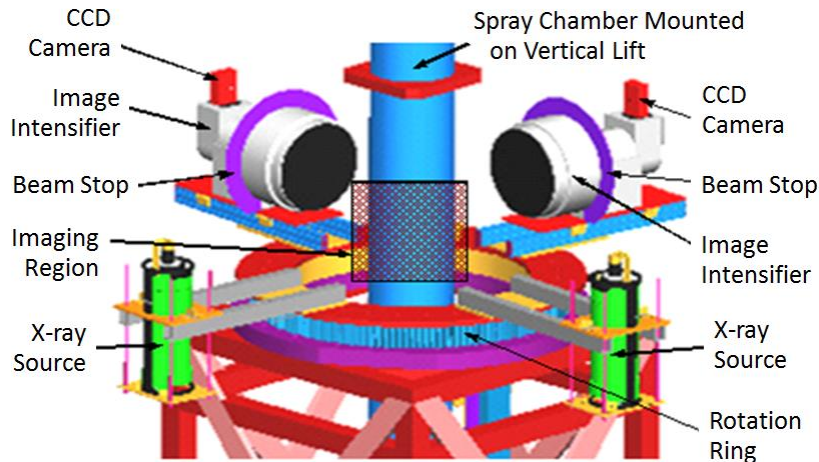


Figure 2-3. Set-up for x-ray radiography and 3-D computed tomography using broadband tube sources and planar imaging systems (Heindel et al., 2007).

The x-rays spread from the pseudo point source and the resolution is determined by the geometric magnification, geometric unsharpness due to the penumbra effect, blurring in

the phosphor screen and CCD chip. The spatial resolution in the current work is restricted by the penumbra effect and CCD pixel size of $120\ \mu\text{m}$. For the current work, the detector is placed near the spray to maximize spatial resolution as the blurriness due to the penumbra effect increases with distance from the spray at a faster rate than magnification. The resulting spatial resolution of the radiographs is $\sim 800\ \mu\text{m}$, estimated from the 10-90% signal rise at the edge of a glass slide. An above view of the radiography system is shown in Figure 2-4. The copper filter is curved to evenly attenuate the beam. The x-rays are incident upon the scintillator where they are absorbed and the energy is emitted in the visible spectrum that is imaged by the CCD camera.

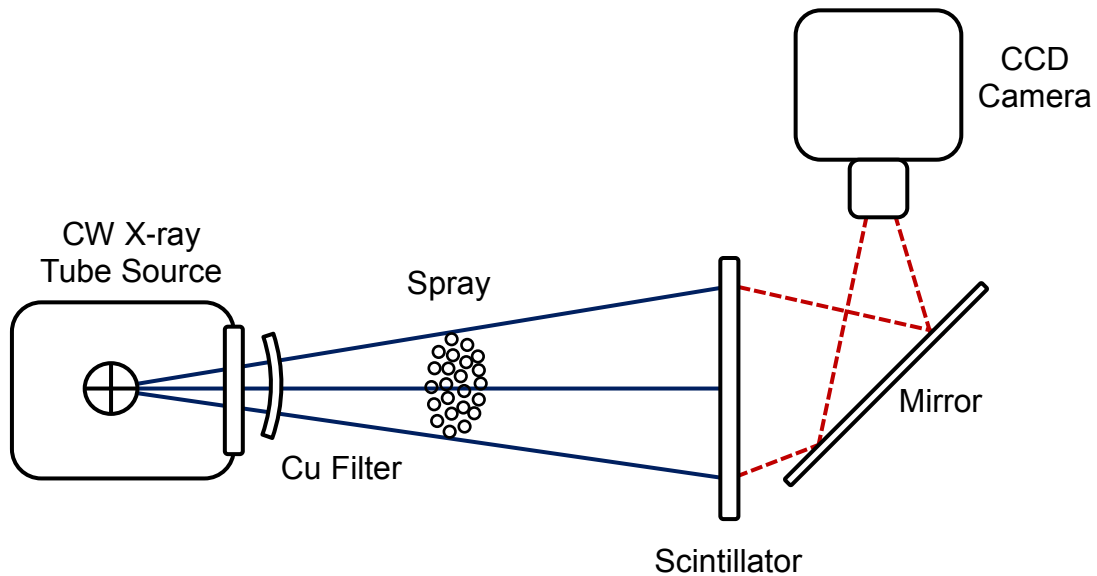


Figure 2-4. Side view of CW tube source for time averaged imaging. Blue solid lines encompass the x-ray cone; red dashed lines encompass the visible light.

The current experiments were conducted with the tube source set to 80 keV and 10 mA. A $127\text{-}\mu\text{m}$ thick copper filter was used to pre-harden the beam. The exposure time was 6.5 seconds. The power settings and filters were selected to maximize the signal-to-noise

ratio (SNR) of the imaging system, and the exposure time was set to nearly saturate the pixels. The SNR was calculated by dividing the peak signal from the standard deviation of the pixels in the image. The radiograph images from the tube source were dark-current subtracted and flat-field normalized, with water spray and flat-field images averaged by 1000 frames and 15% KI spray and flat-field images averaged by 100 frames. The CT scan is used to reconstruct data from 360 time-averaged radiographs collected at 1° increments into a three-dimensional image with 700 μm voxels (three-dimensional pixels). The spatial resolution of 1400 μm for the CT scan, determined from the 10-90% signal rise at the edge of a glass slide, is degraded from the source radiographs as some of the higher spatial frequencies are lost during the reconstruction process. A summary of experimental parameters used for the narrowband, low-energy and broadband, high-energy x-ray sources at the APS and ISU, respectively, are shown in Table 2-1.

Table 2-1 Measurement parameters for narrowband and broadband x-ray sources.

Source	APS Synchrotron	ISU Tube Source		
		2-D Radiograph of Water	2-D Radiograph of 15% KI	3-D CT Scan of 15% KI
Imaging Method	Raster Scan of Water	2-D Radiograph of Water	2-D Radiograph of 15% KI	3-D CT Scan of 15% KI
Beam Shape	Collimated	Cone	Cone	Cone
Spectrum	Monochromatic	Polychromatic	Polychromatic	Polychromatic
Energy [keV]	10	< 80	< 80	< 80
Detector	PIN Diode	16 Bit CCD	16 Bit CCD	16 Bit CCD
Binning	None	1 x 1	1 x 1	4 x 4
Exposure [s]	1	6.5	6.5	6.5
Pixel Array [μm^2]	5 x 6	120 x 120	120 x 120	380 x 380
Frame Averaging	None	1000	100	360
Time per Scan [s]	~ 1000	13000	1300	600

The APS provides narrowband x-rays, such that the attenuation coefficient is readily calculated from the ratio of measured x-ray intensities, I_0 and I , before and after a liquid

structure of known path length, l , and constant number density. Adhering to Beer's Law for a polychromatic source, where ψ is the convolution of the energy dispersion and the camera response function, Equation 2-1 can be simplified to Equation 2-2 if the attenuation coefficient, α , defined in Equation 2-3, is a function of attenuation cross section, σ , and number density, N , and not of the photon energy, $h\nu$.

$$\frac{I(y, z)}{I_0(y, z)} = \frac{\int e^{-\int \alpha(h\nu, x, y, z) dx} \psi(h\nu) dh\nu}{\int \psi(h\nu) dh\nu} \quad (2-1)$$

$$\frac{I(y, z)}{I_0(y, z)} = e^{-\int \alpha(x, y, z) dx} = e^{-\alpha l} \quad (2-2)$$

$$\alpha = \sigma N \quad (2-3)$$

The attenuation coefficient of the broadband source is calculated in a similar manner, with signals, I and I_0 obtained from images collected with and without the spray, respectively. Although theoretically it is anticipated that the attenuation coefficient will depend on wavelength to some degree, if this effect is minimal, then Equation 2-2 is applicable and the data using the broadband tube source should agree with that of the APS. To illustrate the potential differences in the attenuation behavior of the APS and ISU tube sources, their approximate spectra are shown for comparison in Figure 2-5. The APS spectrum shows a nearly Gaussian line shape with a FWHM of ~0.14 keV centered at ~10 keV. The spectrum of the ISU tube source is first approximated using Kramers' Law for the broadband bremsstrahlung radiation emitted by an electron hitting a solid target (Kramers, 1923). The spectrum is altered due to the attenuation of the physical system (ISU w/o Filter) and further reduced by a copper filter (ISU w/ Filter) to preharden the x-ray energy. The two

latter spectra are simulated using attenuation coefficients in the NIST tables (Hubbell and Seltzer, 1995).

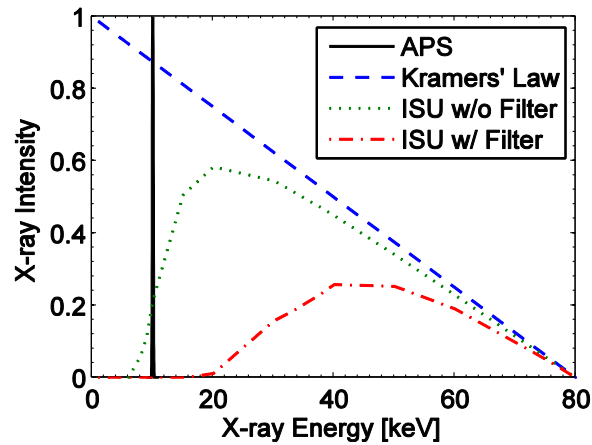


Figure 2-5. Theoretical spectra for the APS and broadband tube source x-rays on a relative intensity scale.

Note that prehardening of the x-ray radiation significantly reduces the intensity of the low-energy x-rays from the tube source. This, along with the low path lengths of typical engineering sprays, helps to minimize the effects of preferential absorption and improve the likelihood that Equation 2-2 can be utilized directly. On the other hand, low levels of attenuation for the higher energy x-rays from the filtered tube source also reduce image contrast and increase susceptibility to background interferences. To evaluate these effects, the accuracy and precision of 2-D and 3-D measurements of liquid mass distributions obtained from the broadband tube source are compared with a raster scan of the same spray using the APS source (see Table 2-1).

Flash Tube Source Radiography

Tube source x-ray emission consists of a broadband Bremsstrahlung spectrum punctuated by narrow peaks due to x-ray fluorescence of the anode material. The upper energy limit is determined by the tube voltage and the lower limit by the source window attenuation. Typical x-ray energies for spray imaging can range from 5 keV up to 120 keV. Previous tube-source time-averaged studies used a metallic filter to spectrally pre-harden the beam by attenuating low energy x-rays. This pre-hardened beam is narrower and the change in attenuation coefficient with photon energy is reduced, allowing for the use of a constant attenuation coefficient for the path lengths that are typical in engineering sprays. Prehardening the beam greatly reduces the usable flux—a serious disadvantage for instantaneous measurements.

Obtaining temporal resolution in a two-dimensional radiograph using a flash x-ray source requires maximizing the usable flux that is both readily attenuated by the spray and produces sufficient contrast on the detector. This poses challenges to the emission and collection of usable radiation. Flash x-ray pulses are produced when a bank of capacitors discharge in rapid succession and the full current pulse impinges upon the anode within tens of nanoseconds. The cone beam emission of x-rays passes through a thin beryllium window, through the spray, and then is partially absorbed by an image plate. The image plate is then read by a laser scanner and a digital image is formed. The cone beam emission from the source anode causes image magnification and its finite size also leads to geometric blur due to the penumbra effect, as illustrated in Figure 2-6. The unfiltered x-ray spectrum hardens as it is attenuated through the spray, resulting in a varying attenuation coefficient. In this work, a modeling and calibration approach is used to determine the effective attenuation coefficient

for quantitative measurements, maximize signal-to-noise ratio, and optimize spatial resolution. Relevant imaging parameters include the source voltage, source anode size and material, source window material, anode-spray distance, spray-plate distance, image plate (detector) and laser scanner.

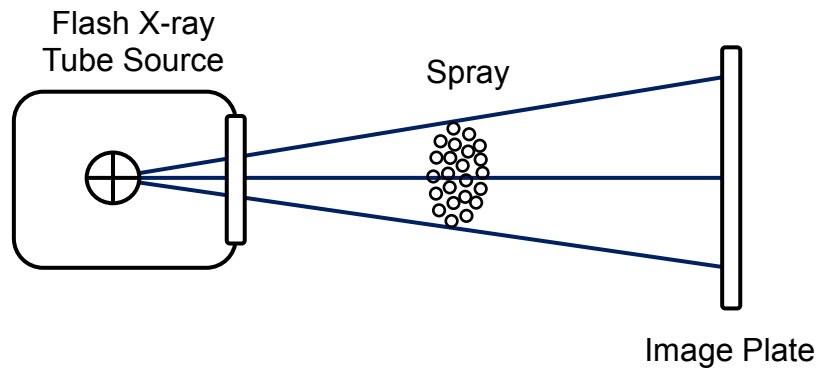


Figure 2-6. Flash x-ray source shown with spray and image plate. Blue solid lines encompass the x-ray cone.

X-ray energy is fixed by selecting the number of capacitors used. Starting with a 150 keV commercial system (L-3 Communications), half of the capacitors were removed to produce a 75 keV system resulting in a larger fraction of lower energy photons for increased attenuation. The tubes in a flash source are readily interchangeable, and a 1 mm tungsten anode was chosen to balance anode longevity with the need to have a small focal spot size for reducing the effect of penumbra and improving spatial resolution. Anodes of lower atomic number materials than tungsten can produce increased levels of lower energy photons, but these degrade more with each pulse. This leads to less consistent imaging behavior and increases the frequency and expense of anode replacement, especially for smaller anodes. A beryllium window was chosen over other materials, such as steel, to

maximize the output of lower energy photons and maximize attenuation (i.e., image contrast) through the spray.

The locations of the anode, spray, and detector affect the total measured flux, the influence of penumbra, and the geometric magnification. The source is placed as near the image plate as possible (225 mm) to maximize the photon flux on the detector. Both the penumbra and magnification increase if the spray is moved closer to the anode. These are offsetting effects with regard to image resolution, but the penumbra will increase at a greater rate than the magnification. When using a relatively large, millimeter-sized source, the penumbra may dominate any benefit of magnification; therefore the spray was placed 200 mm away from the anode and within 25 mm of the image plate.

A Kodak GP image plate was chosen for higher image contrast. The thickness of the plate determines the total absorbance and resolution. A thinner plate tends to increase the resolution with a reduction in the total absorption. A laser scanner with 50 μm focal spot size (ScanX HC) was used to read the imaging plates in post-processing. The focal spot size of the scanner affects the resolution and contrast of the image, with a smaller focal spot yielding higher resolution and lower contrast. During post-processing, it was found that the background collected with the spray off was inconsistent, and flat-field normalization was required on a shot-to-shot basis. Hence, the shape of the background was determined in a number of steps and approximated by a third-order polynomial. Each horizontal array was linearly normalized and pixels with significantly greater attenuation than the standard deviation were eliminated from the array as they were believed to be within the spray. The background signal is then fit with a polynomial and used to normalize the original data array.

The polynomial fit normalization reduces the transmission error of 12% of max signal by half or more.

Once the imaging system was in place, calibration images were collected using steady liquid jets of known diameters, and the system was modeled to determine the attenuation coefficient empirically and analytically. The calibration experiments were modeled in MATLAB using the known or approximated behavior of system elements. The output spectrum was a linear approximation of a known 150 keV spectrum. The photon energy dependent attenuation coefficients were taken from NIST tables (Hubbell & Seltzer, 2004). The imaging plate properties were provided by Kodak, and the laser scanner was assumed to be independent of photon energy (KODAK, 2006). The attenuation coefficient was modeled using known or estimated values for the source, spray, and detector. The 75 keV spectrum was approximated from a 150 keV spectrum obtained empirically by the tube manufacturer with a linear correction factor, as shown in Figure 2-7. Several models exist to predict the spectral output of tube sources, and it was found that a linear correction can be applied to estimate a lower voltage source given the output of a higher voltage source. The 150 keV spectrum is multiplied by the linear correction factor to rescale the intensities while maintaining the approximate shape. The spectrum is used to estimate the general behavior of the attenuation coefficient. Equation 2-4 shows the linear rescaling for the 75 keV spectrum based on the original 150 keV spectrum.

$$\left[Spectra_{75}(h\nu) \right] = \left[Spectra_{150}(h\nu) \right] \times \left[-\left(\frac{1}{75} \right) h\nu + 1 \right] \quad (2-4)$$

The linear correction factor is successfully tested by comparing tungsten tube source spectra calculated with X-ray Oriented Programs (XOP) version 2.11. The linear correction is

incapable of estimating the changes in characteristic peaks, but the difference in overall intensity does not appreciably change the attenuation coefficient, shown in Figure 2-7.

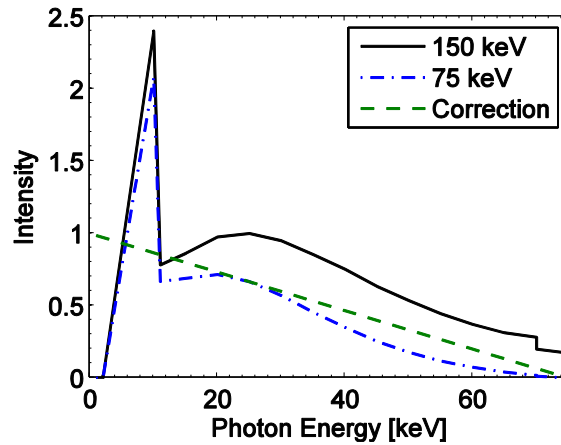


Figure 2-7. Experimental 150 keV spectrum and estimated 75 keV spectrum with linear correction.

Using the modeled 75 keV spectrum, three spectra are computed as shown in Figure 2-8 to estimate the effects of beam hardening. These include an incident spectrum after passing through the beryllium window and air, a spectrum after the x-rays pass through 2 mm of water, and a spectrum after the x-rays pass through 2 mm of water with 15% by mass of potassium iodide (KI), a contrast enhancing agent. NIST attenuation values are used to model the attenuation by the tube source window, the air, and the water or KI solution (Hubbell & Seltzer, 2004). Data from Kodak are used to model the imaging plate absorption and photoemission (KODAK, 2006). It was assumed that the reading by the laser scanner was independent of the x-ray spectrum. Figure 2-8 shows that the incident spectrum is highly attenuated by the window and air. It also shows the preferential attenuation of lower energy x-rays, demonstrated by the large decrease of intensity at lower energies relative to higher energies. This is most noticeable in the case of pure water, where the x-ray intensities at

lower energies are greatly attenuated, although the intensities at higher energies show very little attenuation. For the case of 15% KI, there is greater attenuation for low energy x-rays, but there is also noticeable attenuation at higher x-rays. These effects can be understood by analyzing the energy dependent attenuation water compared with iodine and potassium, as shown in a plot of photon energy vs. attenuation. The increased attenuation coefficient at lower x-ray energies leads to spectral beam hardening for both the case of water and water with a contrast enhancing agent.

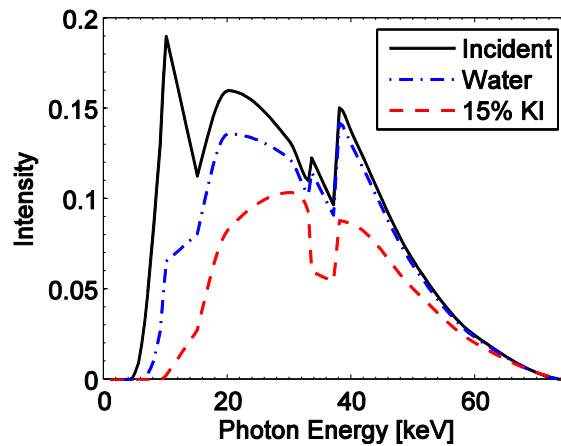


Figure 2-8. Modeled spectra, showing energy shift after passing through water and 15% KI.

The APS 7BM beamline was used to verify the accuracy of the flash images and compare the temporal and spatial frequencies of the time traces and radiographs, respectively. Table 2-2 compares each of the sources and techniques. The APS has very high spatial resolution with a monochromatic beam. These features greatly reduce the potential measurement error at the APS. The flash technique can produce time-resolved, two-dimensional images, but with significant trade-offs in image resolution and signal-to-noise ratio.

Table 2-2. Measurement parameters for the x-ray techniques.

Source	APS Synchrotron	Flash Tube Source
Imaging Method	Raster Scan of Water	Radiograph of 15% KI
Beam Shape	Collimated	Cone
Spectrum	Monochromatic	Polychromatic
Energy [keV]	9 +/- 0.13	5 < hv < 75
Detector	PIN Diode	Image Plate
Temporal Response	5 s at 2.5 MHz	Single Shot at 20 ns
Measurement Area [μm^2]	5 x 6	44 x 44

Simultaneous High-Speed Radiography and Visible Light Imaging

The measurements were performed at the X-ray Flow Visualization Facility at Iowa State University. The radiographs were produced using an anode voltage and current of 80 keV and 10 mA, respectively. Balancing the design of the x-ray and visible light imaging system was important to optimizing the image fidelity. Both magnification and penumbra will occur when using a source with finite anode size. Maximizing the flux and spatial resolution requires careful placement of the spray between the anode and detector while allowing enough space for the visible light optics. White light from a continuous source was reflected off a thin diffuse reflector, prior to passing through the spray, reflecting off of a thin reflector and into the camera lens. A Photron SA5 was used for the visible light images and synchronized with a Photron SAX2 used to capture the radiographs. An above view schematic is shown in Figure 2-9.

A Lorad LPX 220 tube source with 1.5 mm diameter anode was placed 120 mm from the spray which was 120 mm from the phosphor. Lead shielding, including lead glass windows, is used to protect the camera and intensifier. The CsI phosphor, chosen for its high visible light output, is lens coupled to a LaVision high-speed intensifier fixed to a Photron

SAX2. The Photron CMOS camera collects 12 bit images at 20 kHz with an exposure of 48 μ s. The images are flat field normalized and the transmission levels are converted to equivalent path length (EPL) of liquid using the Beer-Lambert Law and an attenuation coefficient found through calibration. The calibration accounts for all aspects of the imaging system, and the EPL measurements are independent of the sprays local geometry and represent the path averaged mass distribution.

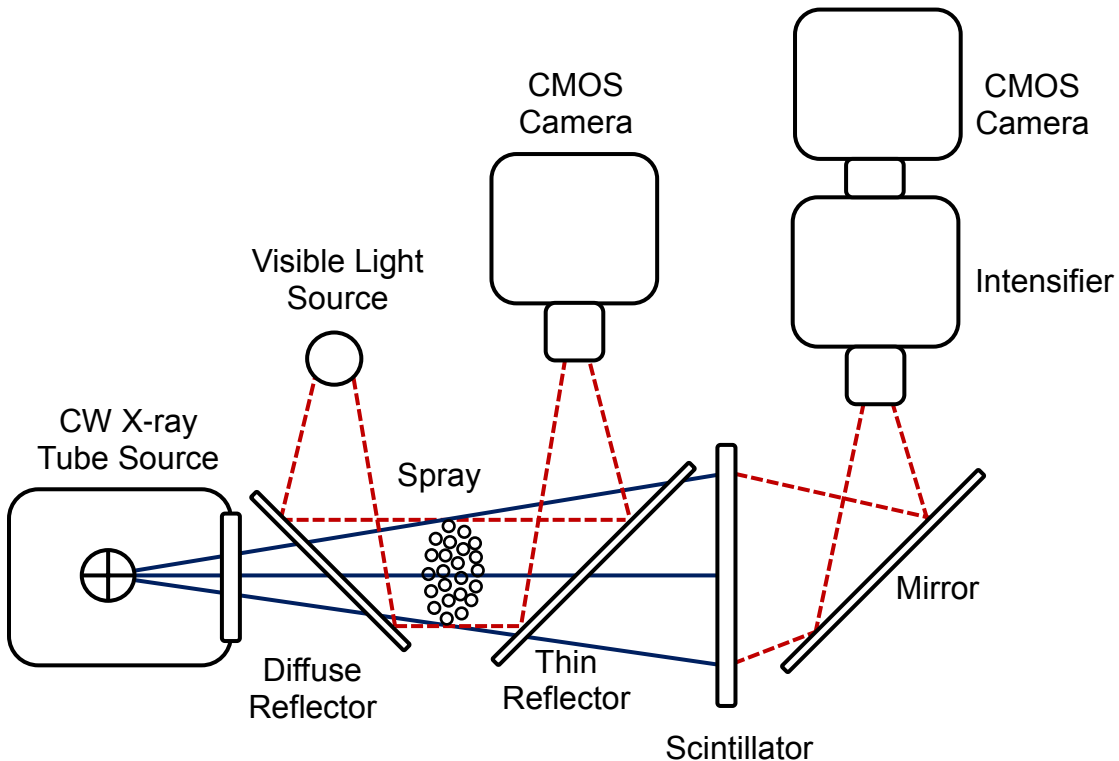


Figure 2-9. Schematic of high-speed radiography and visible light imaging system (top view). Blue solid lines encompass the x-ray cone, red dashed lines encompass the visible light.

The range of x-ray energies from the tube source is between 5 and 80 keV, energies less than 5 keV are absorbed by the windows and in air while no x-rays greater than 80 keV are generated at the given settings. Each photon energy has a respective attenuation

coefficient, and the lower energy x-rays with a greater coefficient are preferentially attenuated. As the beam passes through the spray the average energy of the beam increases and thus the attenuation coefficient decreases. The system must be carefully calibrated to account for the effects of this so-called beam hardening.

The unfiltered spectrum of the ISU tube source is first approximated using Kramers' Law for the broadband bremsstrahlung radiation emitted by an electron hitting a solid target (Kramers, 1923). The spectrum is altered due to the attenuation of the physical system including the source windows air (Figure 2-10).

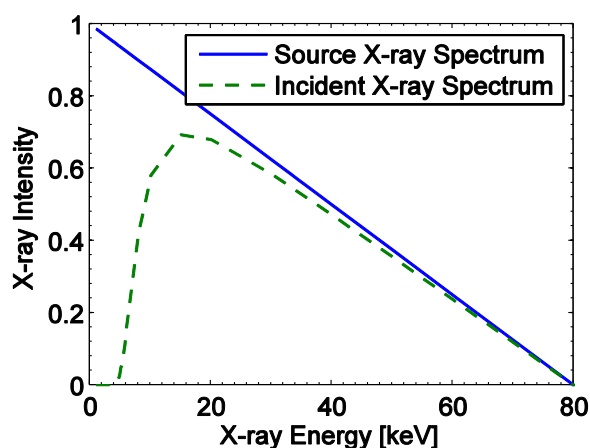


Figure 2-10. Theoretical spectra for the broadband tube source x-rays on a relative intensity scale.

Figure 2-11 shows the spectra of the tube source after passing through 0, 200, and 2000 μm of 50% KI. The spectra are simulated using attenuation coefficients in the NIST tables (Hubbell and Seltzer, 1995). The 0 μm is reduced from the approximated source spectra by the attenuation of the source windows and air.

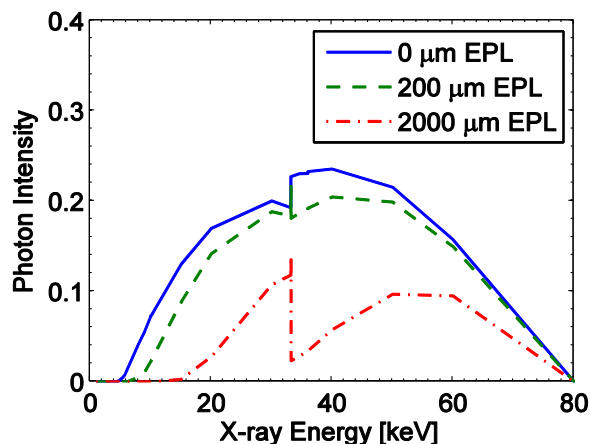


Figure 2-11. Theoretical spectra for the broadband tube source x-rays on a relative intensity scale.

Liquid Mixing

The liquid mixing studies were all made at the APS, due to its narrow beam, both spatially and spectrally. The fluorescence signal is collected with a spectrally resolved diode and the signal is calibrate with the attenuation measurement.

Advanced Photon Source X-ray Fluorescence

Attenuation and fluorescence measurements were conducted at the APS 7-BM beamline, which is a synchrotron bending magnet beamline that creates a nearly collimated, initially polychromatic x-ray beam with high photon flux. The beamline consists of two enclosures, 7-BM-A and 7-BM-B. Enclosure A contains slits and a double multilayer monochromator to condition the beam size and to select a narrow range of x-ray energies, respectively. The monochromator can tune the photon energy from 5.1 to 12 keV ($\Delta E/E = 1.4\%$). Enclosure B houses Kirkpatrick-Baez focusing mirrors (Eng et al., 1998), the spray affixed to a two-dimensional translation stage, and the x-ray detectors to measure attenuation

and fluorescence. A schematic of the enclosures and experiment is shown in Figure 2-12. The total detected x-ray flux is 1.4×10^{11} photons per second in the absence of the spray. A thorough description of the beamline can also be found in Kastengren et al. (2012). Point-wise raster scanning data were collected while the spray was traversed across the incident beam (along the minor axis in Figure 2-12) and at several downstream locations (along the z-axis in Figure 2-12).

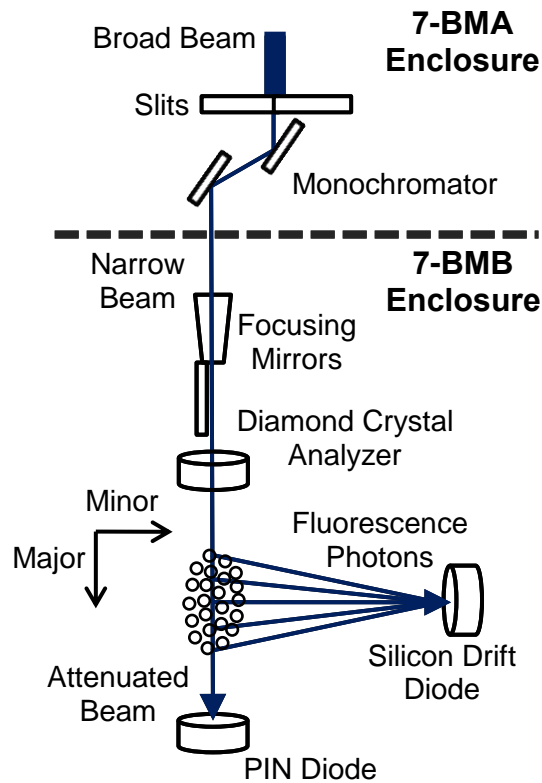


Figure 2-12. Schematic of APS 7-BM enclosures for narrowing and selecting x-ray energy, focusing beam, and detection of attenuation and fluorescence (above view).

Experiments were conducted using either single or dual tracers in each liquid stream and employed photon energies of 10.4 or 10.6 keV, respectively. In each case the x-ray beam was focused to $5 \mu\text{m}$ (vertical) \times $6 \mu\text{m}$ (horizontal) at full width at half maximum (FWHM).

A PIN diode constructed of 300 μm thick silicon and operated without bias voltage PIN was used to detect the transmitted x-ray beam for attenuation measurements. The PIN diode signal was normalized by the diamond crystal analyzer to account for fluctuations in the incident beam. The relative x-ray attenuation along the path of the beam, and hence the amount of liquid along that path, was then measured using Beer's Law. For a monochromatic x-ray beam, Beer's Law can be written as:

$$\frac{I(y, z)}{I_0(y, z)} = e^{-\int \alpha(x, y, z) dx} = e^{-\alpha l} \quad (2-5)$$

where I and I_0 are the attenuated and non-attenuated x-ray intensities measured at the PIN diode, α is the attenuation coefficient, and l is the path length of the x-ray beam through the fluid. In the case where the liquid is not contiguous along the path of x-ray beam, then l is interpreted as an equivalent path length (EPL) of the liquid intersecting the x-ray beam. The attenuation coefficient, α , is the product of the attenuation cross-section and number density of the fluid, which can be considered constant in the case of identical water jets. Changes in attenuation due to the fluorescence tracers are accounted for.

The silicon drift diode (SDD) was used to measure the x-ray fluorescence generated by the interaction of the incident x-ray beam with the spray, as shown in Figure 2-12. The SDD is a photon counting detector capable of discriminating the spectral energy of each incoming x-ray photon with a resolution of 250 eV. The signal of the K_α fluorescence of each tracer element was integrated over a segmented area centered on the peak emission of each tracer. The SDD was placed at approximately $x = 200$ mm from the x-ray beam. The detection of elastic scattering was minimized by detecting at 90° to the excitation beam in the x - y plane. There is no appreciable x-ray fluorescence from water, allowing fluorescence to be

attributable to the specific tracers added to each fluid. Note that the fluorescence signal captured by the SDD at a particular x-ray spectral energy is proportional to the density of the tracer element that fluoresces at that x-ray energy multiplied by the x-ray intensity, which is decaying along the beam path exponentially due to attenuation in water according to Beer's law. The fluorescence signal from each tracer element, therefore, can be directly related to EPL of the liquid originating from each jet integrated along the beam path. Calibration for absolute EPL is achieved by comparing the fluorescence signal in the pure liquid jets measured using the SDD to the attenuation signal using the PIN diode, along with appropriate corrections discussed further below.

A sample spectrum from the SDD constructed by scanning the spray spatially across the incident x-ray beam in the minor axis near the impingement point at $z = 0.5$ mm is shown in Figure 2-13. The signals from each jet are spectrally distinct despite the significant overlap in their spatial distribution and attenuation signal.

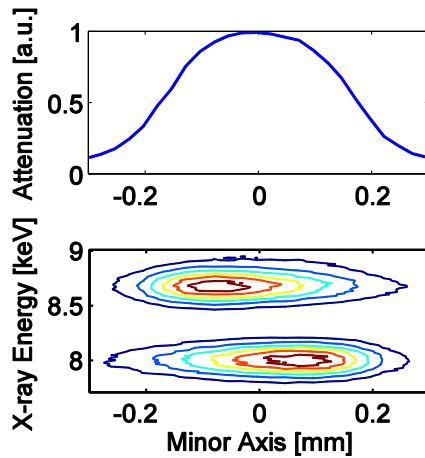


Figure 2-13. Attenuation and fluorescence vs. location at 0.5 mm below impingement point.

Fluorescence Reabsorption Correction Methods

The main uncertainty using this fluorescence technique is the reabsorption of fluorescence photons en route to the SDD. Two methods for error correction are proposed here. The first method, termed the *stereo method*, uses one unique tracer in each fluid and employs stereographic reconstruction to estimate the 3-D shape of the spray and therefore the amount of reabsorption that may occur. In this case, it was not possible to perform an instantaneous radiographic measurement orthogonal to the path of the excitation beam. As such, this approach provides data for reabsorption corrections on a time-averaged basis and is susceptible to uncertainties due to instantaneous fluctuations in the nonlinear, path-length dependent absorption process (see Equation 2-7). The fluorescent tracer elements for the stereo method were chosen to have absorption edges below the energy of the excitation beam (~ 10.4 keV), high fluorescence photon energy (> 8 keV) to minimize reabsorption, good fluorescence yield, and the ability to be easily dissolved in water. The two tracer elements initially included zinc (K-edge energy ~ 8.63 keV) and copper (K-edge energy ~ 8.04 keV) (Thompson et al., 2009) seeded separately into each of the two jets. The second method, termed the *four-salt method*, uses two unique tracers in each fluid. Each tracer from a given fluid emits at a different energy and therefore is absorbed at a different rate. The reabsorption ratio allows for the estimation the path length encountered and a reabsorption correction can be made based on that path length. In the four-salt method, nickel (K-edge energy ~ 7.47 keV) was added to the zinc stream, and cobalt (K-edge energy ~ 6.92 keV) was added to the copper stream (Thompson et al., 2009) to facilitate instantaneous corrections for reabsorption. As shown in Figure 2-14, each pairing maximized the energy ratio so that the fluorescence from one tracer of each pair would be more sensitive to reabsorption than the

other. Hence the ratio of the fluorescence from each pair would enable calculation of the amount of liquid on the path to the SDD. For all measurements, the concentration of each tracer element was 500 ppm by mass, which caused a negligible change in the overall absorption coefficient of the liquids but allowed high fluorescence signal-to-noise ratio.

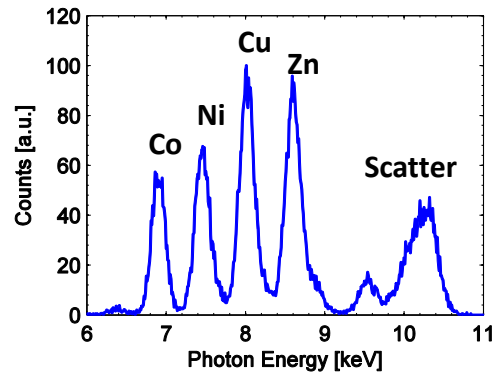


Figure 2-14. Absorption spectrum of different tracer elements seeded into the liquid jets.

As noted earlier, an absolute correlation between the fluorescence data and the quantitative mass distribution of each liquid is obtained through comparison with the attenuation data. The fluorescence signal of each liquid is based on the combined K_{α} lines associated with each tracer present in the spray, and signals from the K_{β} lines are subtracted if they overlap with K_{α} lines. Matrix effects such as zinc K_{α} exciting copper are neglected due to the minute concentrations of the tracer species. The effects of dead-time in the SDD are removed by multiplying the ratio of the input count rate by the output count rate (Walko et al., 2010). The average dead-time was less than 10%, so the dead time corrections are considered minor. To obtain a quantitative fluorescence signal several possible sources of bias error are accounted for through linear corrections, including incident beam attenuation, fluorescence signal reabsorption, and mass conservation. The fluorescence signal from each salt, $F_{salt}(x)$, is corrected for the attenuation of the incident beam, $A(x)$. Reabsorption of the

fluorescence signal, $R_{salt}(x)$, occurs as the fluorescent photons pass through the spray, air, and the window of the SDD. The path length of liquid that the signal is reabsorbed through is the, $RPL(x,y)$ which varies for each location. The correction is based on the $RPL(x,y)$ determined through stereographic reconstruction or the four-salt method, as shown in Equation 2-6:

$$R_{salt}(x) = \frac{1}{N} \sum \frac{m(x,y)}{M} e^{-\alpha_{salt} RPL(x,y)} \quad (2-6)$$

where $R_{salt}(x)$ is determined by Beer's Law given the attenuation coefficient of the emitted x-ray energy and reabsorption path length $RPL(x,y)$ weighted by the local mass $m(x,y)$, divided by the total mass M , and averaged over N pixels in the x direction. The methods differ in how the value $RPL(x,y)$ is determined.

Figure 2-15(a) shows the results of the arithmetic reconstruction technique used to estimate the z -slice of the spray. From each slice the $RPL(x,y)$ can be weight-averaged along y for each data point. The four-salt method uses the ratio between the absorption of the fluorescence signals from each of the two tracers in the given fluid. An example of the calculated ratio, R , is shown in Figure 2-15(b).

A mass conservation coefficient, M_{salt} , is applied to balance measured mass of each fluid with the mass measured through attenuation. Equation 2-7 displays the equality of mass in each jet with the total attenuation mass in terms of spatially integrated EPL. Each correction is applied at each x location, except the mass conservation coefficient, which is a global value used at all x and z locations.

$$M_{Cu} \int A(x) R_{Cu}(x) F_{Cu}(x) dx = M_{Zn} \int A(x) R_{Zn}(x) F_{Zn}(x) dx = 0.5 \int EPL(x) dx \quad (2-7)$$

The final fluorescence signal is a quantitative measurement of the mass distribution of each liquid presented as the EPL. The reliability of the corrections can be tested by

comparing the symmetry of the fluorescence signals and quantitatively by comparing the sum of the EPLs of the individual fluids (fluorescence measurement) with the total EPL (attenuation measurement).

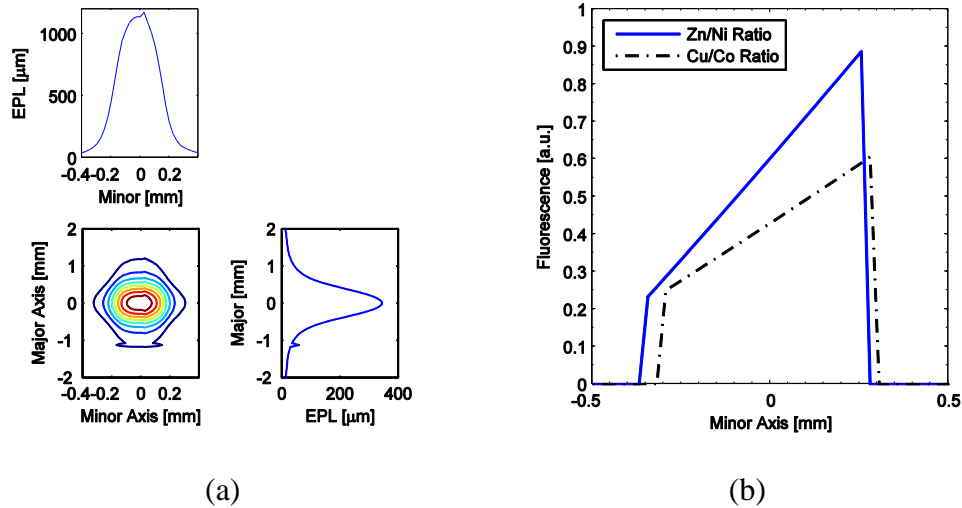


Figure 2-15. Figures displaying reabsorption correction methods. (a) Shows EPL line plots at the same horizontal location with the spray traversed in the minor axis (upper left) and the major axis (lower right), shown in the lower left is a stereographic reconstruction of the spray used to estimate the reabsorption path length. (b) Shows the ratio of Zn signal to Ni signal, and Cu signal to Co signal, these ratios are used to determine the reabsorption path length.

Two nearly identical mixing measurements were conducted at separate times. In the first measurement effort, each fluid was doped with one salt ion and utilized radiographic data for stereographic reconstruction. The second measurement effort used two tracers in each fluid with four salt ions total. The measurements were collected with the same injector conditions.

The spatial resolution of the raster scans was limited by the selected point spacing of 25 μm. Noise in the attenuation and fluorescence signals was determined by the signal's

standard deviation in the flat field where no spray is present. The noise values equate to EPL values of $0.4 \mu\text{m}$ and $0.8 \mu\text{m}$ for the attenuation and fluorescence signals respectively. This gives rise to maximum signal-to-noise ratios (SNR) of 2300:1 and 800:1 for the attenuation signal (used for calibration) and fluorescence signal (used to measure the mass distribution of each liquid), respectively. In the results and discussion, the attenuation signal is used to represent the total EPL during the mixing process, while the fluorescence signal indicates the EPL of the zinc-seeded or copper-seeded fluid.

Spray System

Several spray systems were used in conjunction with the impinging jet injector based on the needs of the experiment. The low pressure system is used for liquid sprays, an infinite flow loop was used for radiographic measurements, and a two liquid system was used for the fluorescence measurements.

Like-Doublet Impinging Jet Injector

The injector used in all the studies was a like-doublet impinging jet injector. The spray is generated by two like jets (same fluid, same diameter, same velocity) impinging each other at an included angle of 2θ , with the distance between the injector and impingement point defined as the free jet length, and at a prescribed velocity. The nozzle orifices have diameters that range from 0.5 to 1.5 mm depending on the experiment. The impingement angle is nominally 60 degrees, but is varied in the water mixing study. The Reynolds number is varied from 1800 through 12200, depending on the experiment. The liquids used are water, KI solutions, and water with fluorescent tracer salts. Figure 2-16 displays photographs of the

impinging jet injector, (a), used in the x-ray measurements, mounted on a base that allows rotation, (b), to view different angles of the spray, and mounted on the rotational and translational mounts, (c), to vary the included angle of the impinging jet spray and the free jet length to diameter ratio.



(a)

(b)

(c)

Figure 2-16. Photograph of the (a) impinging jet injector, (b) the injector mounted on rotation mount to view different angles of the spray, and (c) the injector mounted on the rotational and translational mounts to vary the included angle of the impinging jet spray and the free jet length to diameter ratio.

The backlit image in Figure 2-17 shows a time-resolved visualization of the impinging jet spray under investigation. The major and minor axes correspond to the overall elliptical pattern of the spray. Key locations in the spray are bracketed including the impingement region, sheet formation, liquid breakup, where turbulent dispersion would occur, and potential chemical reactions. In the case of hypergols, vaporization is nearly instantaneous and reactions may occur anywhere along the spray.

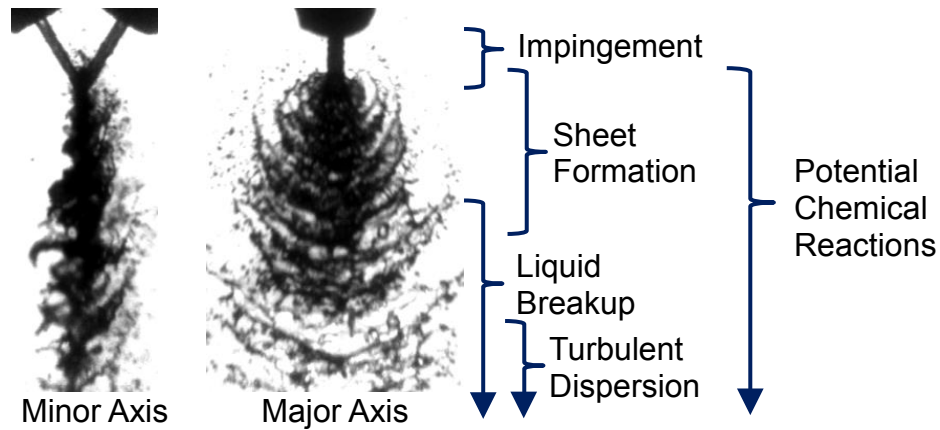


Figure 2-17. Orthogonal visible backlit images of the impinging jet spray at 60 degree included angle, 3.5 mm free jet length, and Reynolds number 9400.

Low Pressure Spray System

Two low pressure spray systems were used to flow water and salt solutions for the liquid spray experiments. An infinite loop system was designed to run for long spray experiments including x-ray CT scans which could take 20 or more minutes, Figure 2-18. Diagramed in Figure 2-18 the flow system was pressurized by a twin gear pump, and the flow rate was adjusted by the pumping pressure and balanced by two rotometers. A spray catch bucket collected the liquid and fed the pump closing the loop. At higher flow rates the liquid was well atomized and several methods to contain the liquid were adapted. The first used low absorbing kapton windows, which were kept dry by air jets, the windows were necessary for tube source imaging. When taking synchrotron measurements, a much smaller beam path was necessary so small pipes replaced the windows, the pipes were fed with air to keep droplets from collecting inside.

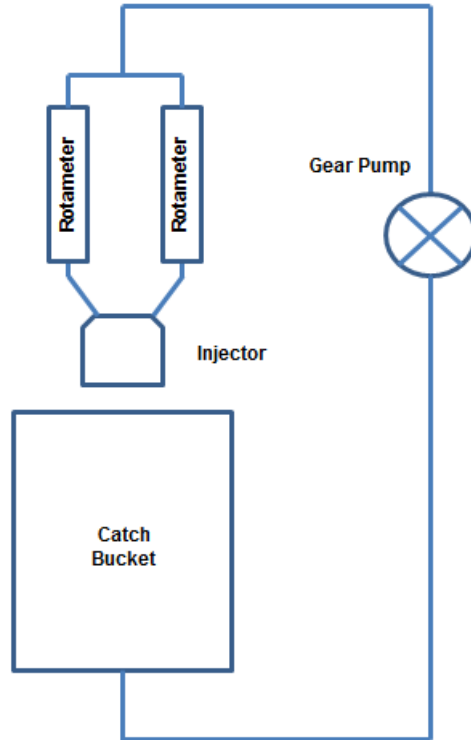


Figure 2-18. Infinite loop spray system with twin gear pump.

It was not feasible to use an infinite spray loop for the liquid mixing measurements. Once the two liquids mixed the salts had to be filtered out and new salts were added to separate reservoirs. Therefore the mixing measurements used a pressure fed system with two large 20 L reservoirs with remotely operated solenoid ball valves, Figure 2-19. The system would work with separate fluids and have a sufficiently long run time. Again the flow was equalized and adjusted with two rotometers.

The low pressure systems were safe and easy to run with a max flow pressure of 675 kPa. Details in running these systems can be found in Appendix B.

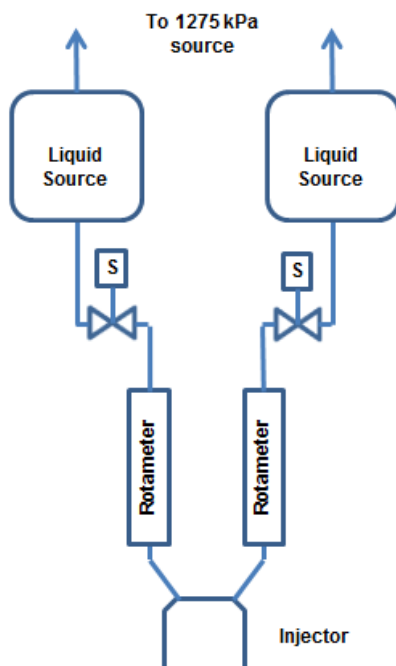


Figure 2-19. Low pressure twin fluid spray system, with remotely operated solenoid valves.

High Pressure Spray System

To provide enough pressure to flow the high viscosity gels such as the glycerol and gel solutions a high pressure spray system was designed and built in collaboration with Purdue University, Figure 2-20. Two very high pressure (28 MPa) piston pumps were coupled to the control valves and injector with thick walled stainless steel tubing. The piston pumps were pressure driven from a high pressure source, usually a high pressure gas bottle to decrease the number of times it needed to be exchanged. The system was controlled via pressure actuated solenoid valves that were controlled remotely. The flow rate was controlled by the feed pressure and the velocity was measured through the displacement of the pressure cylinder pistons that were directly coupled to linear potentiometers.

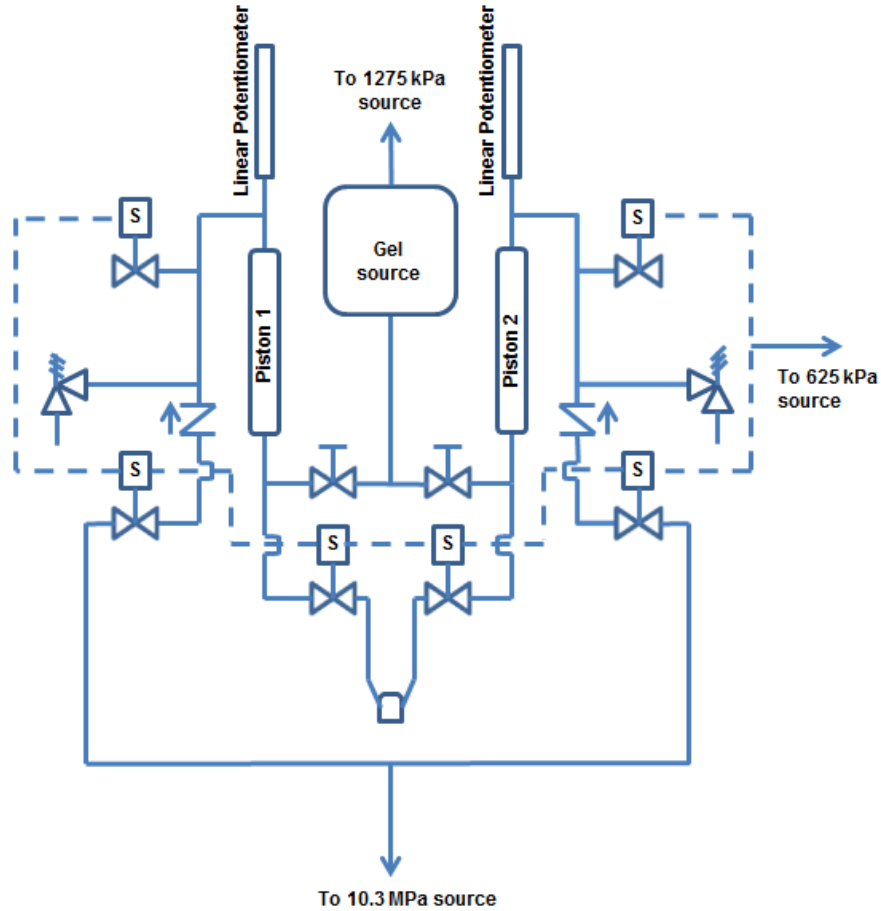


Figure 2-20. High pressure twin fluid spray system, with remotely operated pressure actuated solenoid valves.

The high pressure spray system was run up to 10.3 MPa so safety was a natural concern. A procedure is in Appendix B on how the system was run to maximize safety.

CHAPTER III

RESULTS AND DISCUSSION

Mass Distribution

This chapter examines the data collected and the results of the experiments pursued by the author. X-ray radiography is used to measure the mass distribution within the impinging jet sprays. The attenuation of the x-rays is converted to an equivalent path length (EPL) through the use of the Beer-Lambert Law. This measurement technique is ideally suited because the attenuation of x-rays is very weakly affected by refraction and scatter. This allows for the direct measurement of mass anywhere in the spray independent of local geometry.

Two important notes are that the x-ray sources vary during the course of this chapter and they include the previously mentioned synchrotron source at ANL used to validate the tube sources, measure the mass distribution in non-Newtonian fluids, and the CW and flash tube sources used for laboratory scale measurements for time averaged, time-resolved, and high-speed x-ray measurements. The second notice is that the location of impingement is defined as where the centers of each jet would meet in space. This impingement location is defined as the 0 mm location and any locations above this are described as upstream and negative and below impingement is described as downstream and positive, e.g. the location in the liquid sheet 1 mm from the point of impingement would be defined as the downstream location 1 mm below impingement.

Time Averaged Tube Source Validation

Initial verification regarding the potential effects of beam hardening for the broadband tube source was first obtained by measuring the attenuation coefficient in a plastic cuvette for a range of KI concentrations. As shown in Figure 3-1, the attenuation coefficient increases linearly with the concentration of KI, with the linear range representing the conditions under which beam hardening is minimal. The measurements of the attenuation coefficient, α , in Figure 3-1 were conducted using a path length of 0.5 mm and show a linear relationship with KI concentration up to 20% by mass. Since the spray used in the current study has an EPL of less than 0.5 mm, it is anticipated that beam hardening will be negligible for these conditions. For higher EPL, which are of interest for other spray applications, beam hardening may play a larger role. This is the case for the path length of 10 mm also shown in Figure 3-1. In this case, as the KI concentration increases, the attenuation coefficient begins to saturate, again because the softer x-rays are preferentially absorbed and the remaining harder x-rays propagate with reduced attenuation. In previous work by Meyer et al. (2008, 2010), it was estimated that a path length of 10 mm and a KI concentration of 15% was sufficient to avoid the effects of beam hardening. Indeed, the data in this range can be fit to a linear function with a fair degree of accuracy, as shown in Figure 3-1; however, the slope of the attenuation coefficient for the 10 mm path length is certainly lower than the case for 0.5 mm. This illustrates the importance of utilizing very short path lengths to ensure the absence of beam hardening, even if the attenuation coefficient is varying approximately linearly with KI concentration. Hence, the current data implies that a KI concentration of only 5-10% is possible for sprays with EPL values of 10 mm or greater before beam hardening becomes significant. Furthermore, it is possible to estimate that beam hardening for a path length of

0.5 mm will be negligible for KI concentrations of at least 50% by mass, or conversely, that beam hardening will be negligible for path lengths of ~ 1.67 mm or less for a KI concentration of 15%, a limit that is $\sim 5\times$ larger than the path lengths studied in the current work.

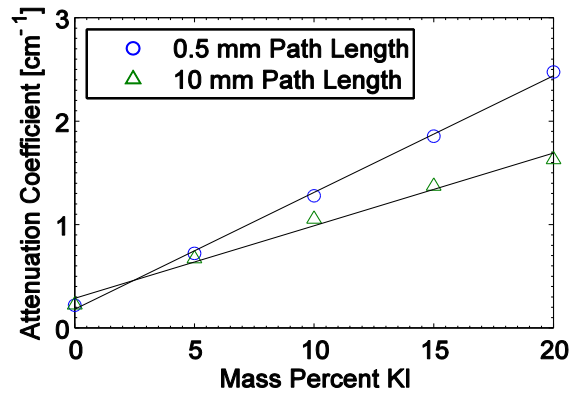


Figure 3-1. Measured attenuation coefficient showing no effect of beam hardening for a 0.5-mm path length with KI concentrations up to 20% by mass in distilled water. Lines are linear fits to the data.

Once the attenuation coefficient, α , is known, radiographs before and after a spray can be used to produce 2-D images of an equivalent path length (EPL) of liquid along the line of sight. Although it is not possible to determine if the liquid is contiguous along the path traversed by the x-rays, it is possible to obtain a time-averaged, planar map of EPL, which is a projection of the 3-D liquid mass distribution onto a plane. Since the impinging jet spray in this case spreads laterally in the imaging plane, this gives an indication of the approximate thickness of the liquid sheet. By rotating the source and detector 360° around the spray, it is furthermore possible to produce a CT scan, not just of the EPL, but of the time-averaged 3-D liquid mass distribution (Barrett and Swindell, 1981; Hsieh, 2003).

In the discussion that follows, x-ray attenuation data are shown with the liquid jets consisting of distilled water. No additive is used for the APS-based images as the softer x-rays allow significant attenuation with water alone. In the case of the broadband source, mass concentrations of 0% and 15% KI in distilled water are selected for the 2-D radiographs, and 15% KI in distilled water is selected for the CT scans. According to the data in Figure 3-1, adding 15% KI by mass increases the attenuation coefficient by a factor of 7.5 over distilled water alone.

Displayed in Figure 3-2 is the spray used in the comparison of the x-ray sources and techniques. The time resolved image details the main features of the spray including the dense impingement region, the unsteady and thin liquid sheet and the surrounding droplet field. The like-doublet impinging-jet injector has an included angle of 60 degrees, orifice diameters of 508 μm and a jet velocity of 8 m/s and the Reynolds numbers are 4160 for 15% KI and 4080 for pure water.



Figure 3-2. Visible image of spray used in comparison of x-ray sources and techniques.

Figure 3-3 shows images of the impinging jet spray from the APS and the ISU x-ray tube source from upstream of the impingement region to a location 14 mm below the orifice tips. In all images, including the raster scan from the APS in Fig. 3-3 (a), darker regions of the spray indicate higher levels of attenuation and longer equivalent path lengths of liquid through the spray. The EPL values at 3, 6, 9, and 12 mm below the orifice tips are compared quantitatively in Table 3-1 as well as in the line plots that follow in Figures 3-4 through 3-7, respectively. As noted earlier, the raster-scan data from the APS has a minimum distance of 50 μm between measurement locations, which was deemed sufficient to capture the main features of the spray liquid distribution. If necessary, a smaller spacing could be used, at the expense of more time-consuming measurements.

Note that the tube source radiograph with 0% KI in Figure 3-3(b) displays significantly higher noise within the spray than for the case with 15% KI in Figure 3-3 (d) due to the higher attenuation coefficient for the KI solution. Figure 3-3 (c) shows contour plots that represent cross-sections through the spray from the CT scan at 3, 6, 9, and 12 mm downstream. A quantitative comparison of the centerline EPL for both the APS and broadband tube source is shown in Table 3-1, along with error (using APS data as the standard), the spatial resolution, attenuation coefficient, EPL standard deviation, and SNR at each downstream location. These data will be referenced while describing the quantitative line plots shown in Figure 3-3.

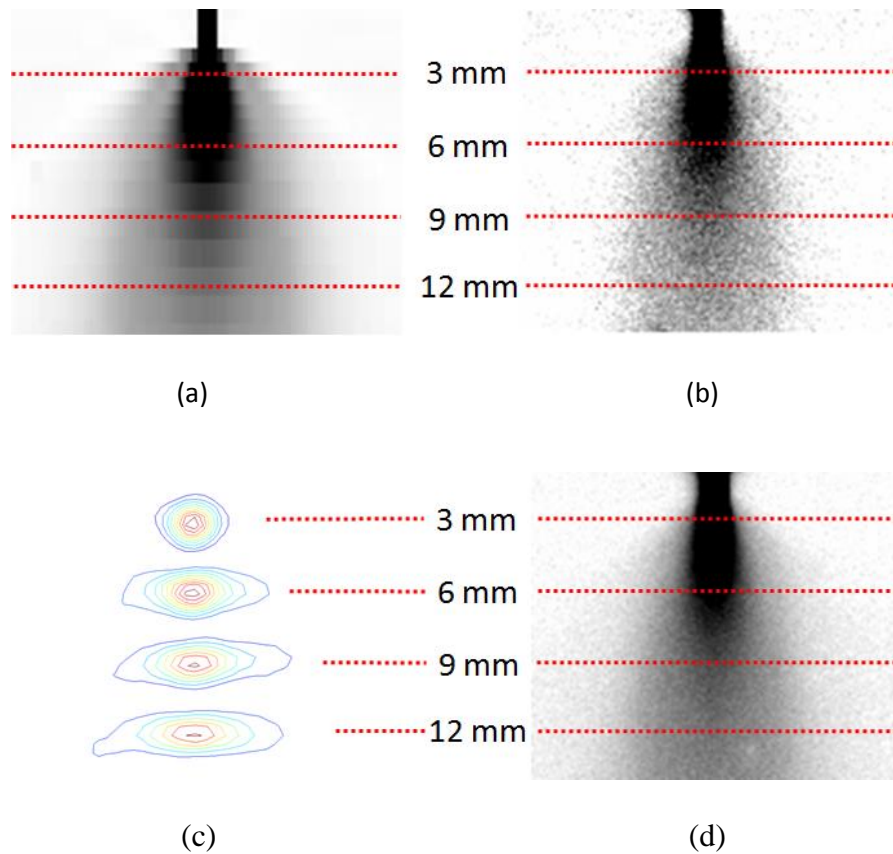


Figure 3-3. Comparison of (a) APS raster scan attenuation data with broadband attenuation data, (b) ISU radiograph of distilled water, (c) ISU CT slices of distilled water and 15% KI, and (d) ISU radiograph of distilled water and 15% KI.

For the line plot at the 3 mm location downstream, shown in Figure 3-4, the attenuation data collected at the APS displays the highest SNR, with a smooth curve even along the base line. The EPL measured at the jet centerline is $\sim 310 \mu\text{m}$, and the horizontal width is $\sim 1 \text{ mm}$ (FWHM). Given the EPL standard deviation of $0.3 \mu\text{m}$, indicated in Table 3-1, and the $50 \mu\text{m}$ spacing of the APS raster scan, then the thickness of $310 \mu\text{m}$ and width of 1 mm is likely representative of the actual time-averaged liquid mass distribution across the spray.

Table 3-1. Comparison of x-ray imaging results from the APS and tube source data.

Source		APS	ISU Tube Source		
Imaging Method		Raster Scan of Water	Radiograph of Water	Radiograph of 15% KI in Water	CT Scan of 15% KI in Water
10-90% Rise [μm]		40	800	800	~1400
Atten. Coeff. [mm^{-1}]		0.533	0.0248	0.196	0.196
EPL Std. Dev. [μm]		0.3	8	3	0.5
3 mm	EPL [μm]	308	268	276	212
	SNR	1028	34	92	425
	Error [%]		13	10	31
6 mm	EPL [μm]	102	106	100	96
	SNR	339	13	33	192
	Error [%]		4	2	6
9 mm	EPL [μm]	68	66	62	68
	SNR	225	8	21	136
	Error [%]		3	8	1
12 mm	EPL [μm]	51	49	51	54
	SNR	171	6	17	109
	Error [%]		4	<0.5	5

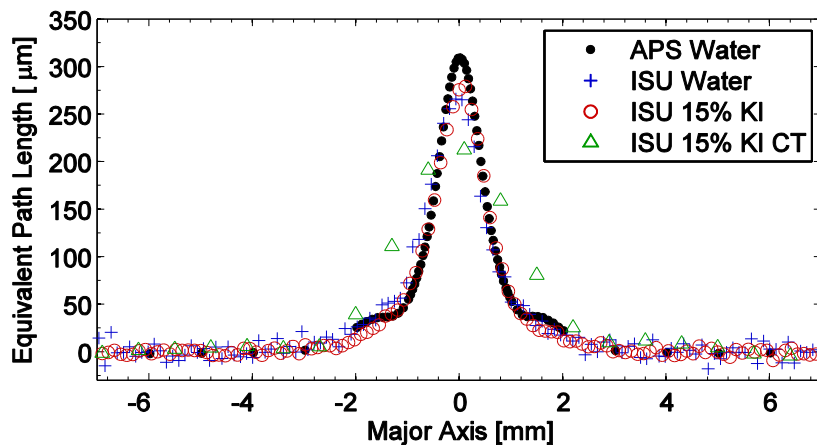


Figure 3-4. Line plot across the impinging jet at 3 mm below injector for the APS and broadband tube source data.

The lower SNR for the tube source (ISU) data is apparent in the wings of the line plots in Figure D, displaying larger deviations from the zero baseline at locations further from the jet centerline with and without KI. Nonetheless, the SNRs for the radiographs with and without KI are sufficient to capture the primary features of the flow, including the spray width and the shoulders near the edge of the spray. Despite this fairly high SNR, the tube source radiograph data show centerline EPL values that are ~10% lower than the APS measurement. Given that the 10-90% rise for the 2-D radiographs is 800 μm , however, it is likely that this error is due to blurring of the spatial profile of the 1-mm wide spray at this location. Indeed, the width of the spray for the tube source data is slightly larger than that of the APS source, as shown in Figure 3-4.

The effect of resolution is particularly apparent in the tube source CT scan data, which shows a centerline EPL of only ~212 μm , or 31% below that of the APS data in Table 3-1. Correspondingly, the width of the spray is measured by the CT scan to be about 2.8 mm, which can be interpreted as the limiting resolution from the reconstruction algorithm given that the width is known to be closer to 1 mm. Because of this spatial averaging and because this reconstruction algorithm the CT scan data have much higher SNR (~425:1) than the tube source radiographs for water (34:1) and water with 15% KI (92:1), although not as high as the APS data (1028:1).

Line plots across the spray at 6 mm below the injector are shown in Figure 3-5. At this downstream location, the equivalent path length through the spray drops threefold from 310 μm to about 102 μm as the liquid sheet spreads laterally in the plane of the image. In this case, all data sets show similar reductions in their respective SNR's because of the significant decrease in absorption through the spray (see Table 3-1). Nonetheless, the excellent

agreement between the APS and tube source data with and without the use of KI lends confidence that the addition of up to 15% KI does not appreciably affect the time-averaged liquid mass distribution, nor does it lead to significant beam hardening in this particular spray. It is also encouraging that all tube source techniques were capable of measuring an EPL as low as 100 μm , although it is important to also keep in mind that the spatial resolution will need to be improved for capturing detailed spray features in the plane of the image. As the width of the spray has also increased threefold, however, in this case the 2-D radiographs and 3-D CT scan nearly fully resolve the width of the spray, as shown in Figure 3-5.

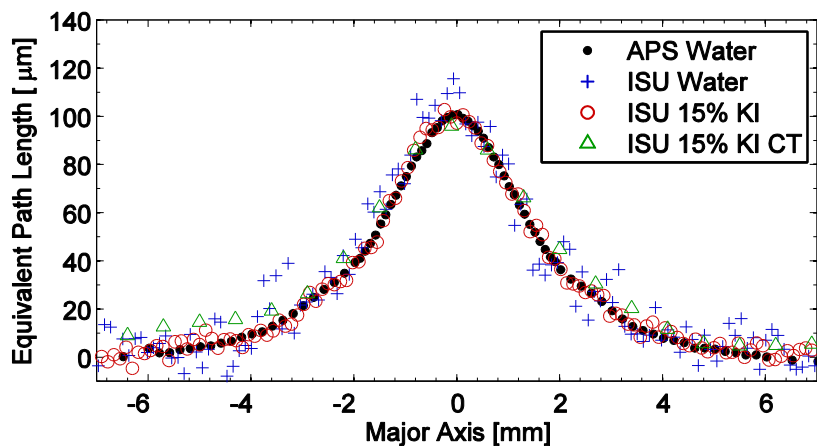


Figure 3-5. Line plot across the impinging jet at 6 mm below injector for the APS and broadband tube source data.

At 9 mm below the injector, shown in Figure 3-6, the shape of the spray continues to spread in the plane of the image, and the measurements from both the 2-D radiographs and 3-D CT scan are fully resolved. All four measurement techniques show nearly an equivalent path length that agrees with the APS data to within experimental error, and the overall trend is well captured. The SNRs for the tube source radiographs, however, have decreased

substantially down to 13:1 for the case without KI. For the case with 15% KI, the SNR is still fairly reasonable at 33:1, as shown in Table 3-1. Since the 3-D CT scan is now fully resolved, it provides a quantitative volumetric map of the time-averaged liquid mass distribution, as verified by the APS data. However, the right side of the plot shows the CT data not approaching the zero baseline as quickly as the other measurements. The CT data contains not only noise from the source, spray, and detector, but also artifacts from the algorithm used to calculate the voxel values as well as potential artifacts from the chamber walls that can be responsible for this disagreement for low levels of attenuation. Hence, the experiment must be carefully designed to minimize these sources of error in regions with low x-ray attenuation.

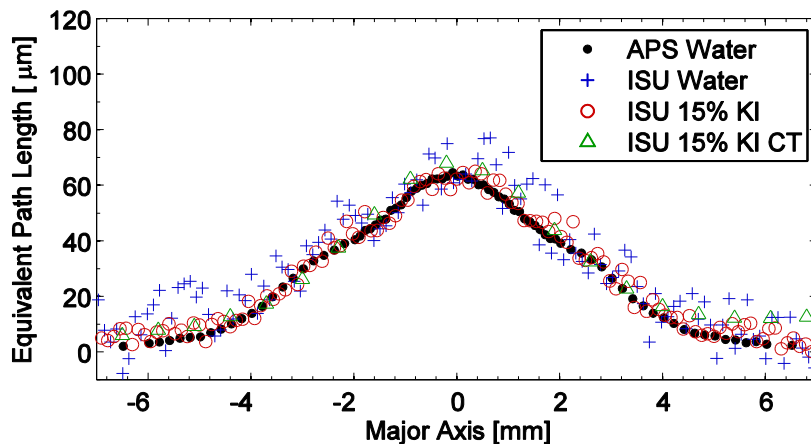


Figure 3-6. Line plot across the impinging jet at 9 mm below injector for the APS and broadband tube source data.

Line plots of the liquid mass distribution at 12 mm below the injector tips is shown in Figure 3-7, with the spray spreading further in the plane of the image and the EPL dropping down to about 50 μm . In this case the shape of the liquid profile has changed from having a prominent central peak to having a broad spatial distribution near the centerline. Indeed, the

images in Figures 3-3 (b) and 3-3 (d) show that 9 mm appears to be on the lower edge of a liquid core, whereas the line plot across 12 mm is in a broad diffuse part of the spray, signifying that break-up of the liquid core is common between 9 and 12 mm downstream of the jet exit. All the measurement approaches appear to capture this change to a broad spray profile and are able to capture the EPL to a high degree of accuracy. However, the lower SNR's for the 2-D radiographs place a limit on the precision of the EPL measurements. At the 9 mm location, the SNR is 8:1 for the 2-D radiographs without KI and 21:1 for the 2-D radiographs with 15% KI. This noise limit can be overcome by increasing the number of frames averaged and, for the current data, very nearly follows one over the square root of number of frames, as expected for random error.

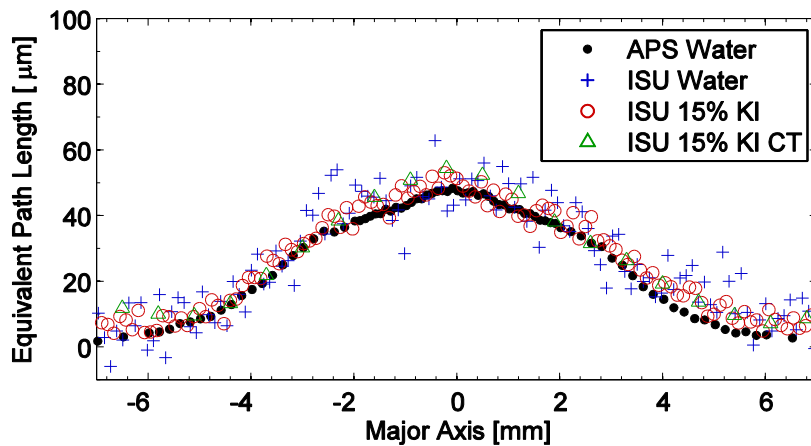


Figure 3-7 Line plot across the impinging jet at 12 mm below injector for the APS and broadband tube source data.

For cases with and without KI, this noise limit is taken to be about five times the standard deviation. Strong evidence for this is shown in Figures 3-5 through 3-7 for EPL data away from the centerline. By reviewing these data, it is possible to see that the broadband tube source is capable of tracking EPL values accurately down to 15 μm for the case of 2-D

radiographs and 3-D CT scans with 15% KI. This indicates that the use of broadband tube sources for measuring the 2-D or 3-D liquid mass distributions in many atomizing sprays of practical interest is very promising. For example, the rocket sprays studied by Schumaker et al. (2012) have EPL values up to about 500 μm with a spatial extent of 20 mm or more. The low EPL is due to the spray being well atomized and distributed over a wide area for effective distribution throughout the rocket combustion chamber. In such a case, the data presented here clearly indicate that the time-averaged 2-D or 3-D liquid mass distribution in such a spray could be accurately measured using a broadband tube source. The same conclusion might also be drawn for a wide range of sprays for combustors in gas-turbine, heating, and power generation applications, albeit keeping in mind that 2-D spatial features less than ~ 0.5 mm and 3-D spatial features less than ~ 3 mm would not be fully resolved without further improvement in the tube source x-ray imaging system. This work also highlights the advantages of the soft, narrowband x-rays available at the APS, which combine high SNR with excellent spatial resolution to enable accurate measurements of both small and large features of atomizing sprays without the use of a contrast enhancing agent. The close agreement of the data between the different x-ray tube source techniques and the APS data at various locations within the spray indicate that the APS can be used as a calibration standard for validating measurements using less ideal x-ray sources.

Time Resolved Flash Source Validation

Further verification of the flash tube sources for time-resolved radiography are presented in this section. The 5 s time trace of the transmission signal from the PIN diode at the APS is partitioned 50 times to lengths of 0.1 seconds, creating a minimum resolvable

frequency of 10 Hz. A second-order Butterworth filter with 250 kHz cutoff frequency conditions the signal resulting in a maximum Nyquist frequency of 125 kHz. This bandwidth produces a dynamic range of 12,500, and encompasses the temporal behavior of the spray. Due to the monochromatic x-ray beam and point detector, the EPL could be determined through a simplified version of Beer's Law, as shown in Equation 3-1, where α is the attenuation coefficient determined from calibration with samples of known liquid path length. The normalized transmission, τ , is computed from the measured intensity transmitted through the spray, I , normalized by the measured intensity transmitted without the spray, I_0 .

$$\frac{I(y, z)}{I_0(y, z)} = \tau = e^{-\alpha EPL} \quad (3-1)$$

Values of the EPL where measured at specific locations in the spray, the results presented here are taken from the centerline starting just below the injector tips and moving down through the breakup of the liquid sheet. The segmented time traces are used to calculate the time-averaged statistics and the power spectral density (PSD). The PSD was determined through a discrete fast Fourier analysis employing a Hann window to reduce aliasing from edge discontinuities. Fifty individual time traces are used to produce an ensemble averaged PSD.

When collecting radiographs using a tube source, the dependence of the attenuation coefficient on photon energy, $h\nu$, becomes relevant. The relationship between the transmission and the EPL is now dependent on the convolution of energy dispersion and the detector response function, ψ , as shown in Equation 3-2. To simplify Equation 3-2, which contains parameters that are difficult to measure in practice, a simple model with an

attenuation coefficient linearly dependent upon transmission is used, as shown in Equation 3-3.

$$\tau = \frac{\int e^{-\int \alpha(h\nu, x, y, z) dx} \psi(h\nu) dh\nu}{\int \psi(h\nu) dh\nu} \quad (3-2)$$

$$\tau = e^{-[m\tau + b]EPL} \quad (3-3)$$

Determining the variable attenuation coefficient is crucial for measurement accuracy. To capture the variation in the coefficient over a range of path lengths and thus transmission levels, a transmission vs. coefficient study was conducted. Sixteen liquid jets of varying diameter were imaged. The averaged transmission through each jet is compared to the averaged path length of each jet. Knowing the transmission and path length allows for determination of the coefficient. This coefficient is then plotted against the averaged transmission, as shown in Figure 3-8. A linear fit of the points is used as the variable attenuation coefficient to calculate the unknown EPL in sprays of interest. This method is subject to the shape of the jets and uncertainty in the calibration data and does not fully capture the non-linear behavior seen in the modeled attenuation coefficient.

Using cylindrical jets as a “step wedge” does incur a small error because the cylindrical jet is not of constant thickness, and attenuation is nonlinear. This causes an overestimation error less than 1.5% for path lengths under 2 mm.

The linear fits have an uncertainty of 11% for water and for 15% KI. This can be due to a number of factors including but not limited to noise, changes in tube anode output, and changes in image plate behavior. This uncertainty in the calibration data does not allow for a curvilinear fit. The model of the attenuation coefficient agrees with the calibrated coefficient

to within 11% and 13% on average for path lengths less than 2 mm for water and 15% KI, respectively. The largest error in the model is likely from the approximated input spectrum.

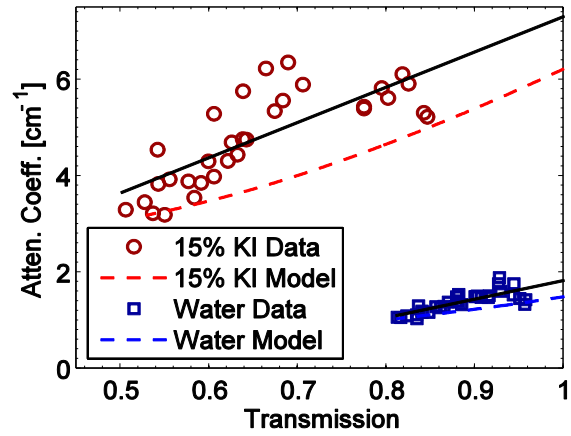


Figure 3-8. Comparison of the empirical and modeled attenuation coefficients vs. transmission for 15% KI and water. Linear trend lines are used for the attenuation coefficient in Equation 3-3.

The like-doublet impinging-jet injector has an included angle of 60 degrees. The injector orifices have diameters of $D = 510 \mu\text{m}$ and length-to-diameter ratios of 46 with chamfered inlets. A gear pump drives the liquid at impinging jet exit velocities of 3.5 m/s and 8 m/s, as shown by the visible-light, backlit images in Figure 3-9(a) and Figure 3-9(b), respectively. The two jets approach the impingement zone in the plane perpendicular to the plane of the image. The jets meet roughly 3 mm below the injector tips. The 3.5 m/s spray forms a semi-stable liquid sheet with most of the liquid occurring in the rim. The unstable 8 m/s spray forms a wavy sheet with a disintegrating rim. The 15% KI used to increase contrast introduced a change in fluid properties, but the kinematic viscosity, ν , for 15% KI ($0.98 \times 10^{-6} \text{ m}^2/\text{s}$) is nearly the same as that for pure water ($1.00 \times 10^{-6} \text{ m}^2/\text{s}$). This allows for a near match of both the jet velocity, V , and the Reynolds number based on jet diameter, $Re_D =$

VD/v . For jet velocities of 3.5–8 m/s, the Reynolds numbers are 1820–4160 for 15% KI and 1790–4080 for pure water.

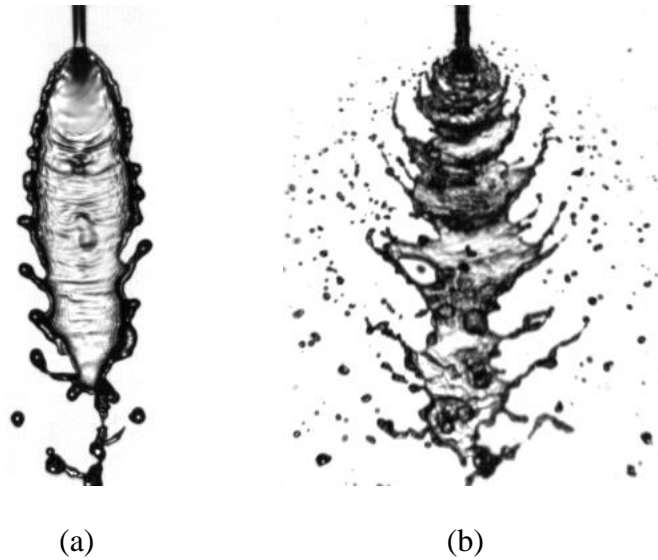


Figure 3-9. Visible light images of the impinging jet sprays used in the comparison of x-ray sources and techniques for jet-exit velocities of 3.5 m/s (a) and 8 m/s (b).

Radiographs of the impinging jets using the flash x-ray source are shown in Figure 3-10 for the low and high Reynolds number conditions. Two instantaneous flash x-ray radiographs of each condition are shown to elucidate the typical behavior. The lower Re condition (3.5 m/s) is characterized by the stable liquid jets impinging at about 3 mm below the jet exit and forming a quasi-stable liquid sheet encompassed by a pronounced rim. The dark regions of the radiograph represent the thicker regions of the spray, occurring in the impingement region, in the rims, and during the formation of rim instabilities. The impact waves with varying amplitude perturb the liquid sheet, leading to variations in the EPL along the centerline. Further downstream, the liquid sheet collapses as the rim breaks into larger droplets at around 12 mm below the jet exit. Increasing the velocity to the high Reynolds

number condition (8 m/s) generates turbulence in the liquid jets resulting in a wider unstable liquid sheet with no pronounced rim structure. Here the impact waves lead to much larger perturbations of the liquid sheet thickness, as well as the early onset of secondary breakup into smaller droplets. Further downstream at about 12 mm, the sheet does not coalesce, but rather breaks into ligaments and subsequent droplets as the impact waves spread radially outward. The flow conditions shown in Figure 3-10 provide a wide range of spatio-temporal features for comparison between the flash and APS x-ray sources.

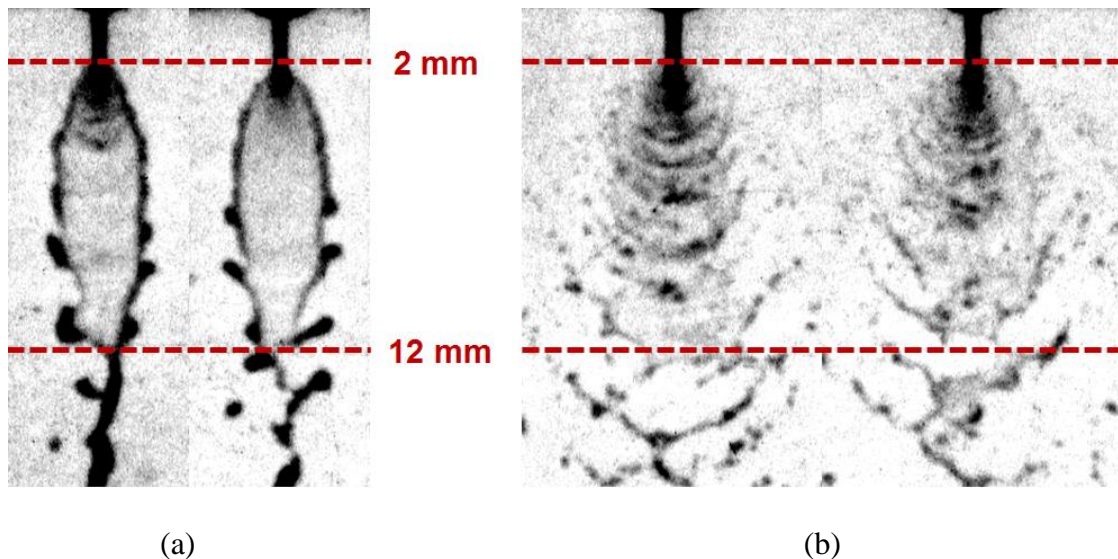
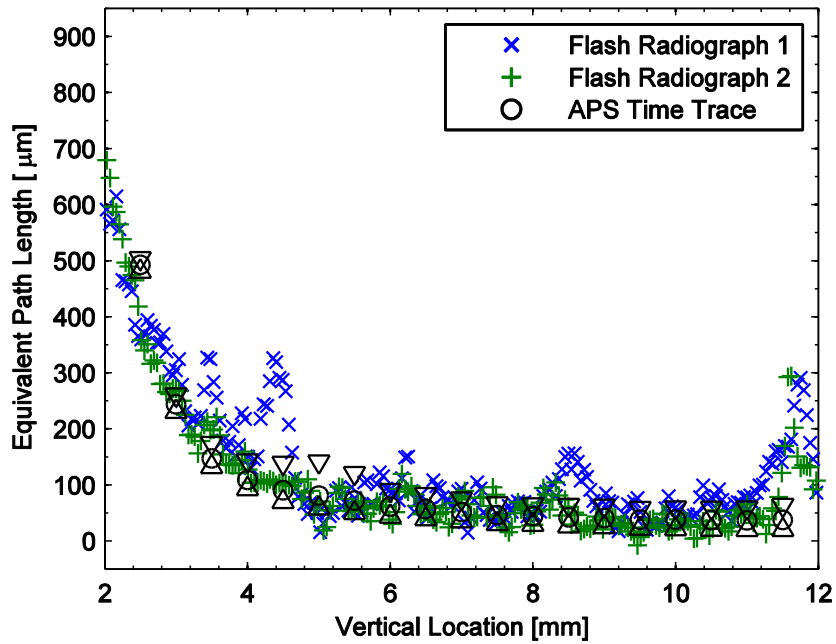


Figure 3-10. Sample flash x-ray radiographs for jet-exit velocities of 3.5 m/s (a) and 8 m/s (b).

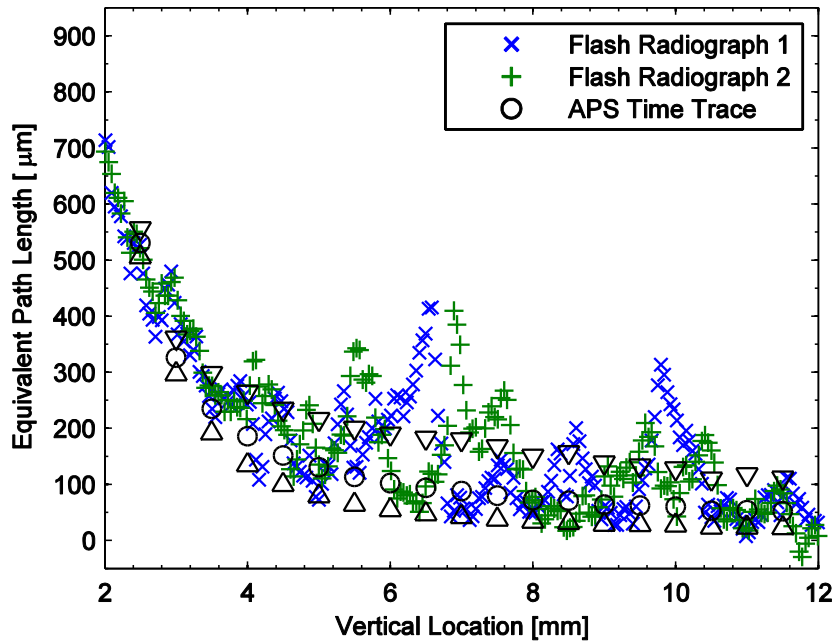
Figure 3-11 compares the centerline vertical profiles from the flash x-ray images with vertical spatial scans obtained using the APS x-ray source. Of course, the flash x-ray images are instantaneous while the APS data are time-averaged based on point-wise raster scanning. Although the spatial profiles from the flash x-ray data reflect the variations in EPL that occur because of the impact waves generated by the merging of liquid jets, the spatial trends are

very well matched with the time-averaged trend from the APS data. For example, the EPL decays much more quickly along the centerline for the case of 3.5 m/s as compared with that of 8 m/s. This is because much of the liquid in the case of 3.5 m/s is contained within the outer rim structure of the sheet. In contrast, the rim structure at 8 m/s is non-existent and most of the liquid is contained within the central, very turbulent region. Based on the very thin liquid sheet for the case of 3.5 m/s in the 10–12 mm region, as shown in Figure 3-11(a), it is possible ascertain that the flash x-ray radiographs can capture sheet liquid features with EPL down to about 50 microns.

The flash x-ray spatial profiles are also able to quantify the variations in EPL with high signal-to-noise ratio, even though these variations may appear to be quite subtle in the images shown previously in Figure 3-10. This is particularly evident at the ~8.5 mm location for the case of 3.5 m/s, where the line profile shows the sheet thickness to vary by about 100 μm . However, fluctuations in EPL for the case of 3.5 m/s occur primarily further upstream near the jet impingement region and further downstream where the sheet coalesces. This is in contrast to the case of 8 m/s, in which the largest fluctuations occur in the central part of the sheet from 4–12 mm, as shown in the images of Figure 3-10(b) and the spatial profiles of Figure 3-11(b). The larger fluctuations in sheet thickness for the case of 8 m/s are also evident in the larger variance of the APS data in Figure 3-11(b).



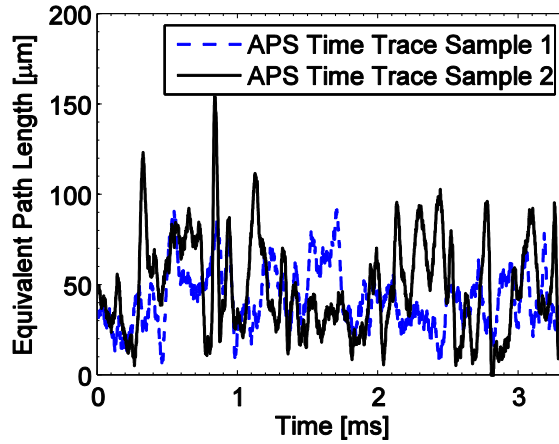
(a)



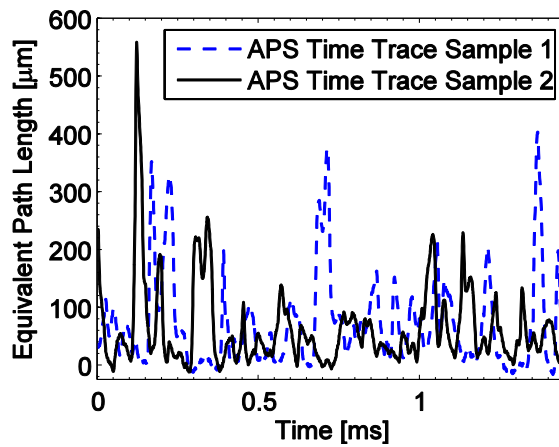
(b)

Figure 3-11. EPL of the centerline comparing data from flash and APS x-ray data for jet-exit velocities of 3.5 m/s (a) and 8 m/s (b). The triangles in the APS data bound the variance.

To compare the fluctuations of the EPL in time, Figure 3-12 shows sample time traces of the APS data at the 3.5 m/s (Figure 3-9a) and 8 m/s (Figure 3-9b) conditions. Note that the time traces in Figure 3-12 are samples of the much longer signal traces that are used later in the spectral analysis. The durations of the time traces in Figure 3-12 are 3.3 ms and 1.45 ms, respectively, which were selected to correspond to an approximate convective length of about 10 mm based on the vertical component of the jet-exit velocities (Dombrowski & Hooper, 1964). As it happens, 10 mm also corresponds to the approximate length of the contiguous liquid sheets shown previously in the flash x-ray images. This region of contiguous liquid sheets begins at approximately 2 mm downstream and ends at approximately 12 mm downstream, as marked on the plots in Figure 3-10. Hence the spatial characteristics in the flash x-ray images and the APS time traces should have similar characteristics based on Taylor's hypothesis. Of course, the spatial frequencies from 2 mm to 12 mm downstream are varying in space, and this cannot be captured by the time traces as they are collected at a fixed location 8 mm downstream. However, it is possible to discern based on Taylor's Hypothesis and the spatial profiles close to 8 mm in Figure 3-11 that the EPL time traces for the case of 3.5 m/s should vary by about 50–100 μm and the EPL time traces for the case of 8 m/s should vary by 150–350 μm . This is well reflected in the time traces shown in Figure 3-12, although the spatial extent and magnitude of the fluctuations in EPL from the flash radiographs do not agree with the APS data due to spatial blur in the images. This blur results in wider fluctuations and lower than expected EPL values within the liquid sheet.



(a)



(b)

Figure 3-12. Sample APS time traces 8 mm below the injector exit for jet-exit velocities of 3.5 m/s (a) and 8 m/s (b).

Because of the periodic nature of the fluctuations in EPL generated by the jet impact process, it is of interest to evaluate the frequency content of the time traces from the APL data along with the spatial frequencies from the flash x-ray images. The centerline data from five radiographs of the full spray are analyzed, and the impact wave amplitudes and frequency information are shown in Figure 3-13. The range of resolvable frequencies is

determined by the Nyquist criterion and the length of the signal. The centerline data arrays have a 44 μm pixel size, giving a Nyquist frequency of 11.3 mm^{-1} and 10 mm lengths with a minimum resolvable frequency of 0.1 mm^{-1} . This gives a dynamic range of 110 for the flash x-ray data. The higher frequency behavior seen in the back lit images is not able to be resolved, while the lowest resolvable frequencies are sufficient because the spray is a finite length.

A similar frequency analysis was applied to the data averaging the five spatial PSDs computed using a Hann window and are compared in Figure 3-13. The spectra for the case of 3.5 m/s compare well, as shown in Figure 3-13 (a), given the limited amount of spatial data. The low frequency components are likely perturbed by limitations on signal lengths. However, there is consistent behavior in the region around 2 mm^{-1} and 5 kHz, providing credence to the measurement technique and analysis. The high frequency component tapers off around 4 mm^{-1} and 12 kHz. The high frequencies found in the radiographs are believed to be caused by noise in the measurement.

The same EPL and spectral analyses were performed for the case of 8 m/s, as shown in Figure 3-13 (b). The spectra become more difficult to compare in this condition. There is agreement in the peak frequency agreement around 1 inverse mm and 6 kHz, but the trend at higher frequencies is not as well overlapped as with the low velocity condition. In addition, the spectrum from the APS data is surprisingly broad. This indicates that the fluctuations in EPL are not purely periodic and have a wide variation in frequency. This may result from the larger sample size used for the APS data, whereas the data from the flash x-ray images may show characteristics that are specific to the limited data set.

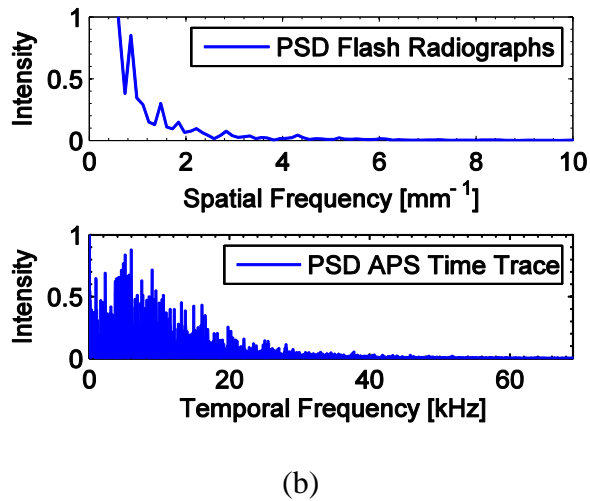
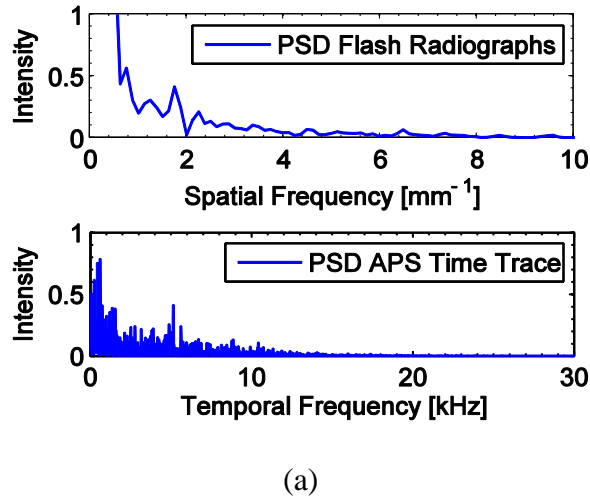


Figure 3-13. Plots comparing the EPL spectral content caused by waves in the liquid sheet for jet-exit velocities of 3.5 m/s (a) and 8 m/s (b).

Table 3-2 compares the imaging method capabilities of the x-ray sources. The APS images are of higher contrast, spatial resolution, and accuracy. Despite their lower fidelity, the flash images are capable of quantitative time-resolved 2-D imaging. Differences in spatial resolution in the flash x-ray technique are due to the geometry of the source, spray, and detector. Upstream of the jet impingement point, the flash radiographs do not capture the exact shape of the jets due to the limited spatial resolution of the flash x-ray images. The

impact waves have been captured, but their peak thicknesses are reduced because of image blur. The spatial resolution in the image plane was estimated to be ~350 μm at a 10-90% rise criterion for the flash x-ray images, which is sufficient to capture the instability waves, the ligands tearing from the sheet, and the larger spray droplets. The spatial resolution is less of a factor farther downstream, and the two measurements capture the impact waves as seen by magnitudes of the fluctuations in EPL.

Table 3-2. Comparison of measurement results from the APS and the flash tube source.

Source	APS Synchrotron	Flash Tube Source
Imaging Method	Raster Scan of Water	Radiograph of 15% KI
Attenuation Coefficient [cm^{-1}]	5.33	$7.32 \times \tau$
Theoretical Penumbra [μm]	0	125
10-90% Rise [μm]	40	350
EPL Standard Deviation [μm]	0.3	25
Dynamic Range of PSD	12500	110

High Speed Tube Source Radiography

To account for the preferential attenuation of low energy x-rays, a modified version of Beer's Law is incorporated. Equation 3-4 relates the ratio of the measured intensity, I , to the source intensity, I_0 , to the attenuation coefficient, α , and the convolution of the detector response function, ψ . This accounts for the material properties of the attenuating medium, the path length of the medium, and the detector response function.

$$\frac{I(y,z)}{I_0(y,z)} = \frac{\int e^{-\int \alpha(h\nu,x,y,z)dx} \psi(h\nu) dh\nu}{\int \psi(h\nu) dh\nu} \quad (3-4)$$

$$\frac{I(x,y)}{I_0(x,y)} = e^{-\left[m\left(\frac{I(x,y)}{I_0(x,y)}\right)+b\right]EPL(x,y)} \quad (3-5)$$

The modified version of Beer's Law, as shown in Equation 3-5, accounts for these factors using a calibrated attenuation coefficient. This is used to compute an equivalent path length that quantifies the path of the liquid traversed by the x-rays. The linear fit parameters in the attenuation coefficient are found through the calibration of five liquid jets of varying path length between 590 and 2020 μm . With prior knowledge of the path length and measured transmission levels the attenuation coefficient is determined at each path length and a linear function is fit and then used for measurements of EPL, shown in Figure 3-14. The error in the empirical coefficients is approximately 1%, the scatter in data plotted is likely due to the fluctuation of the source during imaging.

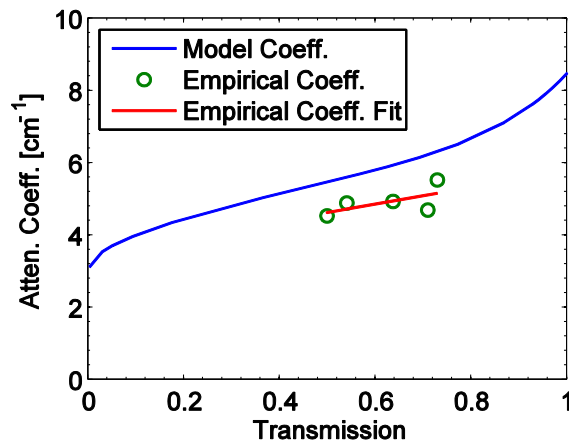


Figure 3-14. Comparison of the empirical and modeled attenuation coefficients vs. transmission for 50% KI. Linear trend lines are used for the attenuation coefficient in Equation 3-5.

The radiographs, therefore, provide a measure of the attenuation of the x-ray radiation which can be used to compute the liquid path length, while backlit optical images capture the refraction and scatter of the visible radiation. These complementary techniques allow the

measurement of fluid geometry and thickness, while the thickness measurement from x-ray radiography is independent of the local geometry.

The radiographs provide a quantitative 2-D map of the sprays thickness with a signal-to-noise ratio (SNR) of approximately 20, in the thicker regions of the spray. The x-ray images have a spatial resolution of 800 μm (10-90% edge rise), and a pixel size of 30 μm . The temporal resolution is limited by the camera exposure time of 48 μs due to image smearing in the direction of movement. Variations in thickness that are difficult to determine quantitatively with visible light imaging are clearly visible and can be tracked through the spray breakup. Resolved edges, small features, and subtle changes in the sprays geometry are revealed in the backlit images. Figures 3-15 and 3-16 show impinging jet radiographs and backlit images at jet velocities of 1.8 m/s and 3.2 m/s, respectively. The data are collected at 20 kHz and every fifth frame is shown.

As shown in Figure 3-15, the jets meet near the top of the images and the liquid spreads into a quasi-stable sheet with a pronounced rim. Impact waves form within the liquid sheets emanating from the impingement point. Instabilities are present in both the sheet and rim. Eventually the sheet collapses and the spray breaks up into large droplets. Certain features of the spray refract the visible light, causing the light to focus internally at some locations, leading to a dark edge and high-intensity (bright) center. In contrast, these same features appear as regions of low intensity in the radiographs due to higher x-ray attenuation. The images are well correlated with what one might expect when only viewing a backlit image of this spray. Certain features including impact waves and sections of the rim are apparent in both images; however it becomes difficult to quantify changes in the liquid path length if only viewing the backlit images due to optical refraction.

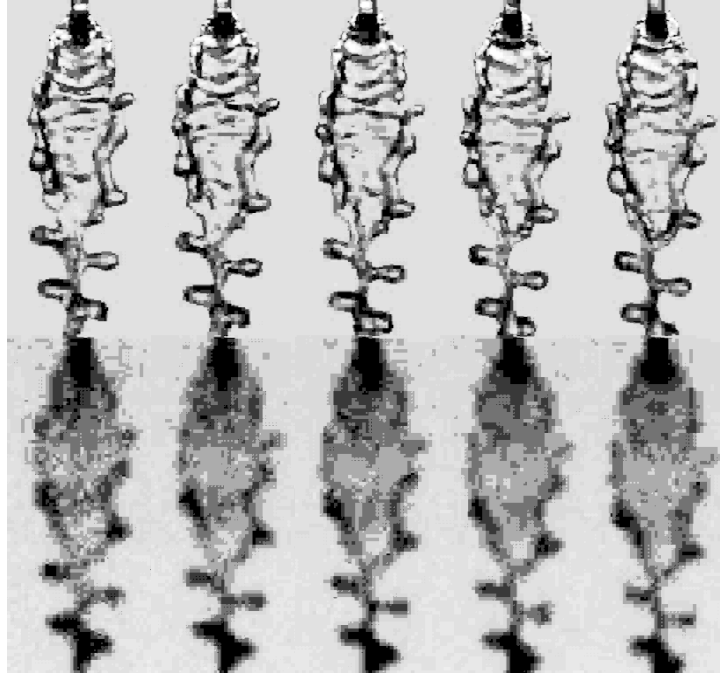


Figure 3-15. High-speed radiograph (bottom row) and backlit image (top row) sequence of the impinging jet spray at 1.8 m/s jet velocity with an exposure of 48 μ s at a frame rate of 20 kHz. Every fifth image is shown.

Figure 3-16 shows a set of impinging jet radiographs and backlit images at a jet velocity of 3.2 m/s with every fifth frame shown. The two jets are no longer stable as they meet near the top of the image. At the impingement point the liquid spreads into a liquid sheet with a greater width relative to the lower velocity condition. As a result, the rim is somewhat less pronounced and contains a lower fraction of the liquid. Impact waves still form on the liquid sheet starting at the impingement point. It becomes clearer that the thickness of the liquid sheet decreases radially from the impingement point. Instabilities, present in both the sheet and rim are more pronounced, leading to ligament and droplet formation. Due to their low EPL and the limited resolution, some of these ligaments and

droplets are detectable but at relatively low SNR. Quantitative measurement of EPL for the smallest features, therefore, requires additional improvement in sensitivity and resolution.

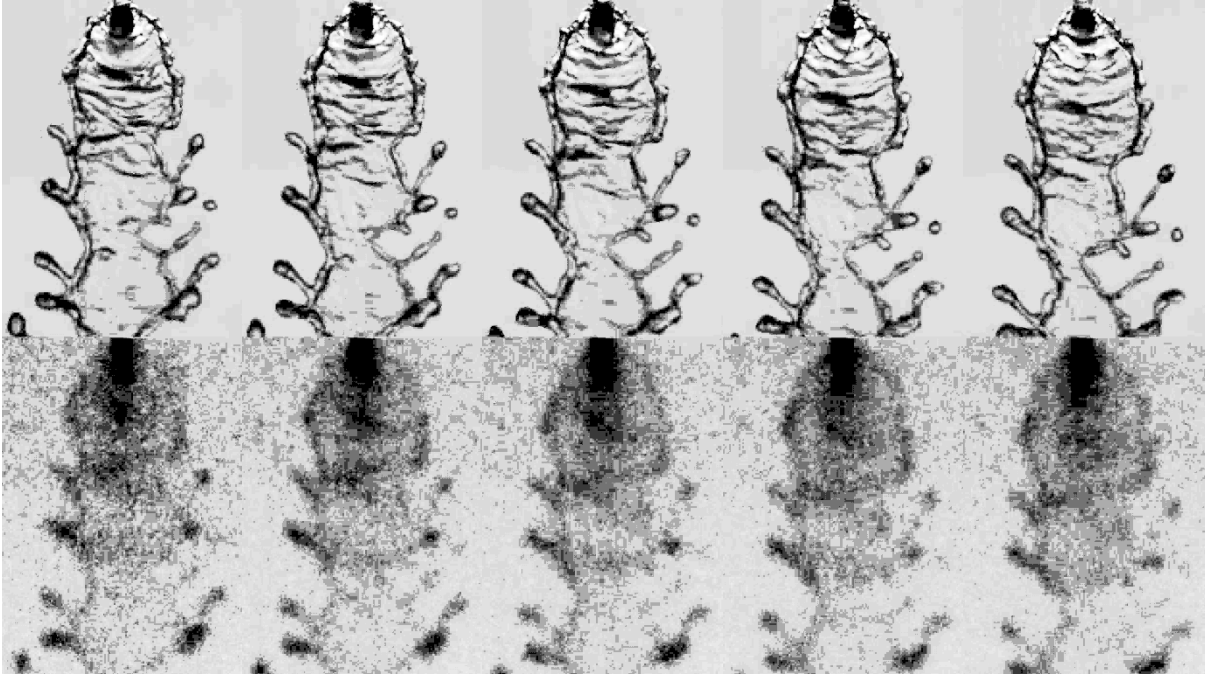


Figure 3-16. High-speed radiograph (bottom row) and backlit image (top row) sequence of the impinging jet spray at 3.2 m/s jet velocity with an exposure of 48 μ s at a frame rate of 20 kHz. Every fifth image is shown.

The simultaneous visible light and x-ray radiography measurements unveil a deeper understanding of the fluid phenomena occurring in an impinging jet spray.

Non-Newtonian Sheet Thickness

The synchrotron source at the APS is ideally suited for mass distribution and sheet thickness measurements within non-Newtonian, shear thinning, viscoelastic sprays. Figure 3-29 shows the change in viscosity with shear rate and the existence of two plateaus, one at the low shear high viscosity limit and the other at the high shear low viscosity limit. It becomes

more important to match previously measured parameters due to the varying viscosity. Reducing the spray to a single Re is no longer applicable. Therefore the addition of contrast enhancing agents greatly alters the behavior of the gel and thus the viscosity as well. The viscosities are described in the section: the global viscosity being a gel with greater loading will exhibit an equal or increased viscosity and a local viscosity where the viscosity of each fluid may change as it flows downstream and the shear rate is reduced. A single geometry was chosen that is common among the literature and current efforts to understand non-Newtonian impinging jets. The injector has an included angle of 60 degrees, a diameter of 508 μm , and a free jet length of 3.5 mm. The non-Newtonian fluid for the study was hydroxypropyl cellulose dissolved in water loaded at 2, 3, and 4% by mass concentration. Water and 84% by mass glycerol in solution with water are included as Newtonian to compare against constant viscosity scenarios. The flow rate was varied from 9.1 to 36.5 m/s to cover most of the common velocities from the literature.

The first velocity investigated was 9.1 m/s where all five fluids were compared. Figure 3-17 shows profiles of the EPL just below the impingement point. The distribution of the fluids here is quite similar. The jets are still apparent and the beginning of the sheet is seen as the shoulders in the profiles around ± 1 mm. As expected the water is spreading the most. The peak values of the HPC reduce with gel loading, following that there is some difference in viscosity but still so similar that they are likely to be near the low viscosity plateau. The glycerol profile is found near the 3% HPC profiles suggesting the local viscosity is similar with the viscosity of the 2% gel being less and the viscosity of the 4% being greater.

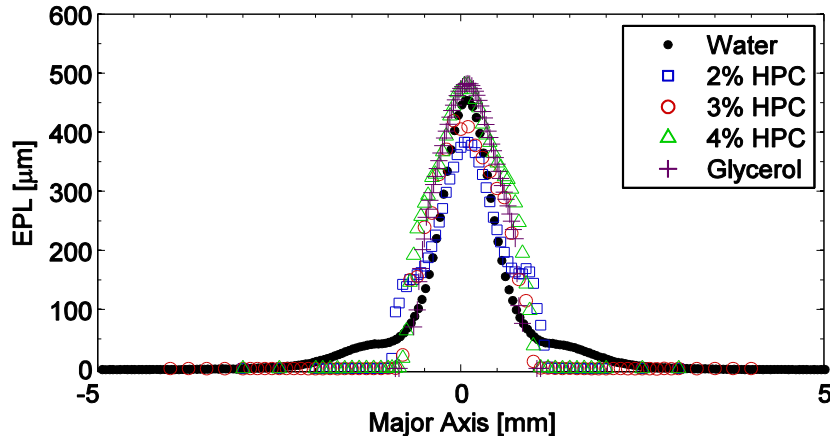


Figure 3-17. Line plot across the spray 0.5 mm below impingement at a velocity of 9.1 m/s.

Moving downstream the profiles no longer overlap, but have split into three separate regimes, Figure 3-18. The furthest spread (lowest viscosity) regime is the water, followed by a rimmed sheet regime comprised of the 2% HPC and glycerol, and the least spread (greatest viscosity) are the 3% and 4% profiles generating narrow and thick sheets. Here the profile difference of the HPC loadings is more prevalent with the 3% and 4% apparently with a local viscosity greater than the glycerol, while the viscosity of the 2% appears to be very close to that of the glycerol.

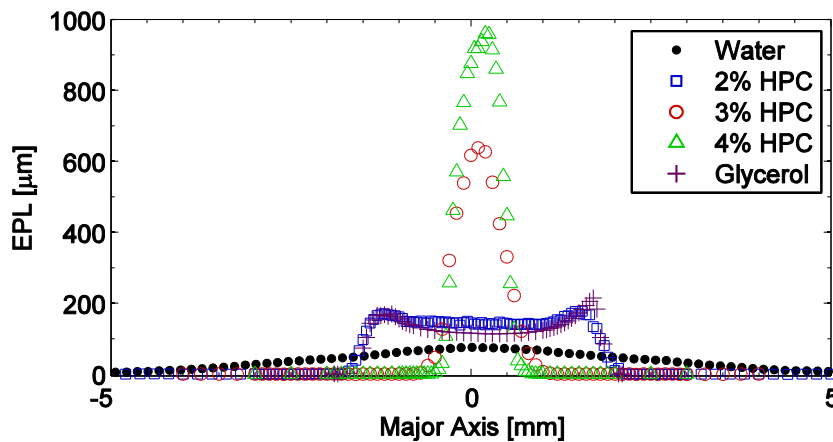


Figure 3-18. Line plot across the spray 6.5 mm below impingement at a velocity of 9.1 m/s.

At 12.5 mm below impingement the profiles have again changed, but the same three regimes are present, Figure 3-19. However the profile of the 2% HPC has narrowed suggesting a further reduction in viscosity and thus local shear rate.

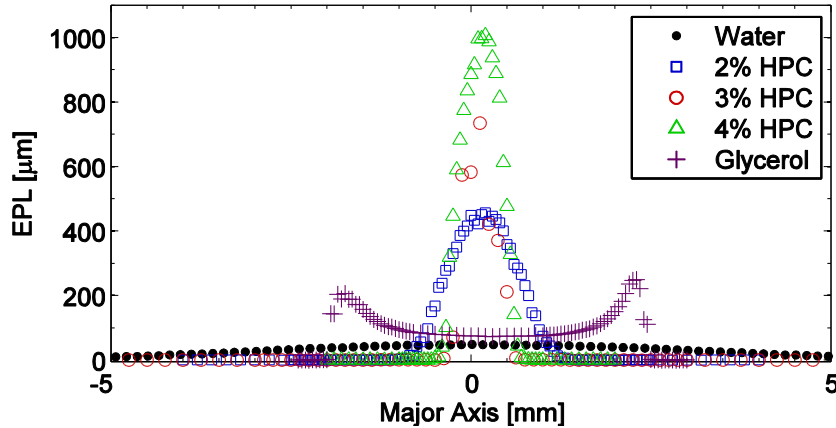


Figure 3-19. Line plot across the spray 12.5 mm below impingement at a velocity of 9.1 m/s.

As the velocity of the jets is increased to 18.2 m/s, just below impingement the profile of the water spray exhibits behavior of a fully developed spray with little to no defined edge to the liquid sheet, Figure 3-20. Only residual wings remain in the water profile. The profiles of the various HPC loadings are even more similar than at 9.1 m/s. The peaks in EPL still follow the gel loading so they are not exactly the same, but the viscosity is likely to be further reduced to a plateau region where shear stress is high enough that the local viscosities of the three gels is similar.

Moving down the sheet to 6.5 mm below impingement the spread of the fluid sheets is following the global viscosity as expected for an impinging jet spray, Figure 3-21. The amount of mass distributed in the rim is seen to increase with a decrease in gel loading, and hence viscosity. This follows previous experiments in which it was found that as Reynolds number is increased the two jets evolve from colliding to forming a sheet with pronounced

rims; then as the Reynolds number is further increased the rim disintegrates and flow is defined as fully developed.

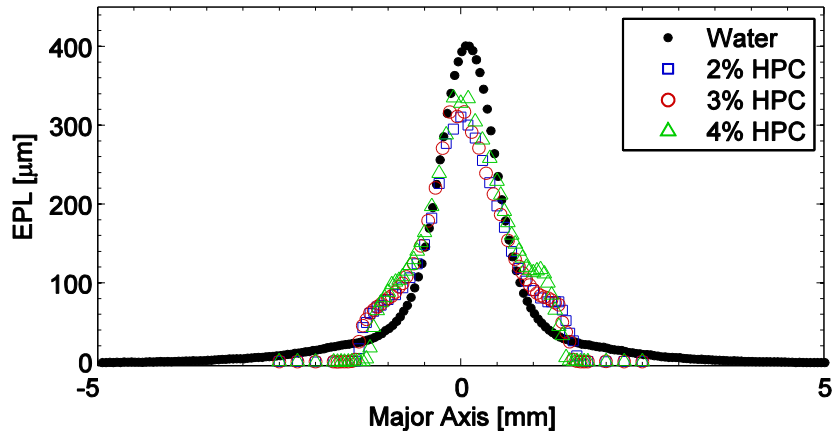


Figure 3-20. Line plot across the spray 0.5 mm below impingement at a velocity of 18.2 m/s.

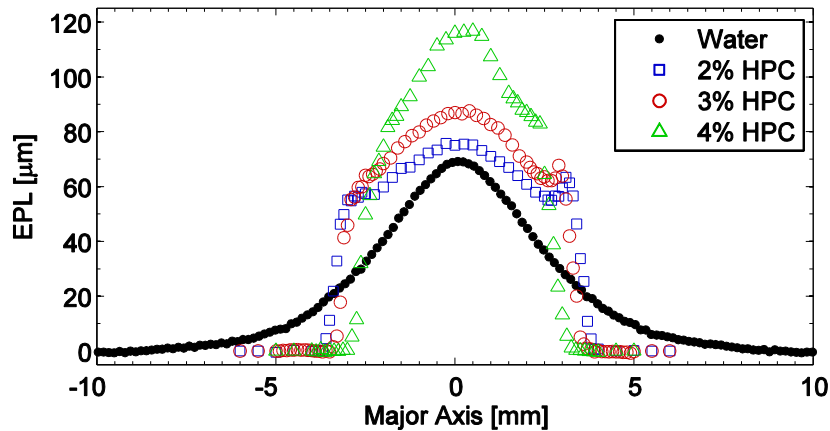


Figure 3-21. Line plot across the spray 6.5 mm below impingement at a velocity of 18.2 m/s.

At the furthest recorded point downstream the trends remain the same, Figure 3-22. The amount of mass distributed in the rim is seen to increase with a decrease in gel loading. This follows previous experiments where when the Re is increased the two jets go from colliding to forming a sheet with pronounced rims, then as the Reynolds number is further increased the rim disintegrates and flow is defined as fully developed.

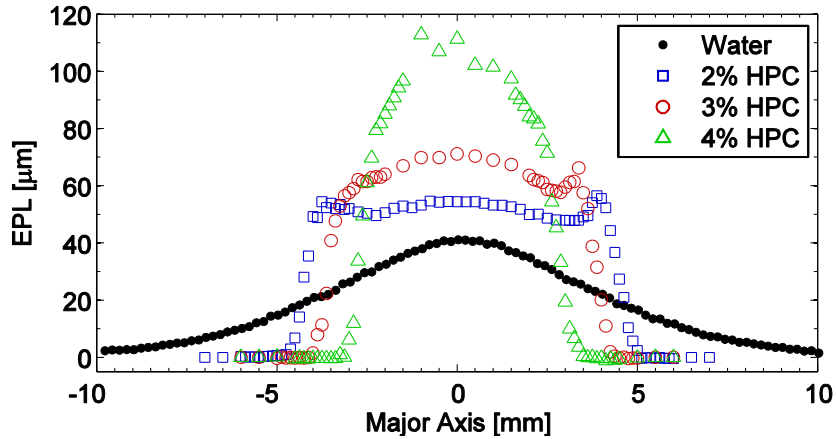


Figure 3-22. Line plot across the spray 12.5 mm below impingement at a velocity of 18.2 m/s.

All five fluids were measured at a velocity of 27.4 m/s, Figure 3-23. At 0.5 mm below impingement the profiles overlap and the largest differences in profile can be seen as the beginning of the fluid sheets are being formed. Here the water has a fully developed profile while all the gel conditions are forming rimmed sheets. The profiles, and by inference the viscosities, of the glycerol and gels appear to be similar near the centerline, and the difference in the gel and glycerol profiles near the edges of the spray may be dominated by the viscoelastic behavior of the gels further from the centerline.

The profiles at 6.5 mm below impingement follow the same trend as in the 18.2 m/s condition, Figure 3-24. However, the 2% HPC profile shows the behavior of a fluid with greater viscosity than the glycerol and nearly matching that of the 3% and 4% gel. Also interesting is that the glycerol and water profiles are nearly identical, which is surprising considering the large difference in viscosity. At this point downstream, if the sheet is fully disintegrated, then viscosity and jet Reynolds number would no longer be the best methods to

characterize the spray. While surface tension might control drop sizes, the overall spreading rate for the water and glycerol profiles is most likely dictated by local turbulent dispersion.

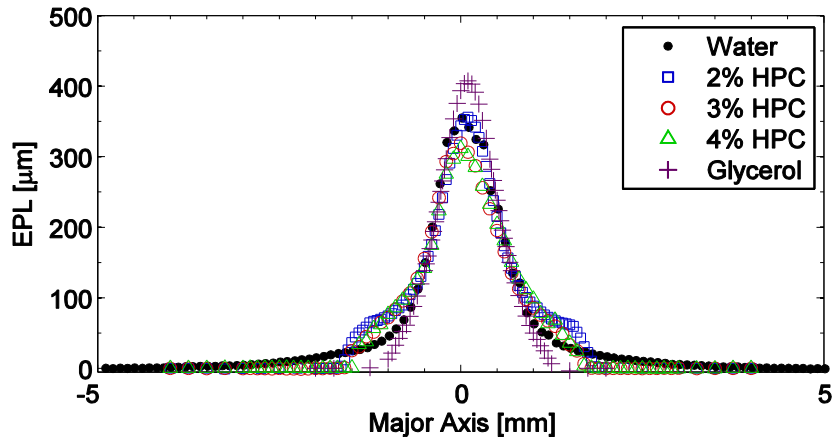


Figure 3-23. Line plot across the spray 0.5 mm below impingement at a velocity of 27.4 m/s.

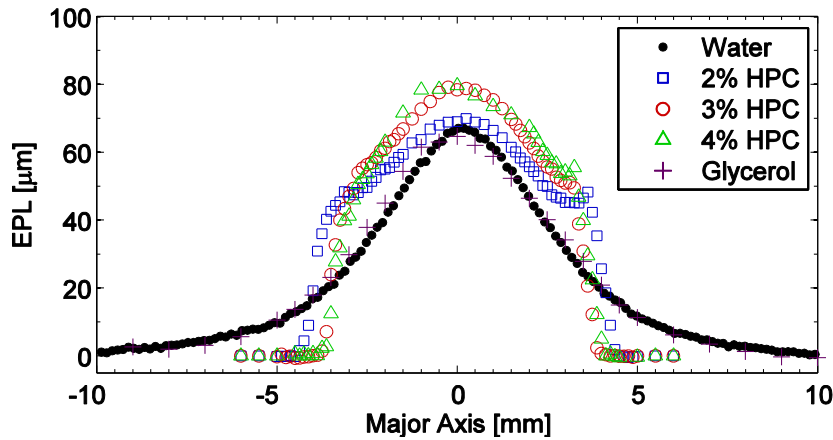


Figure 3-24. Line plot across the spray 6.5 mm below impingement at a velocity of 27.4 m/s.

At 12.5 mm below impingement the profiles follow their expected behavior, with the gel profiles deviating further from each other as the shear rate drops and the sprays become more sensitive to the local viscosity. Glycerol was not measured at this location, Figure 3-25.

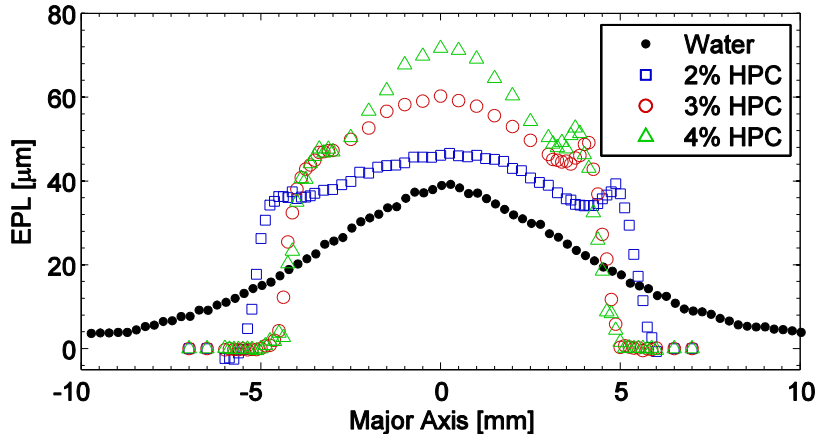


Figure 3-25. Line plot across the spray 12.5 mm below impingement at a velocity of 27.4 m/s.

The high pressure spray system was incapable of spraying the glycerol at 36.5 m/s, but data for water and the gels were collected at these conditions, Figure 3-26. It appears that the local viscosity at 0.5 mm below impingement resides on the plateau of shear rate versus viscosity, with the profiles of all the gel loadings being so similar. Only slight differences in the wings of the profile are visible, which again may be a result of reduced shear in the fluid sheet further from the centerline.

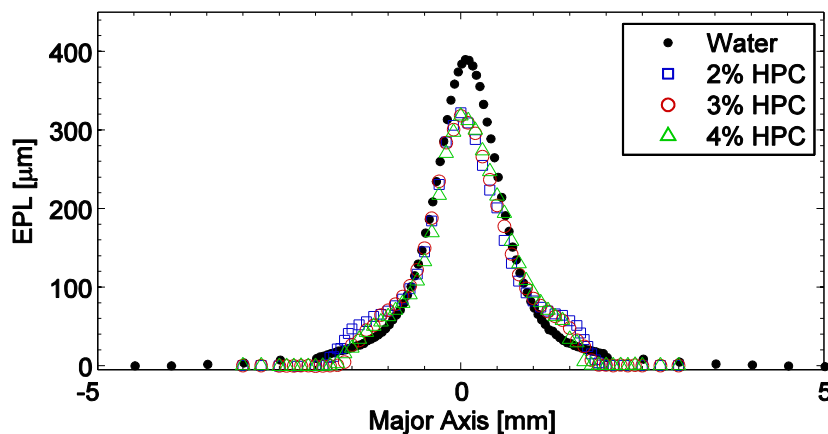


Figure 3-26. Line plot across the spray 0.5 mm below impingement at a velocity of 36.5 m/s.

At 6.5 mm below impingement at 36.5 m/s, the center profiles of the 2% HPC and water are fairly similar, Figure 3-27. It is important to investigate the wings and one may surmise that the water profile represents a droplet field and the 2% HPC is a contiguous liquid sheet. All the gel profiles still exhibit indications of a rim structure.

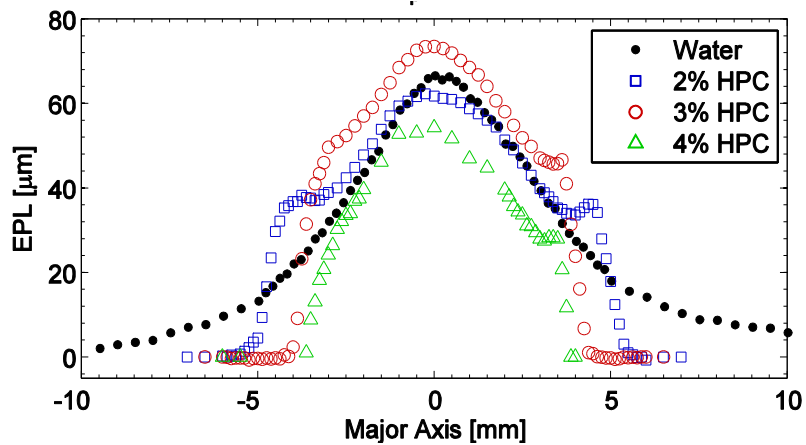


Figure 3-27. Line plot across the spray 6.5 mm below impingement at a velocity of 36.5 m/s.

At 12.5 mm below impingement it is clear that the water and 2% HPC profiles no longer have any similarities, and the behavior is predictable based on the previous velocities and locations presented, Figure 3-28.

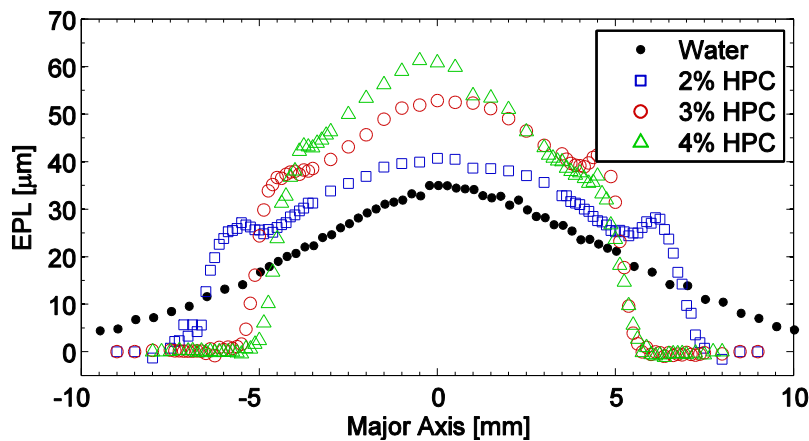


Figure 3-28. Line plot across the spray 12.5 mm below impingement at a velocity of 36.5 m/s.

A graphical representation of the shear rates and viscosities of 3% HPC is shown in Figure 3-29. The local viscosities of the HPC gels are approximated by their profiles in comparison with Newtonian analogues. The figure displays how the viscosity varies in a qualitative sense and the jets impinge and a sheet is formed.

The point wise radiographic measurements of the Newtonian and non-Newtonian sprays show how the behavior of the spray is greatly affected not only by the bulk viscosity but also by the local viscosity. Approximations have been made to determine the change in the gels viscosity as it evolves from jets to forming a liquid sheet.

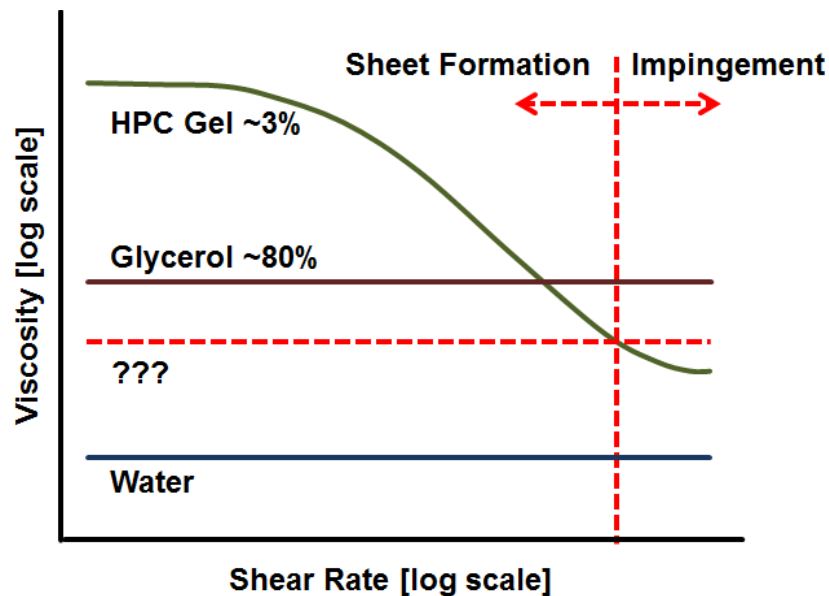


Figure 3-29. Qualitative plot displaying the change in viscosity of the gel as a function of shear rate with spray locations superimposed based on approximated viscosity from spray behavior. The HPC data is taken from Mallory 2012.

Liquid Mixing

The impinging-jet liquid mixing measurements were performed at the Advanced Photon Source at Argonne National Laboratory by collecting the x-ray spectrum with a

silicon drift diode (SDD) and measuring attenuation with a PIN diode. The attenuation measurements are used to calibrate the fluorescence signals, which are converted into EPLs after a series of corrections.

Fluorescence Reabsorption Correction Methods

Figure 3-30 shows the raster-scan profiles of the two separate (unmixed) jets 1.5 mm upstream of the impingement point. Hence, this location is defined here as $z = -1.5$ mm with the origin near the center of the impingement point. At this z location, the jets have not yet begun to merge and have FWHM profiles of ~ 520 μm , as expected. Because the initial jets can be easily isolated and should be nearly identical as they approach the impingement location, this is an ideal location to evaluate the accuracy of the signal corrections applied for the fluorescence measurements. During and after jet impingement, which is of primary interest in this work, the error due to the reabsorption correction is expected to decrease significantly due to thinning of the liquid sheet in the minor axis. After correction, the symmetry of the jet profiles improves significantly, and the EPL of each jet from the corrected fluorescence measurements closely matches that measured directly with x-ray attenuation. However, a slight shift (<35 μm) is apparent in the profile of the copper-seeded jet because of the higher levels of correction for reabsorption. The error in the fluorescence measurement was calculated at each scan point, taken as the absolute difference of the sum of the fluorescence EPLs relative to the EPL determined from attenuation. This leads to maximum local relative error of 4% in the EPL values reported for the pure copper-seeded jet using the stereo method and 5% using the four-salt method. While the error from the four-salt method is slightly higher, it has the important benefit of being applied on a shot-to-shot basis.

This is important for time-resolved measurements. The stereo method requires the spray to be rotated and is only applicable for time-averaged measurements. The error with the stereo method may result from overcorrection of fluorescence reabsorption due to the SDD not being exactly perpendicular to the excitation beam. The main source of error with the four-salt method is separating the fluorescence lines from the different elements, particularly subtracting the K_{β} line from an element from the K_{α} line from the element of next higher atomic number. An additional bias error in the attenuation and fluorescence signals appears in the data as intensity spikes (e.g., near $x = 0$ in Figure 3-30). These are most likely because of droplets collecting on the injector face and falling through the x-ray beam. These transient errors are infrequent and do not appreciably affect the overall jet profiles and observations about the mixing process.

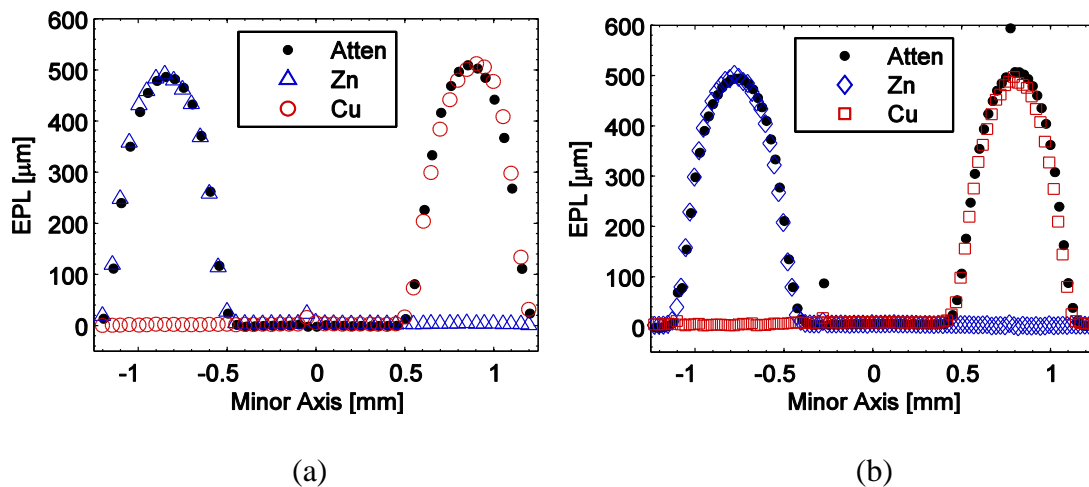


Figure 3-30. Line plots of the EPL across spray at $z = -1.5$ mm upstream of impingement with the stereo (a) and four-salt (b) correction methods compared with attenuation.

Mass distributions of each jet during the start of the mixing process are shown in Figure 3-31 with both types of correction methods. The liquid jets are spaced slightly closer

together in the four-salt data at $z = -0.5$ mm just upstream of the impingement point such that the point of impingement is slightly higher for the four-salt data. This is noticeable in Figure 3-31, where the liquid jets have deformed near the center of the impingement point in the four-salt data, leading to a higher peak in EPL at $x = 0$ mm. This indicates the beginning of sheet formation. In addition, it is possible to detect long tails in the EPL profiles that reach nearly to the other side of the opposing jet. This is somewhat surprising as one might expect the jets to compress at the impingement location. Rather, these tails in the EPL profiles give an early indication that some fraction of each fluid is beginning to penetrate across the opposing jet. Nonetheless, as the two jets begin to merge, they largely maintain their round spatial profiles. This is evident because their FWHM values ($540 \mu\text{m}$) in the minor axis nearly match their EPL values, which represent the jet widths in the major axis along the path of the x-ray beam. Hence, there is a jet core that maintains its structure early on.

Further downstream, the liquid sheet begins to spread into the y - z plane. As this plane is along the path of the x-ray beam, the peak EPL increases significantly as shown in Figure 3-32, where the peak EPL at $x = 0$ (where the two jets meet) has increased to $\sim 1200 \mu\text{m}$. At this downstream location, the total width of the merging jets has compressed to a combined FWHM of only $\sim 380 \mu\text{m}$, which is narrower than the initial FWHM of each separate jet.

Just downstream of the impingement zone, it is possible to see a sudden and significant narrowing of the jet in the minor axis and a spreading of the liquid sheet in the major axis. The visible images also show the appearance of ligaments and discontinuities in the liquid structure, indicating that the merging event initiates the liquid breakup process very near the impingement point. Nonetheless, the narrow profile of the combined jets shown in attenuation data of Figure 3-32 implies that a vast majority of the liquid is confined to a very

narrow sheet at this downstream location. Likewise, the *individual* jets are compressed from a FWHM of 450 μm to only 310 μm , as evident in the fluorescence measurements of EPL in Figure 3-32. This compression is accompanied by significant intermingling of the two fluids, likely through transmissive mixing (Ashgriz et al., 2001).

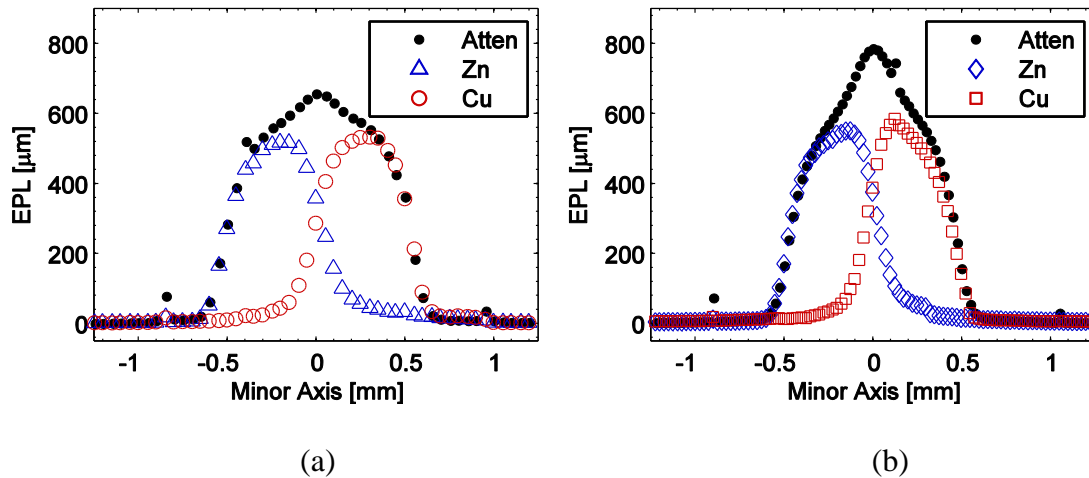


Figure 3-31. Line plots of the EPL across spray at $z = -0.5$ mm upstream of impingement with the stereo (a) and four-salt (b) correction methods compared with attenuation.

At 2 mm below impingement point, the sheet distribution thickens as transmitting mixing and breakup continues, Figure 3-33. Above this location a majority of each fluid has crossed to the opposite side of each jet. The location at which each fluid is exactly overlapping can be estimated between 0.5 mm and 2 mm below the impingement point. The inversion of the jet positions is still apparent well downstream of the impingement point at $z = 9.5$ mm, as shown in Figure 3-34, although by this point the jet profiles widen due to turbulent dispersion and slowly merge back together. Indeed, the backlit images show that this location is beyond the breakup length of the spray where the liquid is primarily contained within ligaments and droplets formed through instabilities in the liquid sheet.

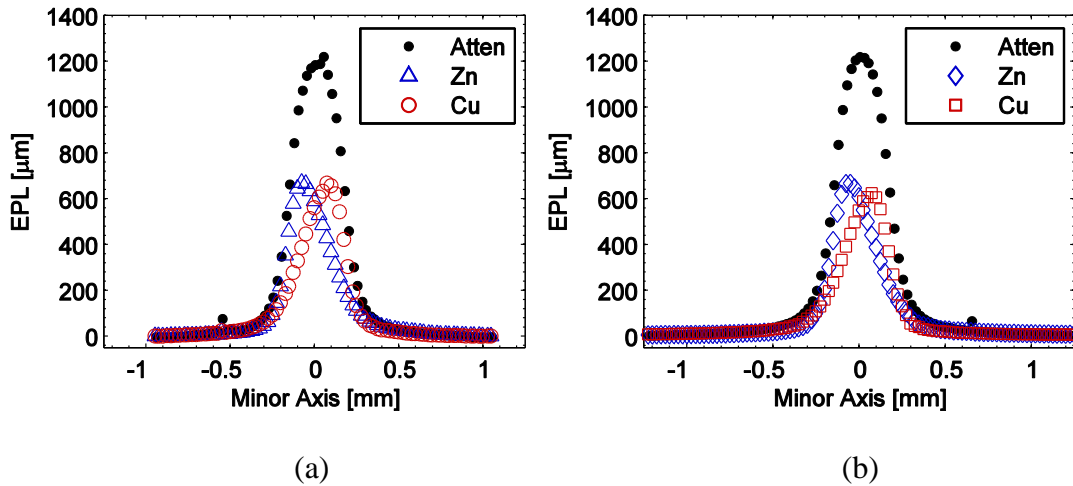


Figure 3-32. Line plots of the EPL across spray at $z = 0.5$ mm downstream of impingement with the stereo (a) and four-salt (b) correction methods compared with attenuation.

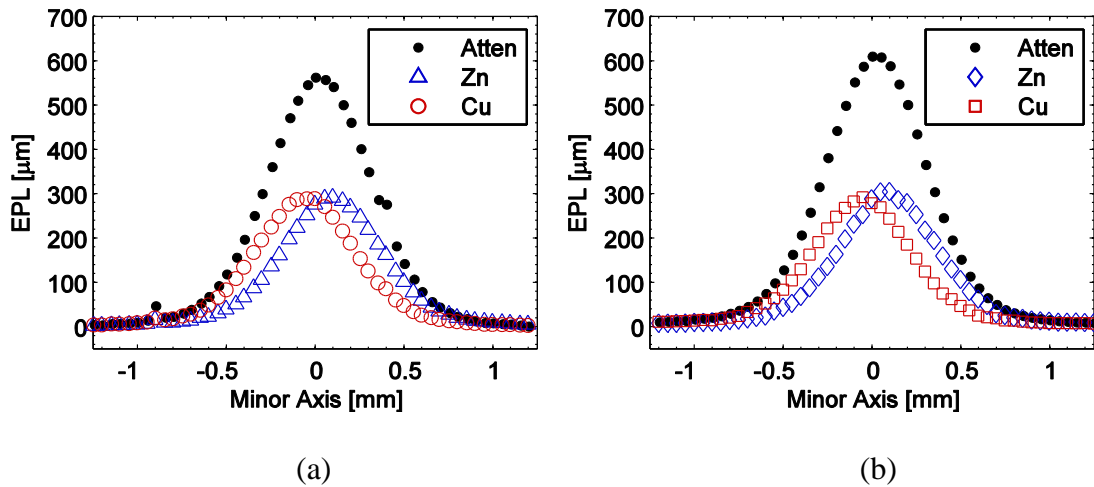


Figure 3-33. Line plots of the EPL across spray at $z = 2$ mm downstream of impingement with the stereo (a) and four-salt (b) correction methods compared with attenuation.

Information about the accuracy of the measurements presented in Figures 3-30 through 3-34 is listed in Table 3-3. The error is taken as the absolute difference between the attenuation signal and the sum of the fluorescence signals from the two fluids. All errors

reported are averaged from data where the total EPL was greater than 100 μm and presented for each vertical location. According to Table 3-3, the stereo method is fairly effective and has the advantage of simpler spectral analysis. However, this requires additional radiographic data orthogonal to the x-ray beam path to apply the correction. The four-salt method does not require any additional data but care must be taken when choosing

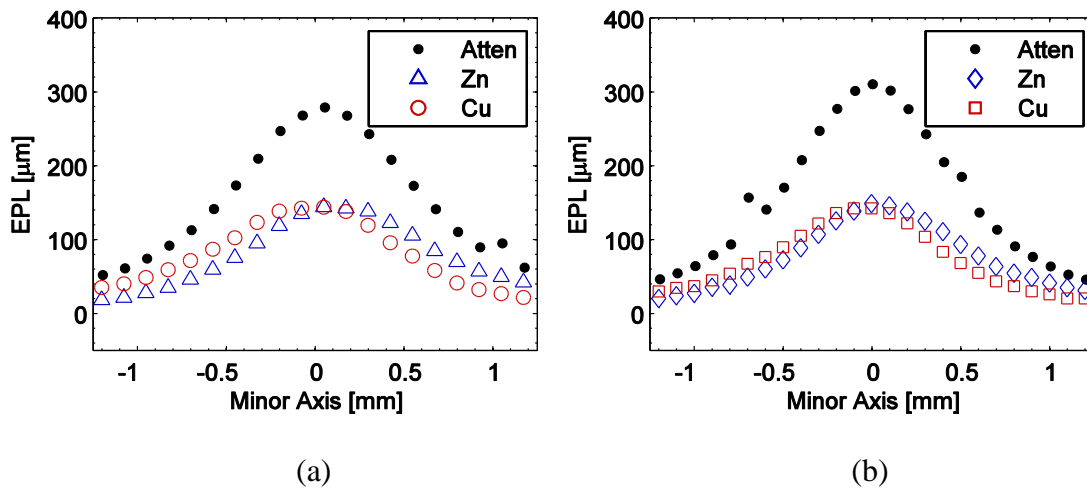


Figure 3-34. Line plots of the EPL across spray at $z = 9.5$ mm downstream of impingement with the stereo (a) and four-salt (b) correction methods compared with attenuation tracers and when analyzing the data, particularly where spectral features overlap.

In addition to the jet profiles presented in Figures 3-30 through 3-34, additional fluorescence measurements from the two fluid streams were collected at various downstream locations, as presented in Figure 3-35. These measurements quantify the transmissive mixing process in the near field that has previously has been inferred from measurements well downstream of the impingement zone (Rupe, 1953 and Ashgriz et al., 2001). Results presented by Ashgriz et al. (2001) describe this process using a very similar injector setup, wherein transmissive mixing behavior was observed at a slightly lower velocity of 16.5 m/s

(compared to 18.3 m/s here) further downstream at 27 mm. The downstream mass distribution was measured via a patternator placed within the droplet field below the injector. Figure 3-35(d) shows a reconstructed mass-distribution image from the current work generated using the EPL of each liquid across the measurement region at various downstream locations. Included in Figure 3-35 is a schematic of the atomization modes inferred from the experiments of Ashgriz et al. (2001), with the current data showing the quantitative spatial distribution of the two fluids within the impingement zone.

Table 3-3. Measurement error of fluorescence signals

Vertical Location [mm]	Stereo Method		Four-Salt Method	
	Error [μm]	Error [%]	Error [μm]	Error [%]
-1.5	14.5	4.5	15.9	4.3
-0.5	21.5	5.4	21.6	4.5
0.5	24.7	4.9	32.3	4
2	4.1	1.4	22.7	5.3
9.5	6.4	3	17.2	8.1
Average	14.2	3.9	21.9	5.2

Of particular interest in this work is the time scale required for transmissive mixing in the near field, as this has implications for the physicochemical modeling of reactive (e.g., hypergolic) impinging jets. Based on the data presented thus far in this work, it is possible to determine that the location required to reach significant overlap in the mass distributions of the two jets occurs between $z = 0.5$ mm and $z = 2$ mm downstream of the impingement point, with complete overlap occurring by about $z = 1.25$ mm. As the jet velocity is 18.3 m/s with a vertical component of ~ 15.8 m/s, one can estimate that the time scale for transmissive mixing is in the range between 55–110 μs , where 110 μs is the time required to ensure nearly

complete overlap of the mass distributions. This can be used to determine if the time scales required for gas formation, ignition, and chemical reactions are of a similar order and whether physicochemical models of reactive jets should include two-way coupling with the mixing process.

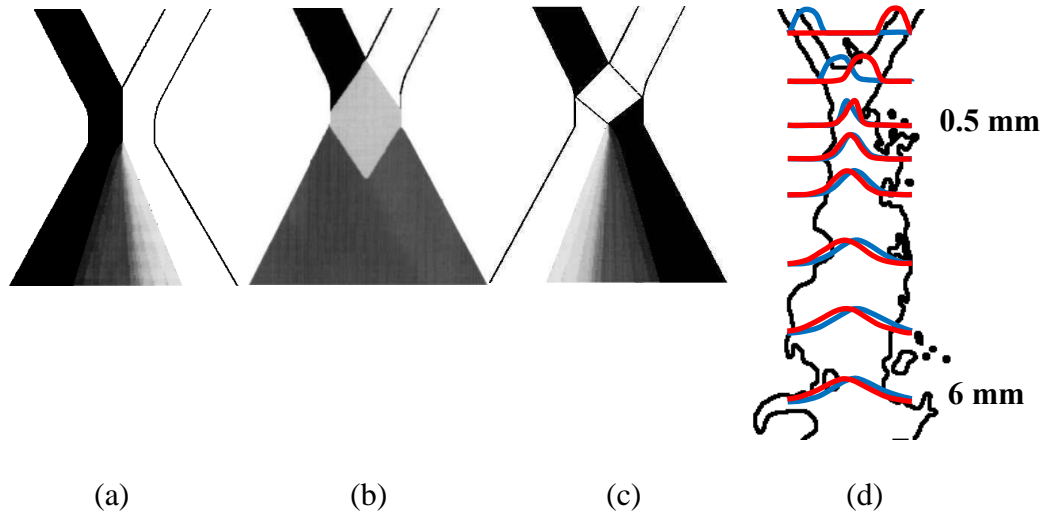


Figure 3-35. Schematic diagrams of (a) reflective, (b) well mixed, and (c) transmissive interaction modes (Ashgriz et al., 2001) compared with (d) x-ray fluorescence measurements of each fluid tracked through the impingement zone.

These measurements are of interest to the spray community to understand mixing phenomena at the location of mixing. These methods have been applied to both non-Newtonian and Newtonian sprays, and different mixing characteristics are discussed further below.

Gel Mixing Study

Previous mixing studies of impinging jets have been limited to sprays that have fully atomized. The x-ray fluorescence technique is not limited by the presence of large liquid

structures or dense droplet fields. Because of this, it is particularly suited to non-Newtonian gel sprays. The mixing of gels is of particular interest because mixing has been shown to be dependent on the local Reynolds number, which can significantly complicate efforts at predicting spray behavior. Since the viscosity is dependent on the shear rate, a fixed Reynolds number is no longer sufficient to define all of the mixing phenomena for a given spray. To investigate the mixing behavior of non-Newtonian viscoelastic gels, a range of gel loadings (1, 2, and 3 % by mass HPC) were employed at velocities of 18.3 m/s and 36.5 m/s. A glycerol water solution was used as a high viscosity Newtonian analogue. Since the gel sprays do not undergo full breakup at these conditions the locations where measurements are conducted is limited to just before impingement and a few millimeters below impingement. After this point the gel is a contiguous sheet flapping back and forth, in and out of the measurement volume, so an accurate mixing measurement is difficult to realize.

Measurements made of 92% by mass glycerol in solution with water are shown in Figure 3-36. The three locations show where the two jets begin to merge ($z = -0.5$ mm) as well as where they compress upon impact and begin to spread in the plane perpendicular to the page (see increase in EPL at $z = 0.5$ mm and 2.5 mm). These phenomena are present in all of the investigated conditions. There is little mixing in the case of glycerol, only a small amount occurs near the horizontal centerline. The profile 2.5 mm below impingement becomes a little askew. The reasons for this are unknown. The mixing is still believed to be qualitatively accurate based on the two measurements made at -0.5 mm and 0.5 mm.

Figure 3-37 shows the EPL profiles for the gel with 1% HPC, manifesting the same basic phenomena, with some subtle differences. Just above the point of impingement at $z = -0.5$ mm, the profiles look almost identical to the glycerol profiles, with roughly the same

amount of mixing. The 1% HPC appears to be mixing better than the glycerol at $z = 0.5$ mm below impingement. This can be attributed to the lower viscosity at high shear rates due to merging. At $z = 2.5$ mm below impingement, the two fluids appear to be very well mixed, although the jets do not cross to the other side as was found with the water sprays. Note that the sheet can move with respect to the measurement volume and so the amount of mixing may be overestimated.

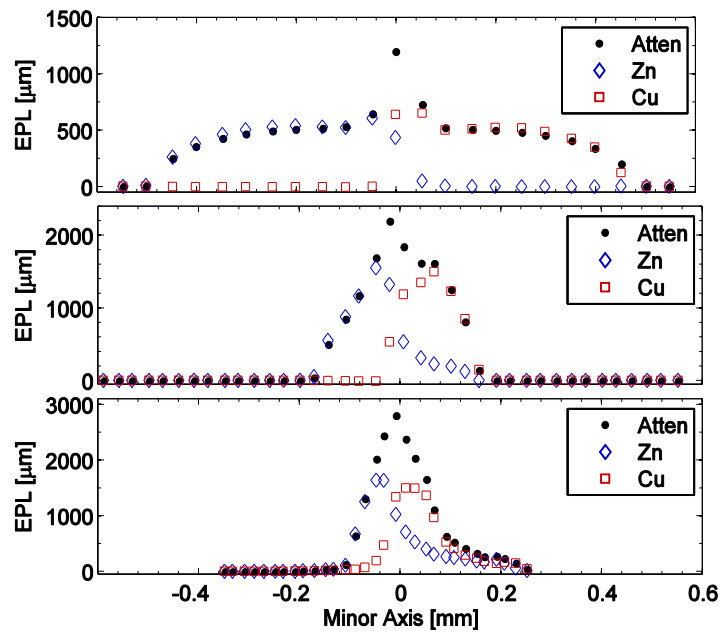


Figure 3-36. 92% Glycerol at a velocity of 18.3 m/s, -0.5 mm above impingement (top), 0.5 mm below impingement (middle), and 2.5 mm below impingement (bottom).

An increase in gel loading to 2% HPC yields the same profile at -0.5 mm as seen with the glycerol and 1% HPC, as shown in Figure 3-38. Both profiles below impingement appear to be broader in the minor axis. The mixing follows almost the same trend as the 1% HPC.

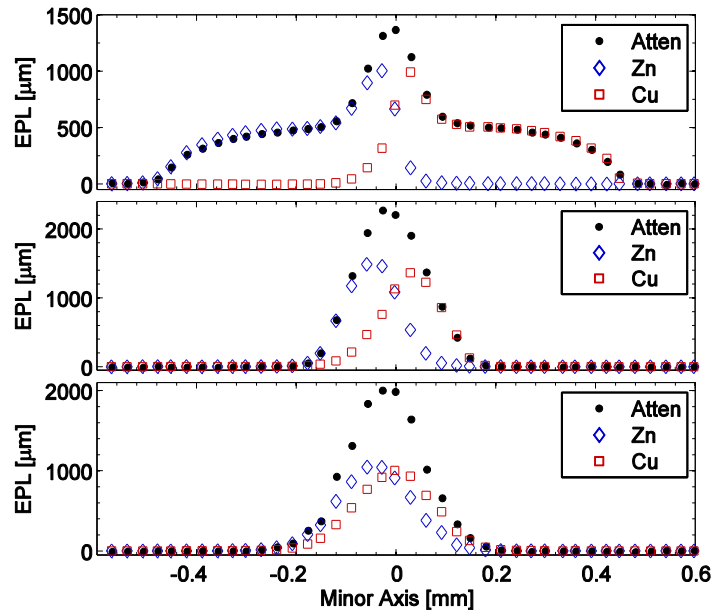


Figure 3-37. 1% HPC at a velocity of 18.3 m/s, -0.5 mm above impingement (top), 0.5 mm below impingement (middle), and 2.5 mm below impingement (bottom).

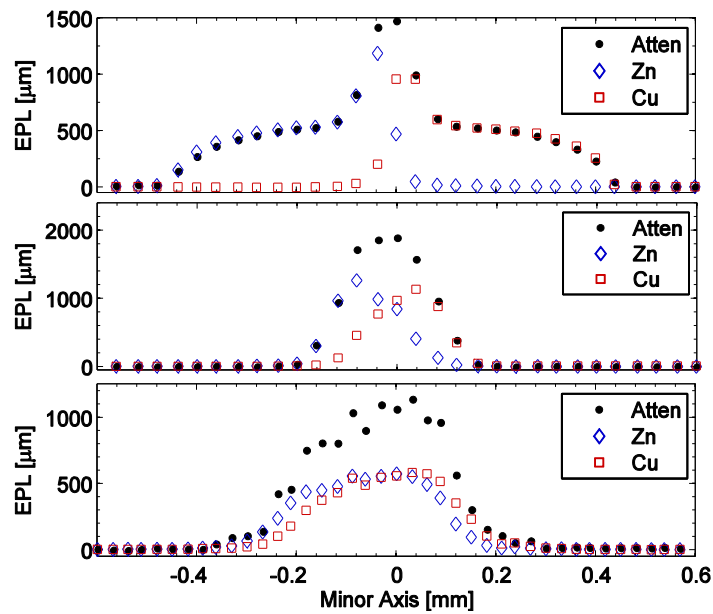


Figure 3-38. 2% HPC at a velocity of 18.3 m/s, -0.5 mm above impingement (top), 0.5 mm below impingement (middle), and 2.5 mm below impingement (bottom).

Further increasing the gel loading to 3% HPC produces the same trend as with the 2% HPC, shown in Figure 3-39. The profile above impingement is still similar, with an exception of the peak EPL along the centerline. Both profiles below impingement show the same level of mixing in a wider sheet. These changes are attributed to the increase in viscosity.

The velocity was doubled to 36.5 m/s, and the profiles show a slight change of shape and little change in mixing. The profiles of 1% and 3% HPC for the case of 36.5 m/s are shown in Figures 3-40 and 3-41, respectively. The differences in the profiles are seen mostly at 2.5 mm below impingement.

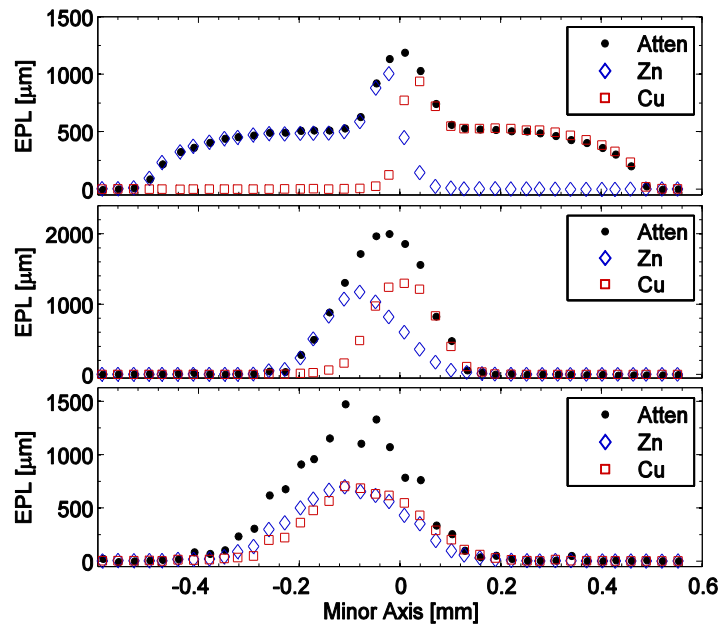


Figure 3-39. 3% HPC at a velocity of 18.3 m/s, -0.5 mm above impingement (top), 0.5 mm below impingement (middle), and 2.5 mm below impingement (bottom).

The changes from 18.3 to 36.5 m/s are minimal for the gel loading of 3%. The profiles and the mixing appear nearly identical, as shown in Figures 3-40 and 3-41. It is surprising to see such little change in EPL profile and mixing even when the gel loading and velocity were varied by a wide margin. The lack of difference in the mixing characteristics of

the gels may be due to equality in viscosity despite the variance in gel loading. If the shear rate is sufficiently high the viscosity reaches a plateau where the local viscosity stops decreasing. In this sense the conditions may be quite similar.

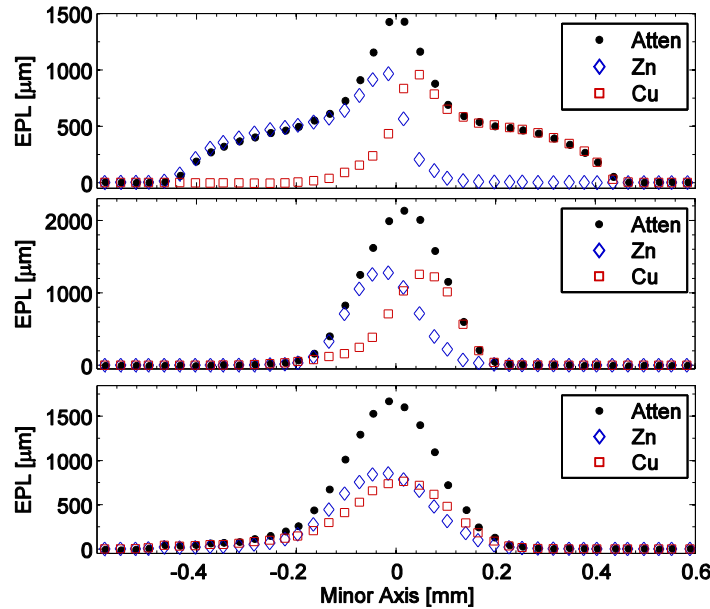


Figure 3-40. 1% HPC at a velocity of 36.5 m/s, -0.5 mm above impingement (top), 0.5 mm below impingement (middle), and 2.5 mm below impingement (bottom).

The gel study was limited by time and was not exhaustive to all the possible conditions for like doublet impingement. The gels take time to mix and load and are not reusable, the time it takes to load the gels is well within the stable lifetime of their viscosity (approx. 2 weeks for 3% HPC). The next study employed water and was more extensive; the fluorescence tracers in the water could be filtered and reused for mixing in new salts. The water sprays could be investigated further downstream in the atomization region, and more parameters were varied to investigate different mixing characteristics. The water sprays of interest generate highly unsteady liquid sheets and dense droplet fields, which means that the

time-averaged technique will incur less error when making downstream measurements, because of the greater ligament and droplet frequencies.

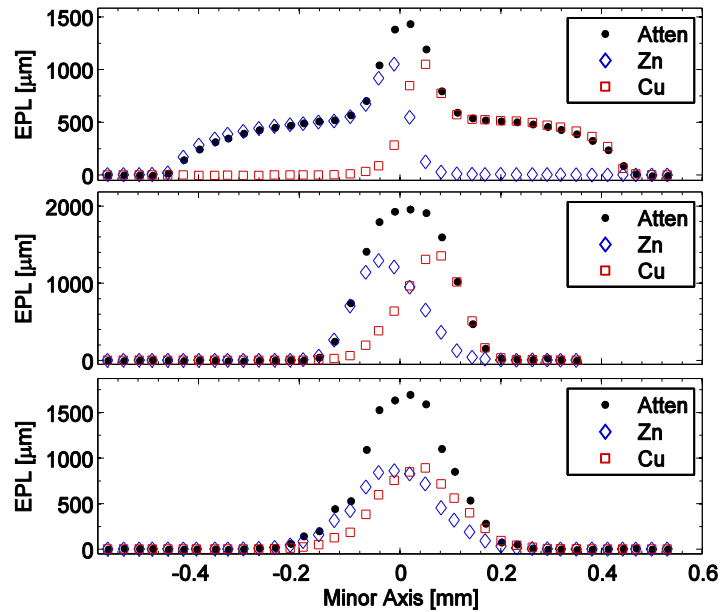


Figure 3-41. 3% HPC at a velocity of 36.5 m/s, -0.5 mm above impingement (top), 0.5 mm below impingement (middle), and 2.5 mm below impingement (bottom).

Liquid Mixing Study

A parametric study was conducted on the mixing of two like impinging jets of water. The technique allows for measurements to be made in the near-field region where the mixing is occurring. There are two dominant mechanisms of mixing, inertial mixing which causes the fluids to transmit through each other near the point of impingement, and turbulent dispersion in which the fluids are mixing in the atomization regime. The parameters of interest are selected to bound these two mechanisms. These include (1) the location where both jets completely overlap, where the mixing factor (defined by Rupe, 1953, Equation 3-6) was a minimum after impingement including the location of this minimum, and (2) the

maximum spread in the centers of mass of each impinging liquid including the location of the maximum.

$$\Phi = 100 \left(1 - \left(\sum_{i=0}^n \frac{w_i}{W} \left(\frac{B - b_i}{B} \right) + \sum_{i=0}^n \frac{\bar{w}_i}{W} \left(\frac{B - \bar{b}_i}{B - 1} \right) \right) \right) \quad (3-6)$$

When the two fluids do no overlap along the line of sight Equation 3-6 equals zero. When the two fluids are perfectly overlapped along the line of sight Equation 3-6 equals one hundred. The local and global mass flow rates are, w and W , respectively, and the local and global mixture ratios are b and B , respectively. The bars above w and b represent values when b is greater than B .

The first parameter is defined by the location of overlap of the centers of mass of each fluorescence profile. This location is linearly interpolated between points just before (Figure 3-32) and just after (Figure 3-33) the overlap occurs. The liquids continue to transmit through each other past the location of overlap. The second parameter, the mixing factor shown in Equation 3-6, is the measure of how “unmixed” the two liquids become, shown in Figures 3-42(b) and 3-43(b). Past this point the liquids continue to spread laterally, and turbulent dispersion enhances the mixing. The spread between the centers of mass of each fluid reaches a maximum and then decreases as the two liquids continue to mix, seen in Figure 3-42(a). The inertial mixing mechanism is thought to dominate up until the minimum in mixing factor is reached, where the centers of mass reach maximum separation after passing through each other. Both the inertial and dispersion mechanisms are present between the minimum in mixing factor and the maximum in center of mass spread. Finally, the dispersion mechanism is thought to dominate after the maximum in separation of the centers of mass. These mixing mechanisms are predominately found when the impinging jets are turbulent prior to

approaching the impingement point. This study is therefore limited to fully-developed turbulent jets.

The quantities expressed in this study have been non-dimensionalized, so trends can be investigated with respect to Reynolds number, included angle, and free jet length to diameter ratios. The angle is described as the sine Θ (or cosine Θ for location parameters), and all length scales are reduced to diameters. The sine is used for mixing parameters where axial momentum may be important, and the cosine is used in location parameters where the momentum normal to the plane of impingement may be important.

Similar to the study of reabsorption correction methods and non-Newtonian sprays the data is collected as raster scans at various horizontal locations both above and below the impingement location. Extracted from these EPL profiles are a set of mixing parameters at each location that serve as the basis of comparison for each spray condition. The mixing parameters are meant to define the mixing phenomena within a spray. These parameters include the location in which both liquids completely overlap, the location and value of the maximum spread between the centers of mass, the location and value of the minimum mixing factor downstream of impingement, and the full width at half the maximum (FWHM) of the EPL profile of both fluids. From this information we can realize where mixing is occurring (overlap location), to what extent the transmission of opposite fluids is occurring (mixing factor), how it is developing in center of mass, and the overall size and shape of the spray (FWHM). This method of data reduction allows for a simple and straightforward analysis of how and when mixing is occurring.

Two examples of the mixing profiles tracking the centers of mass, mixing factor, and FWHM of the EPL profiles are shown in Figures 3-42 and 3-43. All other mixing profiles

including laminar and transitional sprays can be found in Appendix A2, where the plots presented in this section are also co-located. Line plot (a) is tracking the center of mass of each liquid as it progresses downstream. This plot displays both the location of overlap, and the location and maximum spread between the two centers of mass. Each fluid is designated by its fluorescent salt tracer, Zn or Cu. Displayed in line plot (b) is the progression of the mixing factor. Line plot (c) shows the FWHM of the full spray, describing the minor width of the sheet and droplet cloud distribution.

Figure 3-42 shows the downstream profiles of a water spray with an included angle of 60 degrees and a moderate Reynolds number and free jet length. The centers of mass show the two fluids overlapping and then the spread remains constant after about 6 diameters downstream. The middle plot shows that the mixing has not finished at 6 mm but continues throughout the investigated region reaching a minimum mixing factor of 80% around 6 diameters and returning to 90% 20 diameters downstream. It should be noted that the mixing factor should reach 100% when both fluids are completely overlapped. The FWHM profile shows the liquid jets compressing at the impingement point and then spreading out downstream.

The second example profile, Figure 3-43, shows a contrasting condition with an included angle of 90 degrees, a similar free jet length, and more than double the Reynolds number. The jets overlap closer to the point of impingement (shown to coincide with the increase in included angle), and continue along their trajectories through the investigated region. The maximum spread in centers of mass is much greater than Condition 11 (shown to increase directly with included angle and slightly with Reynolds number), and the FWHM is

also greater. The mixing factor again reduces to 80% around 5 diameters downstream but does not return to 90% at the same rate.

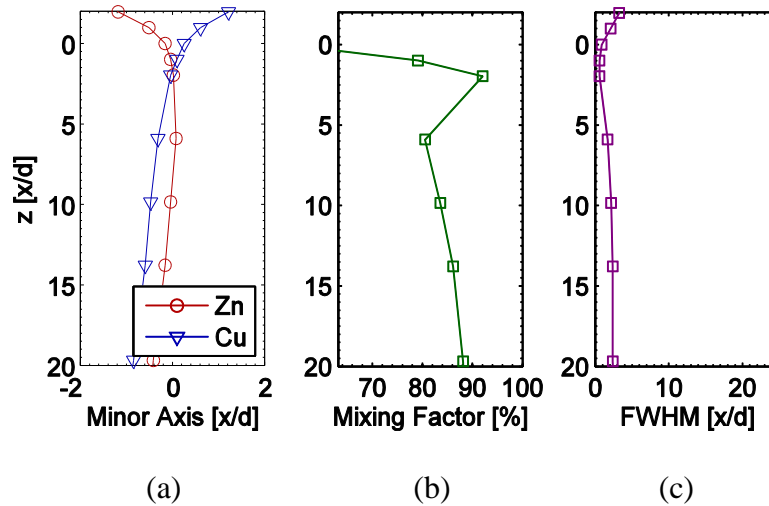


Figure 3-42. Trajectory of the liquid jets(a), mixing factor (b), and overall full width at half maximum (c) for Condition 11, orifice diameter of 0.5 mm, impingement angle of 60 degrees, free jet length of 13 diameters, Reynolds number of 4700.

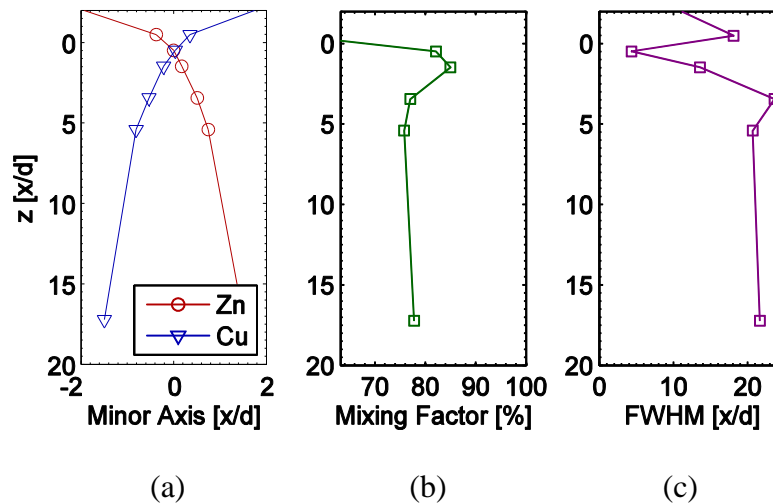


Figure 3-43. Trajectory of the liquid jets (a), mixing factor (b), and overall full width at half maximum (c) for Condition 28, orifice diameter of 0.5 mm, impingement angle of 90 degrees, free jet length of 11 diameters, Reynolds number of 11700.

The following figures show how each input parameter affects the mixing parameters. The input parameters include the sine or cosine Θ ($\sin\Theta$ or $\cos\Theta$), the free jet length (FJ), and the Reynolds number (Re). Other input parameters include the products of each, scaling with the area of the two jets colliding ($\sin\Theta \cdot \text{FJ}$ or $\cos\Theta \cdot \text{FJ}$), scaling with the momentum normal to the plane of impingement ($\sin\Theta \cdot \text{Re}$), scaling with the axial momentum ($\cos\Theta \cdot \text{Re}$), and scaling with the stability of the jets ($\text{FJ} \cdot \text{Re}$).

Shown in Figure 3-44 is the relationship between the cosine Θ and the location of overlap; the relationship is seen to scale quite linearly with the cosine Θ and not be as dependent on the Reynolds number or the free jet length. It follows that the overlap location is a strong function of the injector geometry. As cosine Θ increases the area where the two fluids interact elongates in the axial direction and moves the crossing distance downstream. Displayed in Figures 3-45 and 3-46 are the minimum mixing factor and location vs. the sine and cosine Θ respectively; they both scale well linearly. The increase in sine Θ allows more fluid to transmit and the increase in cosine Θ moves the location of minimum mixing following the trends of increased momentum in axial and normal to mixing plane directions respectively. Presented in Figures 3-47 and 3-48 are the relationship between the sine Θ and cosine Θ and the spread in the centers of mass and location, respectively. The effect of sine Θ is nearly linear with dominant effects from the free jet length and or the Reynolds number, following momentum trends.

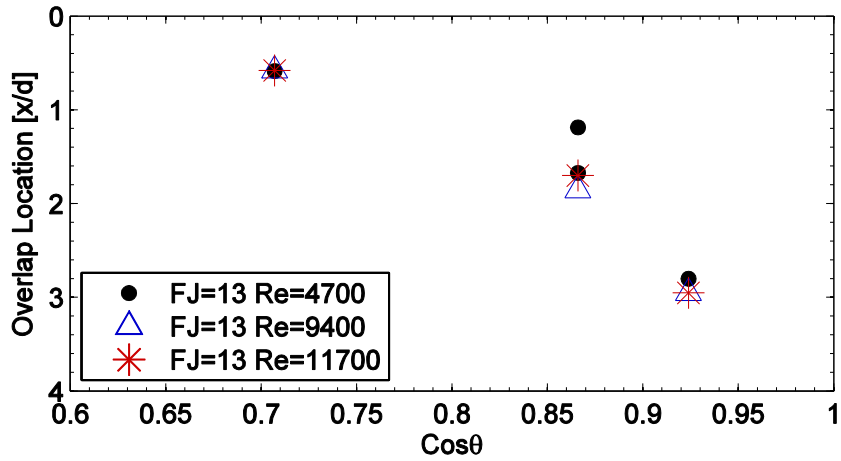


Figure 3-44. Plot showing the location of overlap vs. cosine Θ ; the data points are grouped by free jet length and Reynolds number.

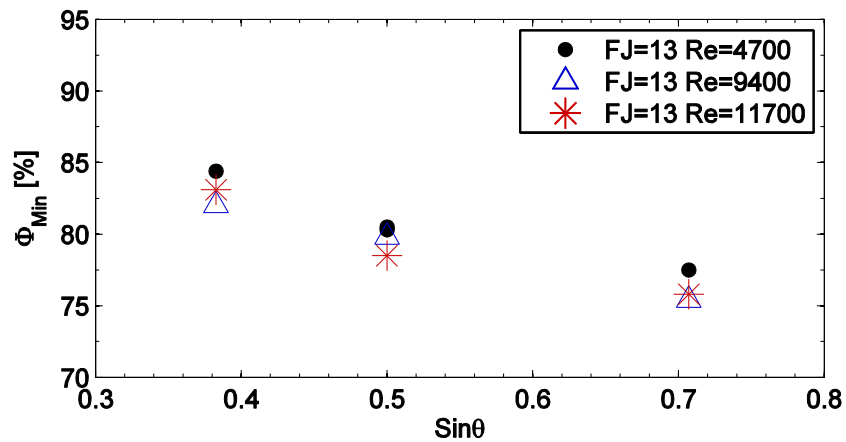


Figure 3-45. Plot showing the minimum mixing factor (Φ) vs. sine Θ , the data points are grouped by free jet length and Reynolds number.

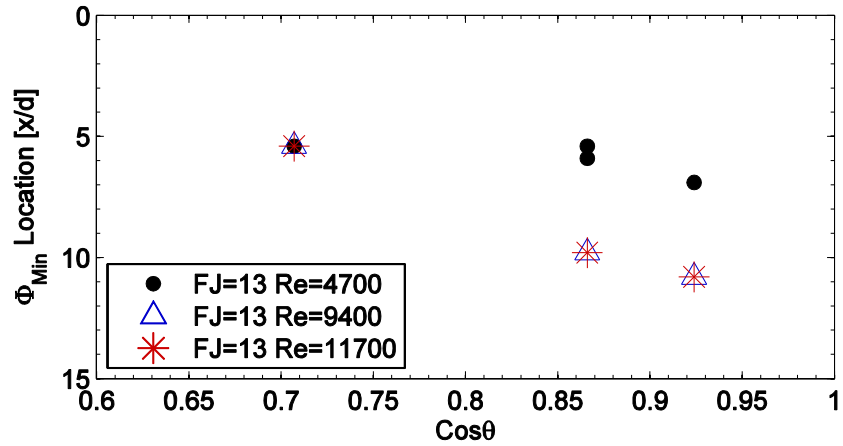


Figure 3-46. Plot showing the location of the minimum mixing factor (Φ) vs. cosine Θ ; the data points are grouped by free jet length and Reynolds number.

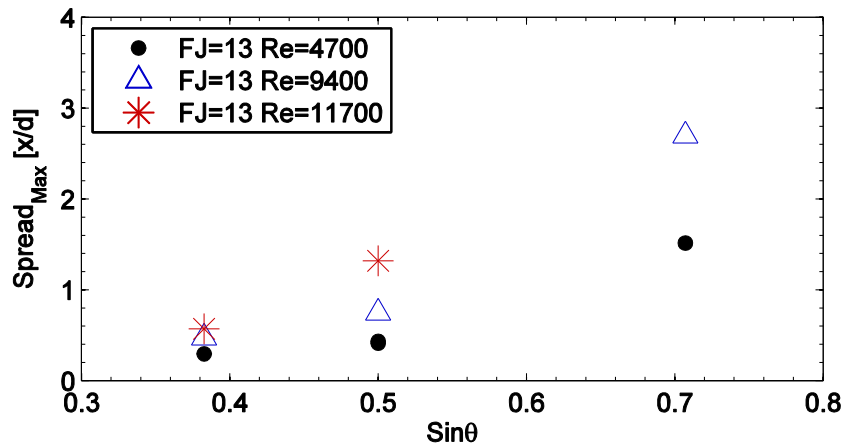


Figure 3-47. Plot showing the maximum spread in centers of mass vs. sine Θ ; the data points are grouped by free jet length and Reynolds number.

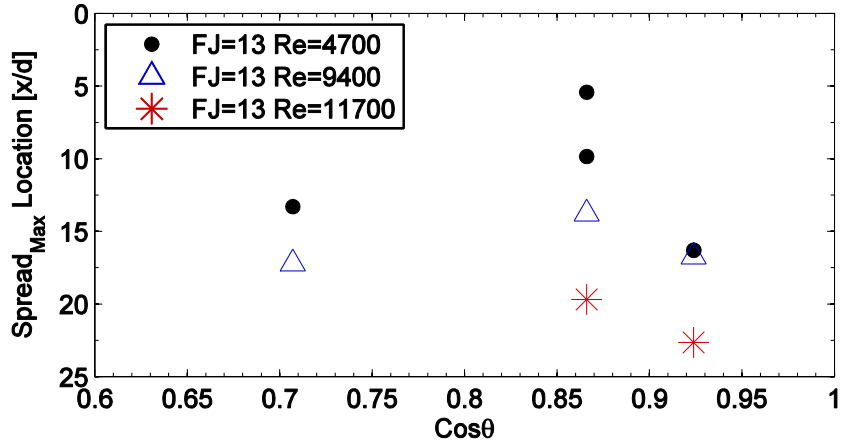


Figure 3-48. Plot showing the location of the maximum spread in centers of mass vs. cosine Θ ; the data points are grouped by free jet length and Reynolds number.

Presented in Figure 3-49 is the free jet length versus the overlap location. The relationship on mixing of the free jet length again is shown in Figures 3-50 through 3-53, where the minimum mixing factor (including location) and the maximum spread in centers of mass (including location), respectively, remain constant. There does not appear to be a strong relationship between the free jet length and the mixing parameters.

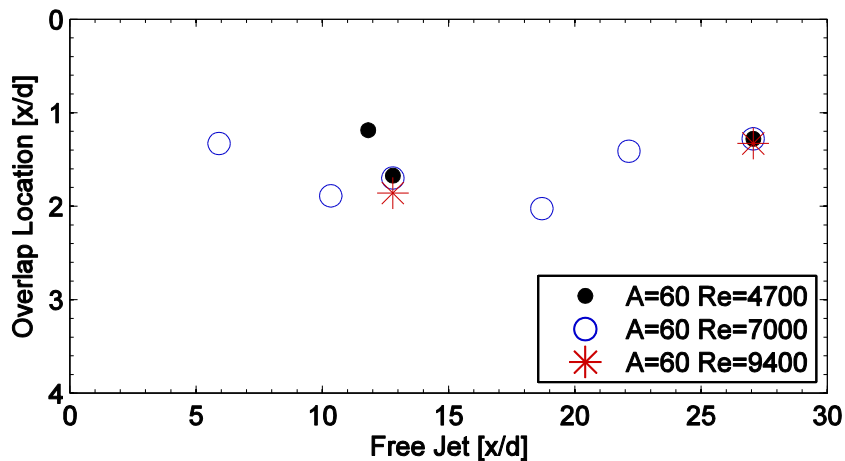


Figure 3-49. Plot showing the location of overlap vs. the free jet length; the data points are grouped by angle and Reynolds number.

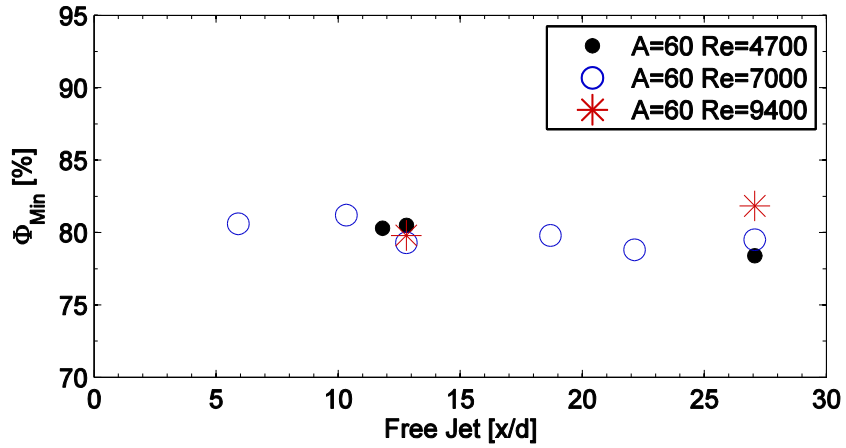


Figure 3-50. Plot showing the minimum mixing factor (Φ) vs. the free jet length; the data points are grouped by angle and Reynolds number.

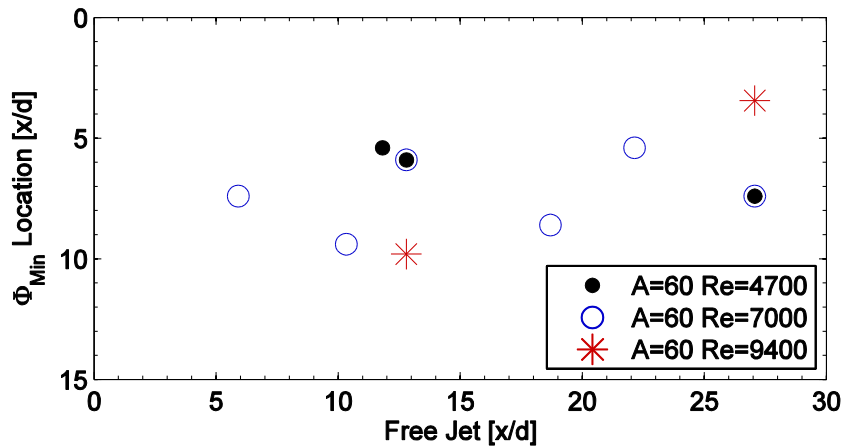


Figure 3-51. Plot showing the location of the minimum mixing factor (Φ) vs. the free jet length; the data points are grouped by angle and Reynolds number.

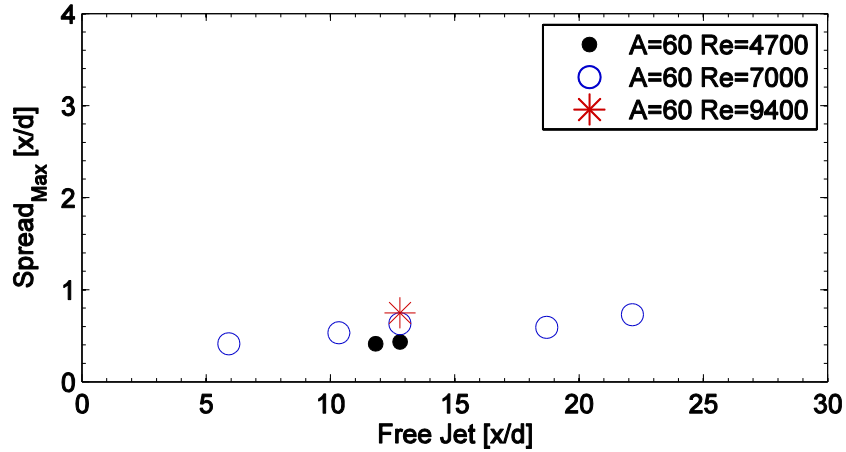
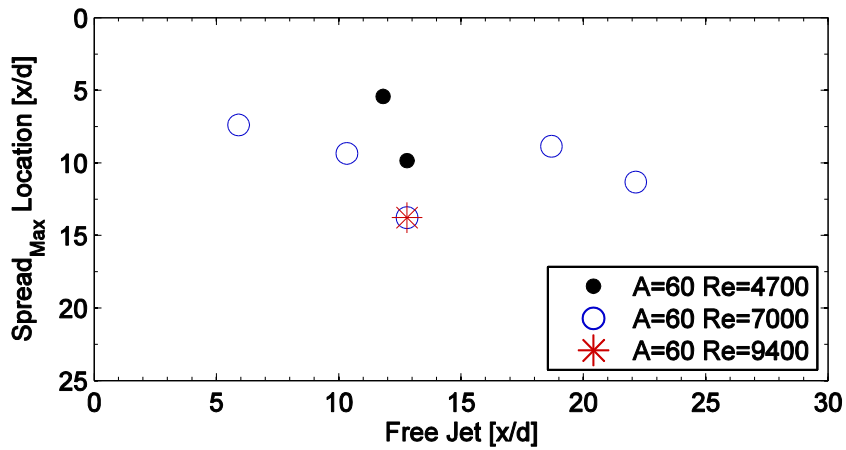


Figure 3-52. Plot showing the maximum spread in centers of mass vs. the free jet length; the data points are grouped by angle and Reynolds number.



(b)

Figure 3-53. Plot showing the location of the maximum spread in centers of mass vs. the free jet length; the data points are grouped by angle and Reynolds number.

Figure 3-54 shows the overlap location vs. the Reynolds number. The overlap location is fairly constant at a range of Reynolds numbers, but can change with the angle of impingement since it was shown earlier that it is not a strong function of free jet length. The

minimum in mixing factor (including location) depend somewhat on the included angle but weakly on the Reynolds number, as shown in Figures 3-55 and 3-56. The maximum spread in the centers of mass (including location) displayed in Figures 3-57 and 3-58 shows a likely trend dependent upon the Reynolds number. An increase in Re and momentum, increases the spread between centers of mass and in a sense pushes the occurrence downstream.

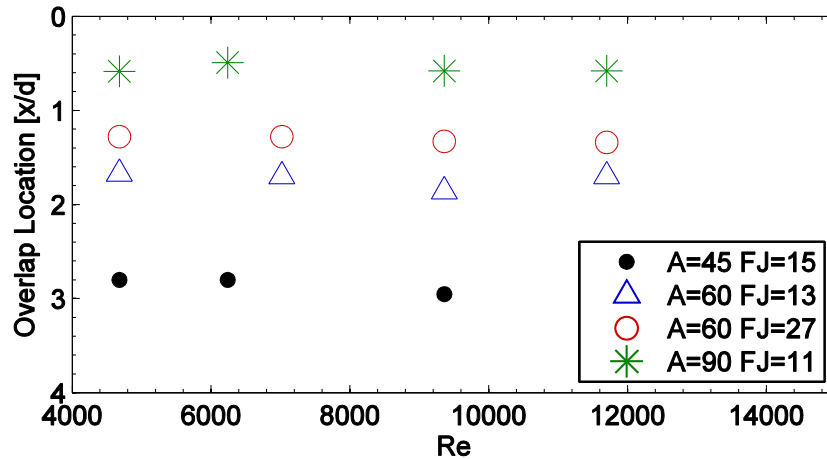


Figure 3-54. Plot showing the location of overlap vs. the Reynolds number; the data points are grouped by angle and free jet length.

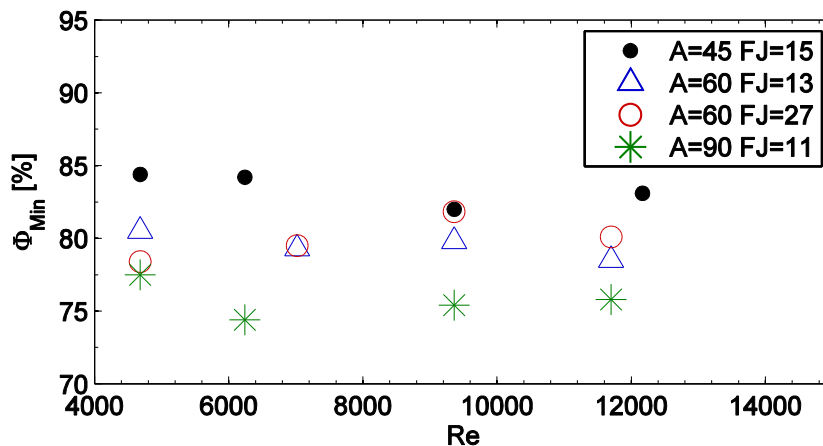


Figure 3-55. Plot showing the minimum mixing factor (Φ) vs. the Reynolds number; the data points are grouped by angle and free jet length.

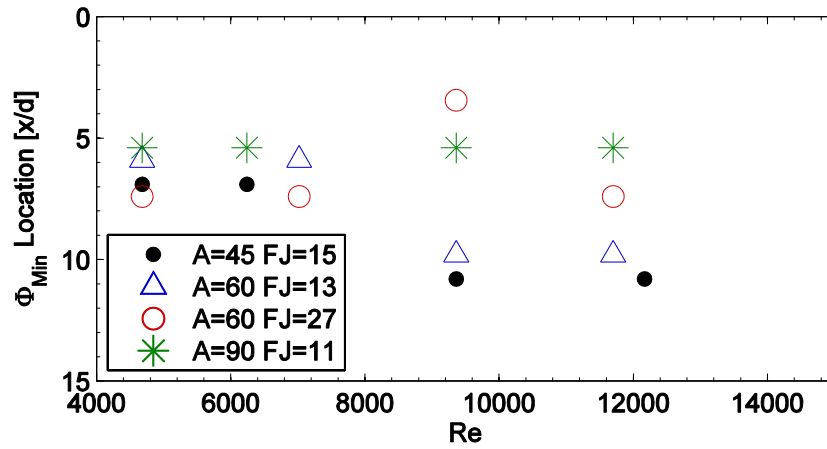


Figure 3-56. Plot showing the location of the minimum mixing factor (Φ) vs. the Reynolds number; the data points are grouped by angle and free jet length.

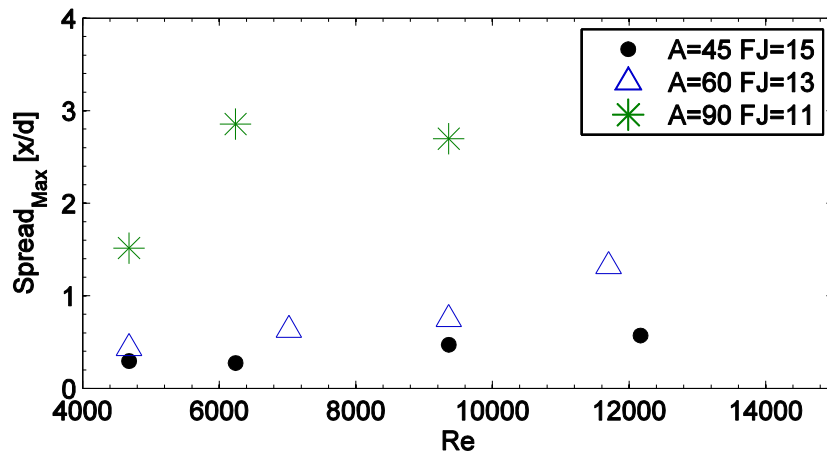


Figure 3-57. Plot showing the maximum spread in centers of mass vs. the Reynolds number; the data points are grouped by the angle and free jet length.

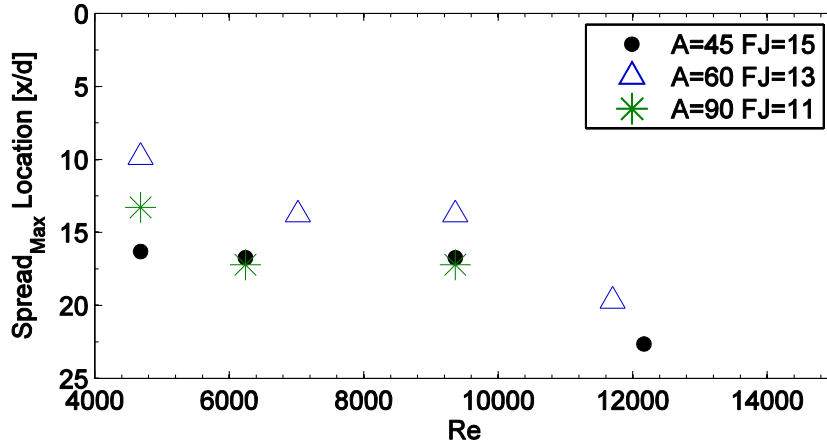


Figure 3-58. Plot showing the location of the maximum spread in centers of mass vs. the Reynolds number; the data points are grouped by the angle and free jet length.

Displayed in Figures 3-59 through 3-61 are the overlap location and minimum mixing factor (including location), respectively, vs. the product of the free jet length and the sine Θ . The data are grouped by Reynolds number, and there does not seem to be a strong dependence shown.

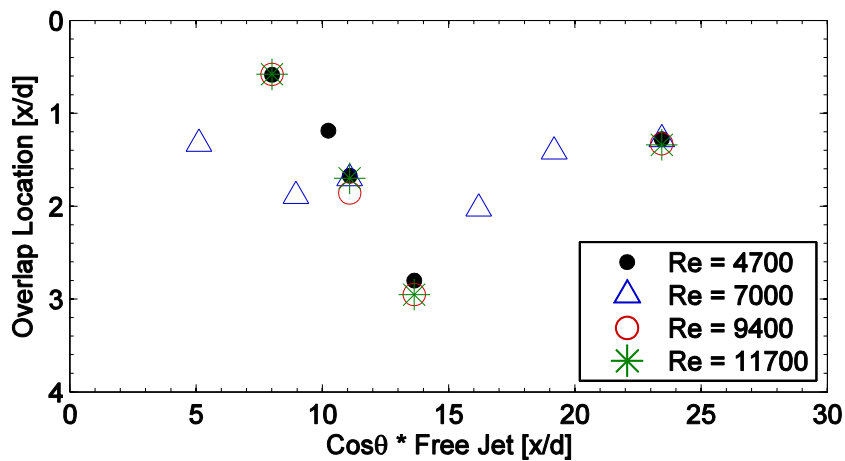


Figure 3-59. Plot showing the location of overlap vs. the product of the cosine Θ and the free jet length; the data points are grouped by Reynolds number.

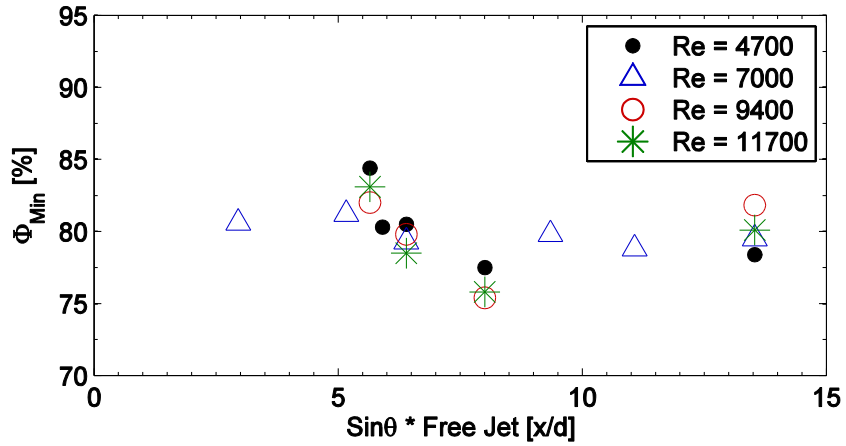


Figure 3-60. Plot showing the minimum mixing factor (Φ) vs. the product of the sine Θ and the free jet length; the data points are grouped by Reynolds number.

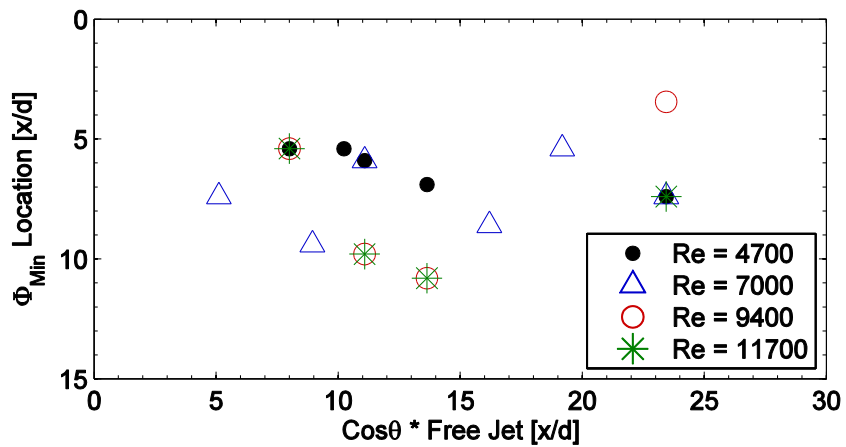


Figure 3-61. Plot showing the location of the minimum mixing factor (Φ) vs. the product of the cosine Θ and the free jet length; the data points are grouped by Reynolds number.

There does not appear to be a relationship between the spread in centers of mass (including location) and the product of the free jet length and sine Θ , shown in Figures 3-62 and 3-63.

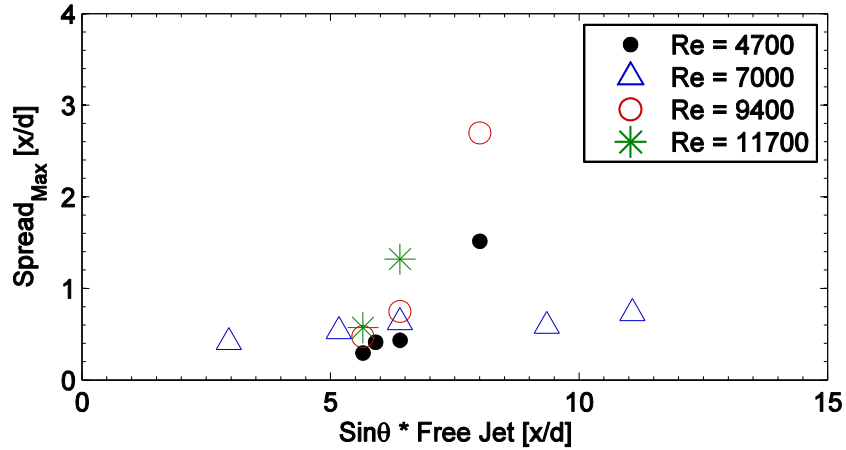


Figure 3-62. Plot showing the product of the maximum spread in centers of mass vs. the product of the sine θ and the free jet length; the data points are grouped by Reynolds number.

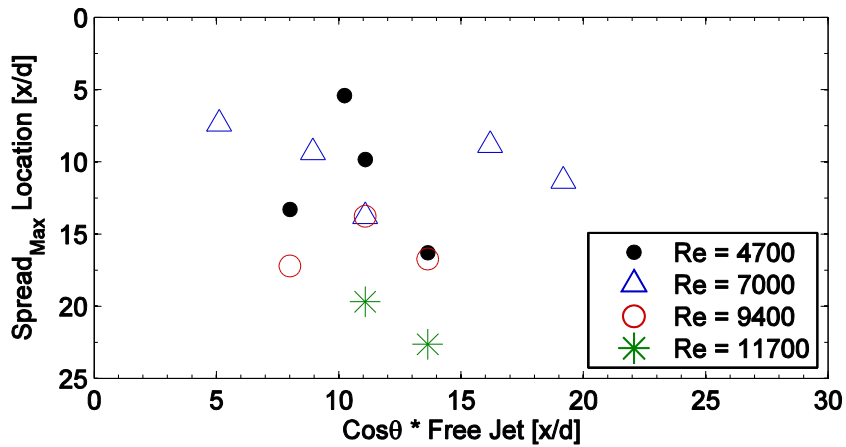


Figure 3-63. Plot showing the product of the location of the maximum spread in centers of mass vs. the product of the cosine θ and the free jet length; the data points are grouped by Reynolds number.

As displayed in Figure 3-64, the overlap location appears to be quite constant with the product of the Reynolds number and the cosine θ . In this case, there appears to be a

relationship between the overlap location and free jet length. However, the case of the free jet length of 27 appears to be an anomalous data set.

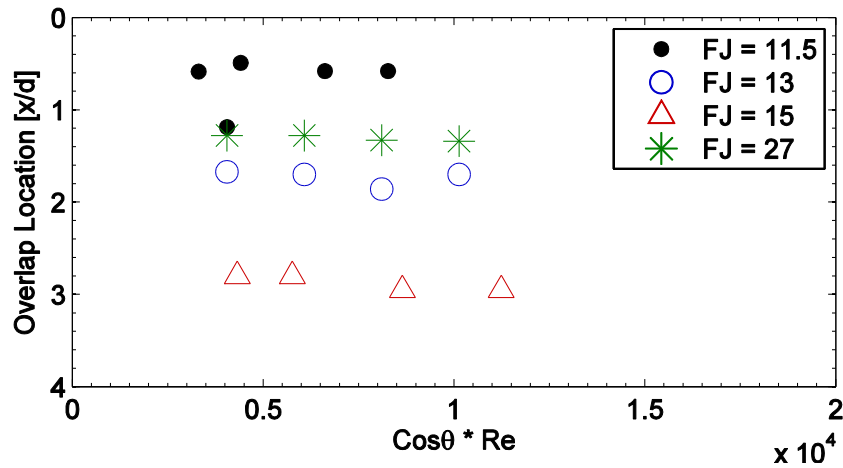


Figure 3-64. Plot showing the location of overlap vs. the product of the Reynolds number and the cosine Θ ; the data points are grouped by free jet length.

Shown in Figures 3-65 and 3-66, there appears to be a slight linear relationship between the minimum mixing factor and the product of the Reynolds number and the sine Θ . This is potentially physically meaningful. As the product of Reynolds number and sine Θ describes the momentum normal to the plane of impingement, a greater momentum means more fluid should transmit through to the opposing side. As Presented in Figures 3-67 and 3-68, the horizontal momentum also has an effect on the spread between centers of mass, in which the free jet length may also play a role, and the momentum normal to the plane of impingement also has an effect on the location where the maximum spread occurs.

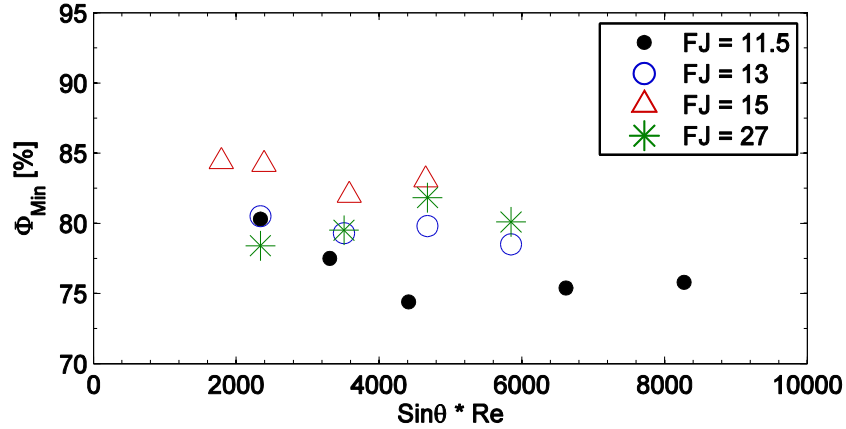


Figure 3-65. Plot showing the minimum mixing factor (Φ) vs. the product of the Reynolds number and the sine Θ ; the data points are grouped by free jet length.

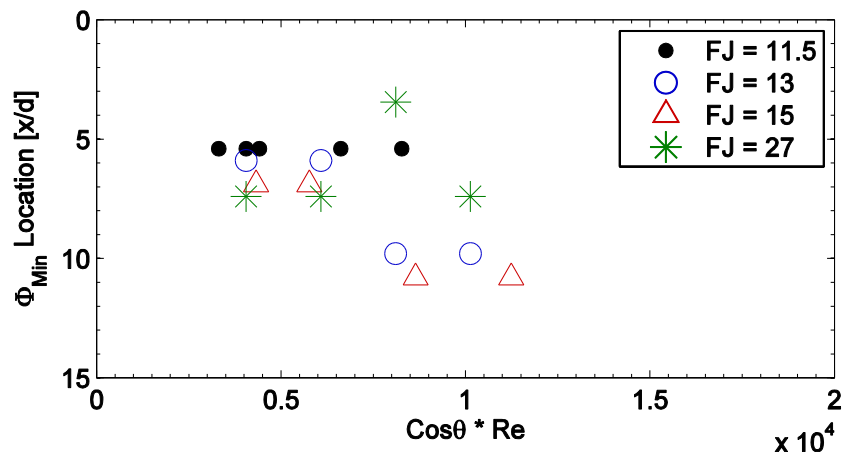


Figure 3-66. Plot showing the location of the minimum mixing factor (Φ) vs. the product of the cosine Θ and the Reynolds number; the data points are grouped by free jet length.

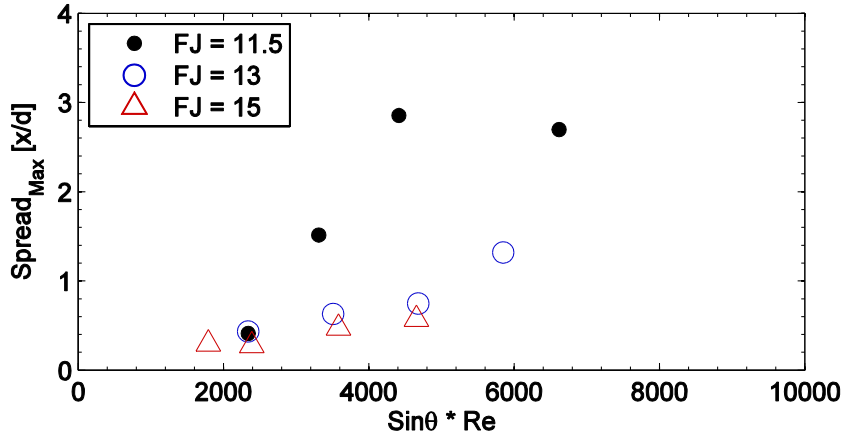


Figure 3-67. Plot showing the maximum spread in centers of mass vs. the product of the Reynolds number and the sine Θ ; the data points are grouped by free jet length.

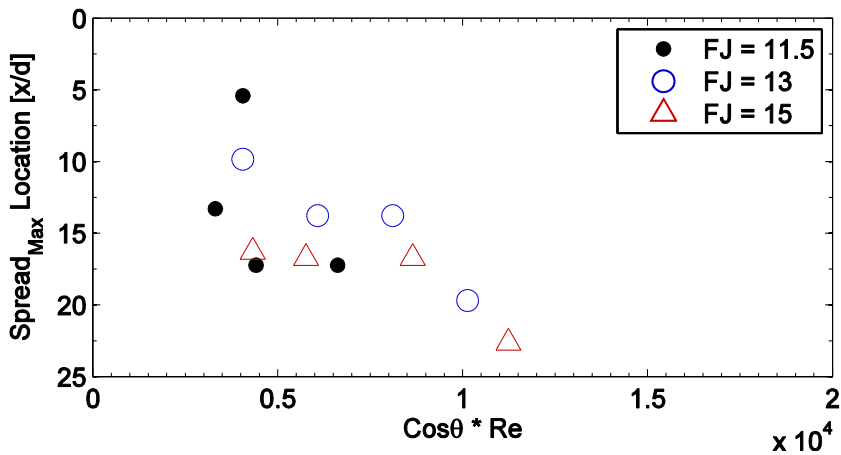


Figure 3-68. Plot showing the location of the maximum spread in centers of mass vs. the product of the cosine Θ and the Reynolds number; the data points are grouped by free jet length.

The instability of the jet at the point of impingement, represented by the product of the free jet length and Reynolds number, does not appear to have a great effect on the overlap location, as shown in Figure 3-69, although there is a strong dependence on the impingement

angle. A similar trend with angle follows for the minimum mixing factor (including location) shown in Figures 3-70 and 3-71. Displayed in Figures 3-72 and 3-73 there appears to be a slight linear dependence with the jet instability.

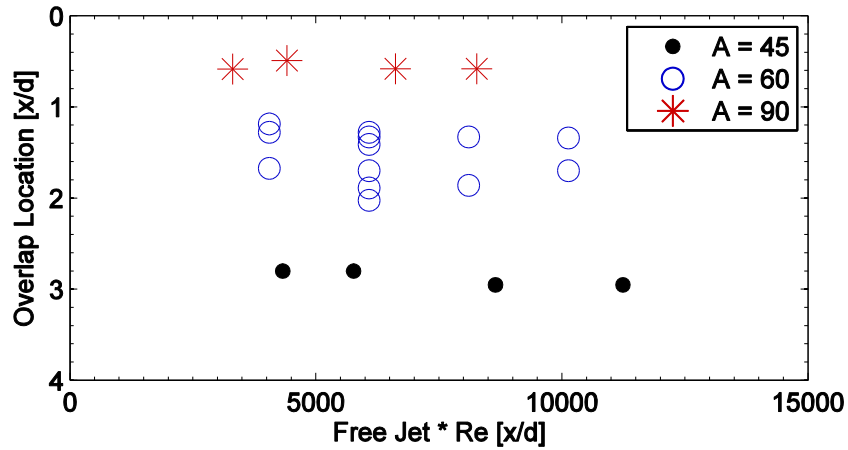


Figure 3-69. Plot showing the location of overlap vs. the product of the free jet length and Reynolds number; the data points are grouped by angle.

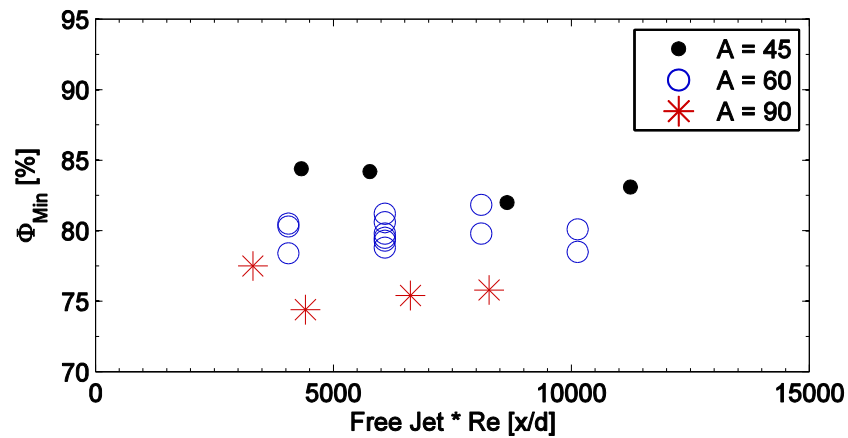


Figure 3-70. Plot showing the minimum mixing factor (Φ) vs. the product of the free jet length and Reynolds number; the data points are grouped by angle.

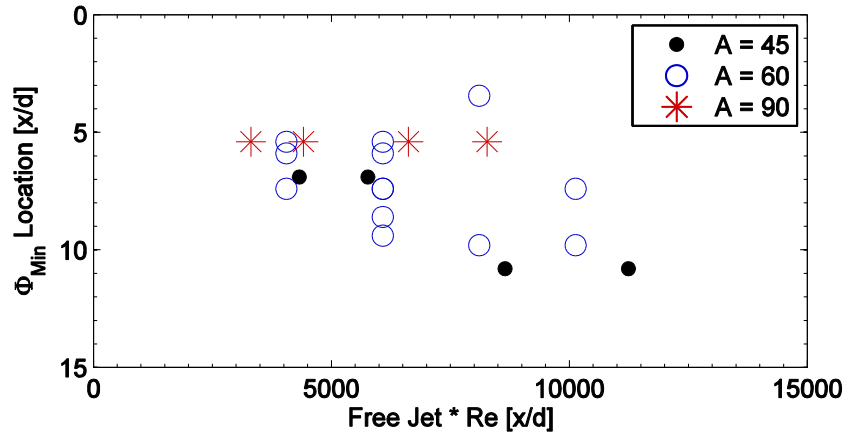


Figure 3-71. Plot showing the location of the minimum mixing factor (Φ) vs. the product of the free jet length and the Reynolds number; the data points are grouped by angle.

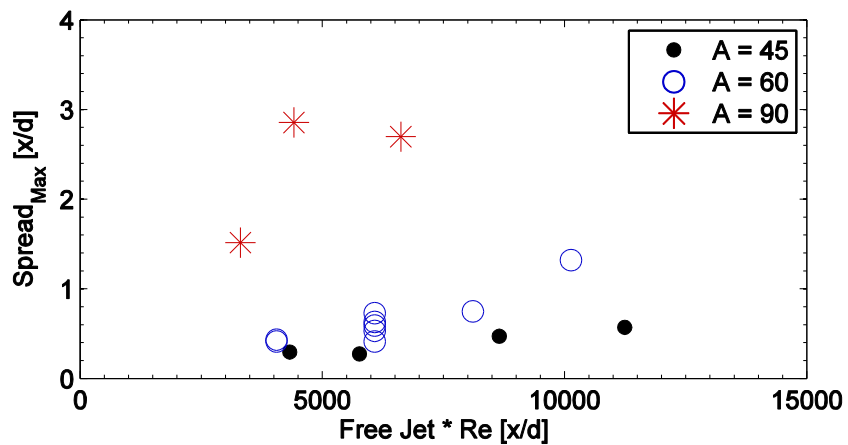


Figure 3-72. Plot showing the maximum spread in centers of mass vs. the product of the free jet length and Reynolds number; the data points are grouped by angle.

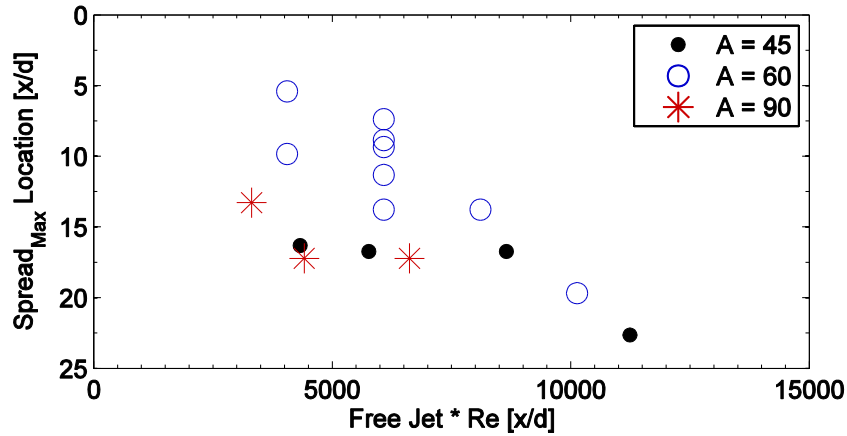


Figure 3-73. Plot showing the location of the maximum spread in centers of mass vs. the product of the free jet length and the Reynolds number; the data points are grouped by angle.

The relationships shown in the previous figures are further investigated through multivariate linear regression using Matlab. The general form of the empirical equation determined through multivariate linear regression is shown in Equation 3-7 and 3-8, which includes the three main input parameters, the sine or cosine Θ , the free jet length and the Reynolds number. Again the products of each are included to show their overall dependences on the output mixing parameters.

$$Y = b_1 + b_2 \sin(\theta) + b_3 FJ + b_4 \sin(\theta) FJ + b_5 Re + b_6 \sin(\theta) Re + b_7 FJ Re + b_8 \sin(\theta) FJ Re \quad (3-7)$$

$$Y = b_1 + b_2 \cos(\theta) + b_3 FJ + b_4 \cos(\theta) FJ + b_5 Re + b_6 \cos(\theta) Re + b_7 FJ Re + b_8 \cos(\theta) FJ Re \quad (3-8)$$

Once the equations were determined, the output variables were compared with the experimental values and the average absolute difference was determined by taking the RMS value. These RMS values as well as the coefficients determined through regression are shown in Table 3-4.

Table 3-4. Empirical equation coefficients of mixing parameters given angle, free jet length and Reynolds number.

Y	b1	b2	b3	b4	b5	b6	b7	Error
Overlap	39.1	-43.7	-3.76	-8.00E-05	4.35	0.00018	-2.97E-06	8%
PHI	79.5	12.8	1.37	-0.00114	-3.41	0.00078	4.05E-05	0.80%
PHI Location	10.5	-12.5	0.382	-0.00213	-0.0968	0.00389	-5.17E-05	12%
Spread	-13.7	26.3	0.958	-0.00011	-1.85	0.0005	-2.52E-06	13%
Spread Location	441	-588	-30.5	0.00064	41.4	0.0121	-0.00075	10%

The effects of each of the input parameters or products of input parameters can be seen as the magnitude and sign of each coefficient. The error is taken as the RMS value when comparing the regression model to the experimental data. The error in all cases is small, ranging from 0.8% to 13%. One major cause of the error may be that the free jet length has been shown to affect the mixing process in a non-linear manner. This full effect was not captured in the data set collected and used for the analysis. The simplification of this phenomenological description leads to errors nearly equivalent to the experimental errors, which are discussed in the following chapter. It is important to note that care should be taken when interpreting the trends found in the data. Based on the limited number of data points and spread in the data definite conclusions are difficult to discern, but trends do agree with physical intuition.

CHAPTER IV

UNCERTAINTY ANALYSIS

Uncertainty Propagation

It is necessary and proper to analyze the uncertainty in any measurement system prior to surmising any and all conclusions. The uncertainty includes all physical limitations, and random and bias errors. These restrictions place bounds on the uncertainty of all the data presented. This section provides a thorough analysis of the measurement uncertainty to provide validation for the conclusions drawn and begin the discussion of future measurements and measurement capabilities. The analysis includes measurement noise, random errors, and bias errors originating from fluid properties, spray hardware, scientific equipment, data processing, and the final analysis of data. The uncertainties are propagated through the experiment and analysis. The uncertainty of each measurement parameter has been determined and presented in Table 4-1 and discussed.

The parameters have been divided into four categories: experimental parameters, spray parameters, output parameters, and regression parameters. The experimental parameters include: the injector angle, geometry, and orifice diameter; the rotameters; and the high-pressure spray rig, including the linear potentiometer and the cylinder diameter. The uncertainty values were determined by a number of methods. The half mark determination is defined by half the distance between the two smallest marks on a scale, used for the rotameter readings. If the measurement was difficult as with the angle and free jet length, a repeatability study was done analyzing the free jet prior to impingement. The angles and free jet lengths were determined by tracking the centers of mass of the free jets prior to

impingement. Manufacturing tolerances were used for the diameters of the injector orifice and gel cylinders. The error in the linear potentiometer used for setting the velocity in the gel rig was estimated by the standard deviation of repeated attempts to get the same velocity. The uncertainty values for the spray parameters were calculated from the associated experimental parameters, as shown in Table 4-1. The output parameter uncertainty was determined through a few repeated conditions over a range of orifice diameters. The uncertainty in the regression outputs was taken as the RMS difference of the output parameters determined experimentally and through the regression equations.

The uncertainties from the output parameters are larger than the uncertainties from the spray parameters. This increase in uncertainty is due to the estimation of the output parameters from the data collected. For example, a line scan was usually not taken exactly where the fluids would overlap, so this location had to be linearly interpolated. The minimum mixing factor and maximum center of mass spread were not interpolated but taken as least and greatest values found in each data set, respectively. It proved highly unlikely to obtain an accurate curve fit to the data to use an interpolated value for the center of mass spread and mixing factor. A greater number of data points would have allowed for interpolation. The uncertainties found from the output parameters are close to the uncertainties of the regression parameters. This lends credence to the accuracy of the empirical equations derived in the Results chapter. One would not expect the regression uncertainties to be lower than the experimental uncertainties. Likewise if the regression uncertainties were too much greater than the output uncertainties they would not be deemed very useful.

Table 4-1. Uncertainty analysis for each measurement parameter.

Parameters	% Uncertainty	Determination
<i>Experimental Parameters</i>		
Injector Angle	1.0	Repeatability
Injector Geometry	1.0	Repeatability
Injector Orifice Diameter	2.5	Manufacturing Tolerance
Rotameter	1.0	Half Mark
Potentiometer	5.0	Repeatability
Gel Cylinder	2.5	Manufacturing Tolerance
Fluor. Water Density	1.0	Repeatability
Fluor. Water Viscosity	1.0	Repeatability
<i>Spray Parameters</i>		
Reynolds Number	4.7	Calculated from Experimental Parameters
Reynolds Number Gel	7.2	Calculated from Experimental Parameters
Free Jet Length	2.9	Calculated from Experimental Parameters
Sin θ	1.0	Calculated from Experimental Parameters
Sin θ * FJ	3.0	Calculated from Experimental Parameters
Sin θ * Re	4.8	Calculated from Experimental Parameters
FJ * Re	5.5	Calculated from Experimental Parameters
<i>Output Parameters</i>		
Fluid Profile Overlap	10.0	Repeated trials
Mixing Factor (Φ)	2.0	Repeated trials
Center of Mass Spread	10.0	Repeated trials
<i>Regression Parameter</i>		
Fluid Profile Overlap	9 / 14	RMS/SD Exp. vs Reg.
Mixing Factor (Φ)	1.5 / 1.6	RMS/SD Exp. vs Reg.
Center of Mass Spread	15 / 15	RMS/SD Exp. vs Reg.

Sources of Uncertainty

The fluid properties of water were altered with the addition of gels, glycerol, and salts; any error in the amounts added would propagate to errors in their fluid properties. All additions to the water were made on a mass basis using a scale. The scales used were all

precise to within 0.1% of the measured values. The measurements of fluid properties such as density, viscosity, and surface tension were accurate to within 1%, based on repeating the measurement 10 times.

The spray hardware comprises any equipment used to flow or measure the flow of the fluid being sprayed. The three components to be analyzed are the injector, the flow rate measurement devices, the source of pressure for the flow, and the APS translation stages used for raster scanning through the spray.

The injector has three main attributes that can alter the flow, including the orifice diameter, the orifice flow passage entrance lip within the injector, and any manufacturing errors causing a deviation from an ideal injector of known geometry. The orifice diameters employed were 0.5 mm and 1.0 mm \pm 2.5%. This uncertainty was taken from the manufacturers who prepared the orifices using wire electrode discharge machining. This method was chosen for its high degree of accuracy and smooth bore finish. Deviations in the diameter from the given values would change the diameters and velocities of the jets at a given flow rate. The orifice flow passage entrance lip was chamfered, and the ratio of the length of the orifice passage within the injector to the diameter was above 20; from this we assumed underdeveloped laminar flow and fully developed turbulent flow depending on the flowrate. The turbulent flow regime was of most practical interest, and the overall geometries were chosen to loosely match previously collected data. Manufacturing defects are believed to be minimal and were not investigated because of the cost of purchasing several of the same type of injector.

The liquid flow rate was measured with two rotameters with a manufacturing uncertainty of 1.5% at the average flow rate. The gel flow rates were determined by a linear

displacement potentiometer attached to the piston in the gel rig. The uncertainty in the velocity measurement of 7.1% is a function of the cylinder area, the injector orifice area, and the linear potentiometer.

The spray collection chamber may have also had an effect on the spray. During the radiography measurements droplets were collecting on the windows so air jets were installed to blow the droplets from the window surfaces. The spray did not appear to be effected by the air jets on the windows. The spray was rotated for the fluorescence measurements, which increased the unwanted number of droplets collecting on window surfaces. During these measurements the windows were replaced with open tubes that had a low inward flow rate of air passing through them. This flow rate was much lower than the initial air jet flow rate for the windows and was also determined by visual inspection to not be affecting the flow physics. The chamber that the injector sprayed into was evacuated into an exhaust duct, further disrupting the air flow surrounding the spray.

A twin-gear pump was used for some radiography measurements to create an infinite flow loop so that liquid from the injector could be resupplied back to the injector and facilitate longer data collection times. The pump was undampened during the first measurements, and to keep the flow consistent the pump was left undampened. This simplified flow system also allowed ease of travel to the various locations where a variety x-ray measurements were performed. These were used to compare measurement techniques and not define the flow behavior. All measured flows used to analyze the underlying flow physics in this work used a tank pressurized by either nitrogen or shop air rather than the oscillating gear pump. The pressurized tank design of the flow system allowed for steady and consistent velocities.

Photon source and detection equipment uncertainties also affect the measured values. The sources include the continuous tube, flash tube, and synchrotron x-ray sources. The sources of uncertainty from the x-ray sources are shot noise and geometric parameters of the tube sources.

The shot noise of the synchrotron is orders of magnitude less than the precision of the detection equipment, and so it was not accounted for in the analysis. The translation stages used at the APS have a precision of 0.5 μm . The absolute spatial scale was set by locating the injector tip in the beam and then centering the spray profile along the x or y axis depending on which measurement is being performed. The uncertainty in the absolute location can be estimated to be 10 μm .

The shot noise of the tube sources became apparent when collecting time-resolved and high-speed measurements. The shot noise was coupled with the detection noise and would change based on the experimental set up. These precisions and accuracies are taken from the data for each experiment and described in the results section. The tube sources emit x-rays in a cone beam from a finite size anode, which causes several effects that require attention. The cone beam both distorts the image of the object from what would be imaged if using parallel beams, as well as induces magnification. The time-averaged tube source measurements that were compared with the synchrotron employed a geometry where the spray was far from the anode, this reduced the effect of distortion. The agreement in the overlap of the plots show the distortion was minimal and did not greatly affect the outcome of the measurements. The finite size of the anode induced a penumbra and magnification on the image, as shown in Figure 4-1. This geometric blur was reduced as much as possible while still retaining enough flux to create an image. The exact amount of blur from this was

not isolated as it was coupled to blur associated with the detection system. The final amount of blur was determined to be acceptable and is reported in the results section.

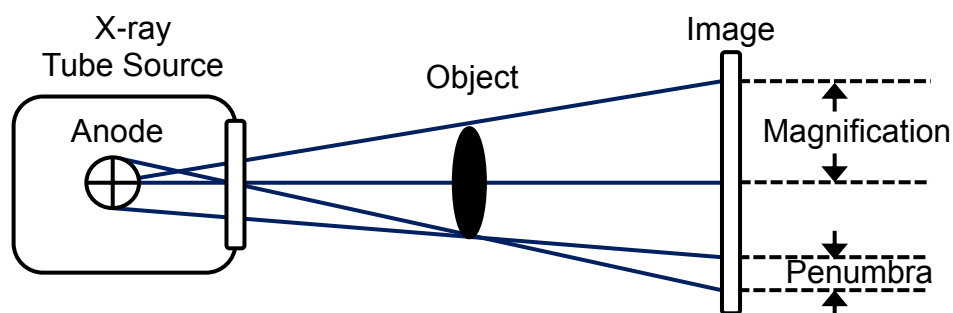


Figure 4-1. Schematic of tube source showing the ray tracing for magnification and penumbra.

Three detectors were used at the APS, an unbiased PIN diode to measure the transmission of x-rays, a crystal analyzer to measure fluctuations in the incoming x-ray beam, and a silicon drift diode (SDD) to detect the fluorescence x-rays during the mixing measurements. The uncertainty of these detectors is coupled and shown in the results section as fluctuations in the flat-field measurements. It is assumed that the spray or the amount of attenuation or fluorescence does not affect the absolute uncertainty. This is not necessarily true for the silicon drift diode, which is an energy-resolved single-photon-counting detector. If an excess of photons are incident upon the detector in a certain amount of time, the detector cannot resolve all of them. This effect is accounted for in the processing of the fluorescence signals.

The tube source images were collected using a CCD camera or an intensified CMOS camera, both lens-coupled to a phosphor. As previously stated, the uncertainties of the camera and intensifier are coupled with the shot noise of the source and is reported in the flat field. The phosphor, intensifier, and limited pixel count of the camera chip also decrease the

resolution of the imaging system. Since these are all closely coupled and depend of the specific geometry of the imaging system, the uncertainties are reported in the results section. The spatial scale uncertainty is estimated to be 1 pixel, or in the range of 44 to 120 μm , which is at least three times less than the spatial resolution of the images.

The raw data are processed through several steps to reveal the quantitative information. Each of these steps may increase or decrease the level of uncertainty. The main processing procedures are a dark current subtraction and flat-field normalization. The dark current is taken when there are no photons incident upon the detector. The subtraction of this value does not appreciably change the uncertainty. The flat-field image is acquired under normal imaging conditions without the spray present. The flat-field image is taken as an average of 100 or 1000 images to smooth out and shot-to-shot fluctuations. Then the spray images are divided by the flat-field image to resolve a transmission map. The division does induce some pixel-to-pixel noise from the flat-field image, but the overall enhancement of normalization greatly outweighs this effect.

Once the signals are normalized they are further processed to determine information on liquid mass distribution. The radiographic measurements require the conversion from transmission to absolute path length of liquid. This is accomplished using the Beer-Lambert Law and a known or previously determined attenuation coefficient. The law and methods by which the attenuation coefficient is determined have been previously stated, but the uncertainty in the variable attenuation coefficient has not been discussed. This method of characterizing the attenuation coefficient requires *a priori* knowledge of the jet diameters and the errors associated with using different jet diameters to obtain a step-wedge like effect. Visible light images were used to determine the diameters of the liquid jets used for

calibration, and their uncertainty was estimated to be around 5%. The liquid jets are cylindrical and contain a variation of path lengths across their profile. The average attenuation of each jet is taken and associated with a single average level of photon transmission. Calculations were made to investigate the effects of using a cylindrical object as one with no variation in path length. It was found that the maximum error was 2% when the jet diameters are small and reduced with larger diameters. Furthermore it was not feasible to image liquid jets of diameters less than ~300 micron because of spatial resolution. The end result is an estimated variable attenuation coefficient dependent on photon transmission. The values of the attenuation coefficient were used to show that the imaging techniques would have sufficient attenuation (i.e., contrast), and it was found that beam hardening would require a more careful method to make and compare measurements of mass distribution. The processing of the fluorescence signals requires several steps. Therefore the precision of measurement is unaffected by the processing, and the accuracy is taken in comparison with the radiographic attenuation data. The resulting value of the accuracy is absolute difference between the mass distributions determined via attenuation and fluorescence.

The method by which the final processed signals are analyzed can reduce some of the uncertainty previously attained through the measurements. An example of this would be investigating an integrated or averaged value. The comparison between the tube source measurements and synchrotron measurements was made by investigating the signal profiles and spectral domains. Both of these aspects are not very susceptible to the accuracy of a single point but rather the average behavior, whether it be a time averaged point or averaged spectra from a set of points.

The magnitudes of the errors presented in this section are reasonable and allow us to propose conclusions based on the observations, as found in the following chapter.

CHAPTER V

CONCLUSIONS

Mass Distribution

Laboratory scale x-ray tube sources are shown to yield quantitative results similar to those of a synchrotron source for both time-averaged and time-resolved measurements. Simultaneous high-speed radiographic images were collected with visible light images to understand changes in overall spray shape and effects on mass distribution. Newtonian and non-Newtonian impinging jets were studied while varying gel loading and velocity.

Time-averaged Measurements

The tube source validation study evaluated the use of narrowband and broadband x-ray tube sources for quantitative measurement of liquid mass distributions in atomizing sprays. By comparing broadband attenuation data with measurements using a narrowband x-ray source from the synchrotron facility at the APS of Argonne National Laboratory, it was possible to determine the relative error and uncertainty of the EPL for varying spray conditions. For the broadband x-ray imaging system used in the current work, it was found that measurement errors of 8% or lower are achievable for 2-D measurements of the EPL within spray features as small as 1 mm in the image plane, limited by spatial resolution. For features that are broader in the image plane, the percent error improves and it is possible to measure effective path length (EPL) values as low as 20 μm . The EPL is defined as the effective amount of liquid traversed by the x-ray beam along its path through the spray, including potentially non-contiguous liquid structures. A significant improvement in SNR

can be achieved by using a contrast-enhancing agent, such as potassium iodide (KI). As excessive levels of KI can induce beam hardening and potential errors in the attenuation measurement, it is possible to establish a dynamic range for EPL measurements using a single KI concentration. For a KI of 15% by mass in distilled water, this dynamic range is about 330:1 (i.e., EPL range of 15 μm to 5 mm). It is also necessary to investigate the fluid properties of any such contrast enhancing agent to ensure similar spray characteristics. Based on comparisons with the x-ray data from the APS, however, it did not appear that the contrast-enhancing agent had any significant effect on the average spray structure.

This study also revealed certain limitations on the use of broadband tube sources. For example, it would be critical to optimize the imaging resolution for measuring spray features of less than 1 mm in the imaging plane, and measurements of EPL less than 15 μm would require changes in the level of attenuation either through increased KI or the use of lower energy x-rays. As many engineering sprays have EPL values of 1 mm or less, it would be theoretically possible to increase the concentration of the contrast-enhancing agent to shift the dynamic range to a lower EPL, such as 3 μm to 1 mm, and have similar performance. A significant advantage of the broadband tube source, aside from its ready availability and portability, is that fully 2-D large-frame images of the spray can be acquired over a very short time period without raster scanning a point source. Note that the tube source and imaging system used are not completely optimized for imaging small sprays with short path lengths, and further optimization of the imaging system could lead to improved image contrast and resolution.

The narrowband synchrotron source, on the other hand, avoids several limitations described above as it is not subject to beam hardening, and its lower energy of ~ 10 keV leads

to sufficient levels of attenuation for measuring EPL of unseeded liquids (e.g., water or fuel) down to about 5 μm with excellent SNR. The use of lower photon energy in the synchrotron measurements would potentially permit even smaller values of EPL to be measured. In addition, the focus spot size of 5 μm \times 6 μm indicates that it can potentially resolve steady spatial features with cross-sections down to 10 to 12 μm in the image plane without the use of a contrast enhancing agent. Note that the configuration used and the results attained are not meant to signify a physical limit of the synchrotron-based technique. Further improvements in spatial resolution and data collection rates are possible.

With regard to 3-D measurement of mass distributions using x-ray CT imaging from a broadband tube source, the current work showed that it is possible to achieve high accuracies for spray features that are ~ 2.8 mm or larger (limited by spatial reconstruction resolution) in the image plane and for EPL values down to ~ 15 μm . The lower limit on EPL is due to interferences from background corrections required during the reconstruction. Nonetheless, this range is applicable to a wide range of spray systems in propulsion, heating, power generation, and industrial processing.

Future efforts to use x-ray tube sources should balance the need for sufficient spatial resolution, high SNR, and high dynamic range for EPL measurements. One approach is to tailor the source to the experimental needs. Several sources are available with smaller anodes and more narrowband spectra with greater flux in the lower energy range. These features can improve the spatial resolution and contrast and decrease the effects of spectral beam hardening. For conditions in which larger EPL's may be a limiting factor or higher levels of attenuation are required, the current work provides a baseline data set for validating corrections for beam hardening.

Time-resolved Measurements

Flash x-ray tube sources have been shown to afford a quantitative means of determining the time-resolved liquid mass distribution in sprays, measured using instantaneous two-dimensional radiograms and extracting the EPL distribution. The comparison with the APS data for an impinging jet spray geometry shows that quantitative mass distributions with EPL down to 50 μm are possible with proper attention paid to image processing. This includes maximizing photon flux, ensuring sufficient x-ray attenuation for low EPL, and calibrating for variations in the attenuation coefficient along the line of sight (e.g., beam hardening) at high EPL. High photon flux was achieved by removing filters used in spectral pre-hardening, while sufficient attenuation was achieved through proper selection of source spectrum and contrast-enhancing agent. The effects of spectral beam hardening and proper normalization were addressed through proper calibration and post-processing.

With these considerations, the flash x-ray radiographs captured instantaneous 2-D data, while the APS data captured the time-averaged spatial profile and the time dynamics at a single point in space. When a line plot through the spray is compared, the spatial profiles of time-averaged EPL values from the APS data agreed quite well with the single-shot flash x-ray images. The fluctuations in EPL for the two techniques, which were induced by impact waves generated during jet impingement, also agreed between the APS time-trace data and the flash x-ray spatial profile, but the spatial extent and magnitude of the fluctuations for the flash x-ray data were moderated by limited spatial resolution.

Future measurements could be enhanced using high-speed imaging to capture 2-D temporal dynamics. Careful attention must be paid to the fluid properties when using contrast enhancing agents. The spectroscopic effects of contrast enhancing agents must be determined

as well. The preferential attenuation of lower energy x-rays led to spectral beam hardening and was taken into account through calibration and spectral modeling. In future experiments, greater precision can be achieved by collecting a larger number of calibration images, and calibration should be conducted for each source and detector. Furthermore, simultaneous calibration would allow for minor changes in attenuation coefficient to be accounted for on a shot-to-shot basis (e.g., due to fluctuations in the x-ray spectrum). The normalization may also be improved by taking a large number of background images to help decrease the associated error. More accurate determination of the x-ray source spectrum would also increase the accuracy of the model and aide in the calibration and determination of the variable attenuation coefficient. The choice of source size, material, and imaging geometry should also be determined to optimize the contrast and spatial resolution based on the experimental objectives.

High-speed X-ray Imaging

The high-speed x-ray imaging experiments examined the applicability of simultaneous x-ray and visible light imaging. The x-ray radiographs imaged changes in the liquid path length and allow the quantification of time-resolved mass distribution information. The visible light system imaged changes in the shape of the spray. The visible rays refract as they pass through the liquid, and the result is an image of the shape of the spray with excellent spatial resolution. Together the complimentary techniques describe the flow behavior relying upon the strengths of each technique. Changes in path length and mass distribution can be related to changes in shape and breakup phenomena. A limitation of this

approach is the image contrast, necessitating a high mass percent of the KI contrast-enhancing agent.

In future experiments, higher resolution might be possible by optimizing the x-ray source characteristics. Higher fidelity can also be achieved by collecting a larger number of calibration images, and calibration should be conducted for each source and detector. The simultaneous calibration would allow for minor changes in attenuation coefficient to be accounted for on a shot-to-shot basis. The normalization may also be improved by taking a large number of background images to help decrease the error. The application of a rotating anode tube source with greater flux would allow for an increase in the signal-to-noise ratio, as well as imaging at a lower x-ray voltage where less KI would be needed to gain contrast.

Study of Impinging Jet Primary Breakup with Non-Newtonian Liquids

Radiographic mass distribution measurements made of Newtonian and shear-thinning non-Newtonian sprays at the Advanced Photon Source show how the behavior of the spray is greatly affected not only by the bulk viscosity but also by the local viscosity associated with shear rate. Approximations have been made to determine the change in the gel viscosity as it evolves from the jet exit to the sheet formation region. Comparisons were made with water and a high viscosity glycerol-water solution to show how the gels appear to change local viscosity over a wide range through the impingement and sheet formation process. This is expected as the shear rate would change throughout these processes.

For example, at lower shear rates induced by lower jet velocities, it was possible for the liquids with lower gel loadings to match the sheet structure of a 92% mixture of glycerol in water. This could be used to estimate that the local viscosity is similar between the gelled

liquid and the glycerol-water mixture at those conditions. As the shear rate is increased, the local viscosity of the lower and higher gel loadings seem to approach similar limiting values. This indicates that the shear thinning behavior of the liquid used in this work saturates at a certain shear rate. It is possibly for this reason that the gelled liquids did not reach the full atomized regime even at the highest jet velocities used in this work.

Future measurements would involve time-resolved measurements to understand the dynamical behavior of the gel sprays. A wider range of experimental conditions would also be beneficial to realize the role that injector geometry plays in the impingement process.

Liquid Mixing

X-ray fluorescence was employed to measure the mixing of two fluids in a like-doublet impinging jet spray. This technique is not susceptible to scatter or refraction and therefore measurements could be made anywhere in the spray independent of geometry. This is the first time measurements such as this have been made at locations prior to, during, and after impingement to see how the mixing is occurring and evolving downstream. Two methods of correcting for the reabsorption of x-ray fluorescence photons are investigated, each with advantages and disadvantages. A four-salt method was used for instantaneous corrections and to determine the mixing in both non-Newtonian and Newtonian sprays.

Reabsorption Correction Methods

X-ray fluorescence was utilized for measurements of liquid mixing in the near field of impinging jets at various stages of the merging process. Absolute calibration using x-ray attenuation measurements enabled detailed characterization of the effective path length

(EPL) profiles of each liquid jet after corrections for beam attenuation and reabsorption of fluorescent photons. Two methods to account for the reabsorption of the fluorescence signal were discussed and compared. The accuracy improved in regions with minimal reabsorption, such as in the liquid region closest to the fluorescence detector or further downstream in the liquid sheet where the liquid path length for reabsorption is reduced by spreading of the liquid sheet.

Analysis of the EPL profiles at various locations prior to and after impingement revealed significant compression of each liquid jet in the direction of jet propagation early in the merging process. This is accompanied by liquid expansion in the orthogonal direction, which is indicative of sheet formation, as expected. The liquid sheet formed by the impact of the two initially 0.51 mm individual jets is as thin as 0.38 mm combined, with individual jet profiles being as thin as ~0.30 mm and overlapped significantly within the impingement region. The amount of overlap between the individual jet fluids is what makes this measurement unique compared with prior efforts, as this has not been measured within the near-field impingement zone in prior work. Moreover, it is determined from the EPL profiles that the liquid jets cross paths and separate until finally reversing direction and merging again further downstream. These data are consistent with the occurrence of transmissive mixing, characterized by the penetration of liquid fragments from one stream into or around the other. This transmissive liquid jet mixing phenomenon agrees with previous studies of the liquid distribution well downstream of the impingement zone. The utility of the current approach is that it can be used to measure the jet profiles in the near-field impingement region, allowing the spatial and temporal mixing scales to be determined in the region where chemical reactions can begin to take place in combustion and hypergolic systems. Current efforts,

discussed further below, also analyzed changes in mixing behavior as a function of flow parameters such as impingement angle, Reynolds number, and free jet length.

These data provide key insight into the complex mixing phenomena that develops during the collision of opposed-flow jets, confirming the existence of transmissive mixing very early in the process and prior to the onset of significant droplet formation. Further examination of various conditions using this approach can, therefore, deepen the understanding of impinging jet mixing and help to validate high-fidelity numerical simulations and/or detailed physicochemical models.

Non-Newtonian (Gel) Mixing Study

Mixing measurements were made by applying the four-salt reabsorption correction method to shear thinning, non-Newtonian, viscoelastic gels comprised of 1-3% by mass HPC dissolved in water. The measurements were made using a single injector configuration while varying the velocity between moderate (18.3 m/s) and high (36.5 m/s) conditions.

Measurements were made just before and after impingement and one downstream location close to impingement zone to minimize sheet movement within the measurement volume. A 91% by mass glycerol solution was also measured as a high viscosity Newtonian analogue.

The primary conclusion from this experiment is that there is little to no variation in the mixing of the gels as the gel loading or velocity is varied for this range of jet velocities.

However there is an increase in mixing relative to the glycerol solution. This contrasts somewhat with the measurement of sheet spreading, in which it was found that the high-viscosity glycerol mixture reached the atomization regime but the gelled liquids did not.

These findings suggest that the shear rate near the impingement of the two jets is much

higher than the shear rate at the outer edge of the spreading sheet, as might be expected. Hence, while mixing is enhanced by high shear rates at the impingement point, atomization and eventual dispersion is more limited due to the difficulty of maintaining high shear rates as the liquids expand and propagate downstream. In both the mixing and sheet spreading experiments, however, the shear rate was sufficiently high that the viscosity was at or near the high shear (i.e., low viscosity) limit. At this limit the mixing and sheet spreading phenomena appear to be independent of gel loading. It should be noted that the lack of difference due to increased velocity could be due to lack of downstream measurements, where variations in shear rate lead to wider variations in the physical behavior for different gel loadings.

Future measurements would involve time-resolved measurements to extract the dynamic behavior of the fluid sheet and mixing behavior. This would require a new detection scheme; the current detector is an energy-resolved, single-photon-counting diode that is limited to speeds in the hundreds of Hz. Either a high-speed detector or multiple detectors will be required for measurements where 10's of kHz are necessary to resolve the dynamic fluid behavior.

Newtonian Liquid Mixing Parametric Study

Measurements of liquid mixing were made in an impinging jet spray while key parameters were varied, including the diameter of the jets, the angle of impingement, the free jet length, and the Reynolds number. Changing these parameters allowed for comparisons between horizontal momentum, the effect of area as the two jets meet, and the stability of the jets prior to impingement. The results were non-dimensionalized and linear multivariate

regression was used to determine trends within the data. The error in these trends is similar in magnitude to the experimental error and the assumptions made involving the effects of free jet length.

The overlap location of the two liquids, where the liquid profiles are overlapped in space, is a strong function of impingement angle and a moderate function of the free jet length. The Reynolds number has little to no effect on this overlap location, indicating that it is mostly a function of the exit trajectory of the liquid orifices. The mixing factor, or degree of overlap in the profiles of the two jet liquids, is dependent on all three spray parameters, with the largest reduction in mixing found at higher angles of impingement and greater Reynolds numbers. This indicates that the degree in which the two jet cross paths and propagate past each other is mainly dependent upon the momentum in the direction of approach. As such, the spread in the centers of mass downstream of the crossing point increases with an increase in impingement angle or Reynolds number.

Many possibilities exist for future measurements. From a diagnostics stand point, making a time resolved measurement would greatly improve the understanding of the mixing phenomena by separating jet flapping versus jet mixing effects. Although jet flapping is considered to have a minimal impact on the conclusions within the impingement zone, the precise contribution of this effect has not been quantified. Tomographic reconstruction from multiple views or point measurements using a polycapillary bundle has also been proposed to generate mixing data from two directions simultaneously, and perhaps even in three-dimensions. Finally, changing the surface tension and viscosity would allow for separating the effects of Reynolds number from Weber number, which was not investigated thoroughly in this work.

REFERENCES

- "Annual Energy Review 2011," (U.S. Energy Information Administration, 2012).
<http://www.eia.gov/totalenergy/data/annual/pdf/aer.pdf>
- Ashgriz, N., *Handbook of Atomization and Sprays*, Springer, 2011.
- Ashgriz, N., Brocklehurst, W., Talley, D., Mixing Mechanisms in a Pair of Impinging Jets.
- Baek, G., Kim, S., Han, J., Kim, C., Atomization characteristics of impinging jets of gel materials containing nanoparticles, *J. Non-Newtonian Fluid Mechanics* 166, 2011.
- Bachalo, W.D. Method for measuring the size and velocity of spheres by dual-beam light-scatter interferometry, *Appl. Optics* 19, 363-370, 1980.
- Baldwin, E., Schmidt D., Halls, B.R., Meyer, T.R., Impinging jet model and experimental validation, In Preparation.
- Balewski B, Heine B, Tropea C., Experimental investigation of the correlation between nozzle flow and spray using laser Doppler velocimeter, phase Doppler system, high-speed photography, and radiography *Atomization Sprays*, 20(1), 57–70, 2012.
- Barrett, H.H., Swindell, W., 1981. Radiological Imaging: The Theory of Image Formation, Detection, and Processing. Academic Press, New York.
- Beckhoff, B., B. Kanngiesser, N. Langhoff, R. Wedell, and H. Wolff, *Handbook of Practical x-ray Fluorescence Analysis*. Springer, Berlin, 2006.
- Berrocal, E., Kristensson, E., Richter, M., Linne, M., Aldén, M., *Optics Express* 16(22), 2008.
- Birk, A., McQuaid, M., Gross, M., "Liquid core structure of evaporating sprays at high pressures – Flash X-ray Studies", ARL-TR-901 2003.

- Cai, W., Powell, C.F., Yue, Y., Narayanan, S., Wang, J., Tate, M.W., Renzi, M.J., Ercan, A., Fontes, E., and Gruner, S.M., Quantitative analysis of highly transient fuel sprays by time-resolved x-radiography, *Appl. Phys. Letters* 83(8), 1671-1673, 2003.
- Campbell, D.T., Clapp, S.D., Profitt, R.L., Cline, G.L., Reactive stream separation, *AIAA J.* 9(9), 1971.
- Char, J.M., Kuo, K.K., Hsieh, K.C., Observations of Breakup Processes of Liquid Jets Using Real-Time X-ray Radiography, *J. Propulsion* 6(5) 544-551, 1989.
- Charalampous, G., Hardalupas, Y., Taylor, A., Novel Technique for Measurements of Continuous Liquid Jet Core in an Atomizer, *AIAA J.* 47(11), 2605-2315, 2009.
- Chen, X., Yang, V., Numerical simulation of primary atomization of non-Newtonian impinging jets, 25th *ILASS*, 2011.
- Chen, X., Ma, D., Yang, V., Mechanism study of impact wave in impinging jet atomization, 50th *AIAA ASM*, 2012.
- Choo, Y.J., Kang, B.S., Parametric study on impinging-jet liquid sheet thickness distribution using an interferometric method, *Exp. Fluids* 31, 2001.
- Coil, M.A., Effect of Viscoelastic Properties in Impinging Jet Sprays, 11th *ICLASS*, 2009.
- Coil, M.A., Hypergolic Ignition of a Gelled Ionic Liquid Fuel, *AIAA JPC*, 2010.
- Coletti, F., Benson, M.J., Sagues, A.L., Miller, B.H., Fahrig, R., Eaton, J.K., Three-dimensional mass fraction distribution of a spray measured by x-ray computed tomography, *J. Engineering for Gas Turbine and Power* 136, 2014.
- Dennis, J.D., Pourpoint, T.L., Son, S.F., Ignition of gelled monomethylhydrazine and red fuming nitric acid in an impinging jet apparatus, 47th *AIAA JPC*, 2011.

- Dobbins, R. A., Crocco, L., and Glassman, I., Measurement of mean particle sizes of sprays from diffractively scattered light, *AIAA J.*, 1(8) 1882–1886, 1963.
- Dombrowski, N., Hooper, P.C., A Study of the Sprays Formed by Impinging Jets in Laminar and Turbulent Flow, *J. Fluid Mechanics*, 18(3), 392-400, 1964.
- Elverum, G. W., Jr., and Morey, T. F., Criteria for Optimum Mixture-Ratio Distribution Using Several Types of Impinging-Stream Injector Elements, Jet Propulsion Lab., Memorandum 30-5, 1959.
- Eng, P.J., Newville, M., Rivers, M.L., Sutton, S.R., Dynamically figured Kirkpatrick Baez x-ray micro-focusing optics, *P. Soc. Photo-Opt Ins.*, 3449, no. 145, 145-156, 1998.
- Epstein, A.H., "Aircraft engines' needs from combustion science and engineering," *Combustion and Flame* 159, 1791–1792 2012.
- Feikema, D.A., Smith, J.E., Combustion and flow visualization of hypergolic combustion and gelled mixing behavior, ARO-TR, 1997.
- Fukui, N., Sato, T., The study of liquid atomization by the impingement of two jets, *Japanese Society of Mechanical Engineers* 15(83) 1972.
- Halls, B.R., Heindel, T.J., Kastengren, A.L., Meyer, T.R., "Evaluation of X-ray sources for quantitative two- and three-dimensional imaging of liquid mass distribution in atomizing sprays," *Int. J. Multiphase Flow* 59, 2014.
- Halls, B.R., Heindel, T.J., Meyer, T.R., High-Speed Simultaneous Tube Source Radiography and Visible Light Spray Imaging, ILASS Americas 2014, 2014.
- Halls, B.R., Meyer, T.R., A. L. Kastengren, X-ray Fluorescence Measurement of Mixing in Impinging Jets, 26th ILASS Americas, 2014.

- Halls, B.R., Heindel, T.J., Meyer, T.R., Kastengren, A.L., X-ray spray diagnostics: comparing sources and techniques, 50th AIAA ASM, January 2012.
- Halls, B.R., Heindel, T.J., Meyer, T.R., Lightfoot, M.D., Danczyk, S.A., Schumaker, S.A., Roy, S., Gord, J.R., A. L. Kastengren, Quantitative X-ray imaging of liquid mass distribution in optically dense sprays, 25th ILASS-Americas, 2013.
- Halls, B.R., Meyer, T.R., A.L. Kastengren, “Quantitative measurement of binary liquid distributions using multiple-tracer x-ray fluorescence and radiography,” Submitted to Optics Express, 2014.
- Halls, B.R., Morgan, T.B., Heindel, T.J., Meyer, T.R., High-speed radiographic X-ray spray imaging with broadband tube source, 52nd AIAA ASM, January 2014.
- Halls, B.R., Radke, C.D., Heindel, T.J., Lohry, W.F., Zhang, S., Kastengren, A.L., Meyer, T.R., Evaluation of advanced diagnostics for visualization of dense spray breakup processes, Spring Technical Meeting Central States Section of the Combustion Institute, April 2012.
- Halls, B.R., Radke, C.D., Heindel, T.J., Lohry, W.F., Zhang, S., Meyer, T.R., Lightfoot, M.D., Danczyk, S.A., Schumaker, S.A., Roy, S., Gord, J.R., Kastengren, A.L., Characterization of three-dimensional dense spray visualization techniques, 51st AIAA ASM, January 2013.
- Hasson, D., Peck, R.E., Thickness distribution in a sheet formed by impinging jets, *A.I.Ch.E. Journal* 10(5) 1964.
- Heidmann, M.F., Humphrey, J.C., Fluctuations in a spray formed by two impinging jets, NACA-TN-2349, 1951.

- Heidmann, M.F., Priem, R.J., Humphrey, J.C., A study of sprays formed by two impinging jets, NACA-TN-3835, 1957.
- Heindel, T.J., A review of X-ray flow visualization with applications to multiphase flows, *J. Fluids Engineering – Transactions of the ASME*, 133(7), 2011.
- Heindel, T.J., Gray, J.N., and Jensen, T.C., *Flow Measurement and Instrumentation* 19, 67-78, 2008.
- Heindel, T.J., Hubers, J.L., Jensen, T.C., Gray, J.N., and Striegel, A.C., *Proc. 2005 ASME Fluids Engineering Division Summer Meeting and Exhibition*, June, 2005.
- Heindel, T.J., Jensen, T.C., and Gray, J.N., “Visualizing fluid flows with X-rays,” *Proceedings of FEDSM2007: 5th Joint ASME/JSME Fluids Engineering Conference*, July – August, 2007.
- Hoehn, J.W., Rupe, J.H., Sotter, J.G., Liquid-Phase Mixing of Bipropellant Doublets, NACA-TR-32-1546, 1972.
- Houseman, J., Combustion effects in sprays, JPL-TN, 1968.
- Houseman, J., Optimum mixing of hypergolic propellants in an unlike doublet injector element, JPL-TN, 1970.
- Hsieh, J., 2003. Computed Tomography: Principles, Design, Artifacts, and Recent Advances. SPIE Press, Bellingham, WA.
- Hubbell, J.H. and Seltzer, S.M., Tables of X-Ray Mass Attenuation Coefficients and Mass Energy-Absorption Coefficients (version 1.4). [Online] Available: <http://physics.nist.gov/xaamdi> [2013, 02 20]. NIST, Gaithersburg, MD (2004).

- Jung, K., Koh, H., Yoon, Y., Assessment of planar liquid-laser-induced fluorescence measurements for spray mass distributions of like-doublet injectors, *Meas. Sci. Technol.*, 14(8), 1387-1395, 2003.
- Kampen, J., Alberio, F., Ciezki, H.K., Spray and combustion characteristics of aluminized gelled fuels with an impinging jet injector, *Aerospace Science and Technology* 11, 2007.
- Kastengren, A. L., Powell, C.F., Spray density measurements using X-ray radiography, *Proceedings of IMechE Part D: J. Automobile Engineering*, 221, 653-662, 2007.
- Kastengren, A., Powell, C. F., Dufresne, E. M. & Walko, D. A. Application of X-ray fluorescence to turbulent mixing, *J. Synchrotron Rad.* 18, 811-815, 2011.
- Kastengren, A. L., Powell, C.F., Arms, D., Dufresne, E. M., Gibson, H., Wang, J., The 7BM beamline at the APS: a facility for time-resolved fluid dynamics measurements, *J. Synchrotron Radiation*, 19(4) 654-657, 2012.
- KODAK INDUSTREX Digital Imaging Plates. [Retrieved 2013, 02, 20 from http://www.kodak.com/eknec/documents/80/0900688a805e0880/EN_ti2632.pdf], 2006.
- Kramers, H.A., On the theory of X-ray absorption and the continuous X-ray spectrum. *Philos. Mag.* 46, 836 1923.
- Kristensson, E., Berrocal, E., Alden, M., *Quantitative 3D imaging of scattering media using structured illumination and computed tomography*, *Opt. Express* 20, 14437-14450, 2012.
- Lawver, B. R., An Experimental Study of the N₂O₄ / N₂H₄ Jet Separation Phenomena, Final Report, Dynamic Science NASA-CR-72444, 1968.
- Lefebvre, A., *Atomization and Sprays*, Hemisphere Publishing Corp, New York 1989.
- Li, R., and Ashgriz, N., Characteristics of liquid sheets formed by two impinging jets, *Phys. Fluids* 18, 2006.

- Lightfoot, M.D., Kastengren, S.A., Schumaker, A.L., Danczyk, Powell, C.F., Spray Statistics and the Impact of Geometry in Gas-Centered Swirl Coaxial Injectors, *24th ILASS-Americas*, 2012.
- Lim, J., Sivathanu, Y., Wolverton, M., Evaluation of Soft X-Ray Absorption Tomography for the Near Injector Characterization of Dense Sprays, *25th ILASS-Americas*, 2013.
- Lin, K.-C., Kennedy, P.J., Jackson, T.A., Spray structures of aerated-liquid jets in subsonic crossflows, *AIAA 2001-0330*, 2001.
- Lin, K-C., Rajnicek, C., McCall, J., Carter, C., Fezzaa, K., Investigation of pure- and aerated-liquid jets using ultra-fast X-ray phase contrast imaging, *Nucl. Instrum. Methods in Phys. Res. A*, 649(1) 194-496, 2011.
- Lin, K. C., Ryan, M., Carter, C., Sandy, A., Narayanan, S., Ilavsky, J., & Wang, J. Investigation of droplet properties of supercritical ethylene jets using Small Angle X-ray Scattering (SAXS) Technique. *21st ILASS-Americas*, 2008.
- Linne, M.A., Paciaroni, M., Gord, J.R., Meyer, T.R., Ballistic imaging of the liquid core for a steady jet in crossflow, *Appl. Optics*, 44(31) 6627-6634, 2005.
- Linne, M. A., Imaging in the Optically Dense Regions of a Spray: A Review of Developing Techniques, *Progress in Energy and Combustion Science*, 39(5) 403-440, 2013.
- Mallory, J.A., Sojka, P.E., Jet Impingement and Primary Atomization of Non-Newtonian Liquids, Thesis, 2012
- McDonnell, V., Phi, V., Samuelsen, S. Shahnab, M., Nejad, A., Carlson, R.A., Guernsey, Structure of Sprays Generated by Unlike Doublet Injectors, *AIAA, JPC*, June, 1999.
- Meyer, T. R., Brear, M., Jin, S. H., Gord, J. R., *Formation and Diagnostics of Sprays in Combustion*, Handbook of Combustion, Wiley, New York, 291–322, 2010.

- Meyer, T.R., Schmidt, J.B., Nelson, S.M., Drake, J.B., Janvrin D.M. Heindel, T.J., 21st *ILASS-Americas*, 2008.
- Miller, K.D., Distribution of sprays from impinging liquid jets, *J. App. Phys.* 31, 1960.
- Negri, M., Ciezki, H.K., Schleichtrien, S., Spray behavior of non-Newtonian fluids: Correlation between rheological measurements and droplets/threads formation. *Prog. Propulsion Phys.* 4, 2013.
- Nurick, W.H., Orifice cavitation and its effect on spray mixing, *J. Fluids Engineering*, Dec, (1976).
- Nurick, W.H., and Clapp, S.D., An experimental technique for measurement of injector spray mixing, *J. Spacecraft*, 6(11), 1969.
- Poola, R., Powell, C.F., Yue, Y., Gupta, S., McPherson, A., and Wang, J., Development of a quantitative measurement of a diesel spray core using synchrotron X-rays, 8th *ICLASS*, 2000.
- Powell, C.F., Yue, Y., Poola, R., and Wang, J., Time-resolved measurements of supersonic fuel sprays using synchrotron X-rays, *J. Synchrotron Radiation (Fast Communications)*, 7(6) 356-360, 2000.
- Qun, S., Lee, W-K., Fezzaa, K., Chu, Y.S., De Carlo, F., Jemian, P., Ilavsky, J., Erdman, M., and Long, G., Dedicated full-field X-ray imaging beamline at Advanced Photon Source, *NIM A*, 582(1), 77-79, 2007.
- Robert, E., Dozias, S., Vildarosa, R., Cachoncinlle, C., Pouvesle, J.M., Table-top flash X-ray diagnostics of dodecane sprays, *23rd ILASS-Europe*, 2010.
- Ruff, G.A., Sagar, A.D., Faeth, G.M., Structure and Mixing Properties of Pressure-atomized sprays, *J. AIAA* 27(7) 901-908, 1989.

- Rupe, J. H., The Liquid-Phase Mixing of a Pair of Impinging Streams, Jet Propulsion Lab. Progress Rept. 20-195, 1953.
- Rupe, J. H., "A Correlation Between the Dynamic Properties of a Pair of Impinging Streams and the Uniformity of Mixture-Ratio Distribution in the Resulting Spray," Jet Propulsion Lab., Progress Rept. 20-209, 1956.
- Sallam, K.A., Aalburg, C., Faeth, G.M., Lin, K.C., Carter, C.D., Jackson, T.A., Primary breakup of round aerated-liquid jets in supersonic crossflows, *Atomization Sprays*, 16(6) 657-672, 2006.
- Santangelo, P.J., Sojka, P.E., Focused-image holography as a dense-spray diagnostic, *Appl. Optics*, 33(19) 4132-4136, 1994.
- Schumaker, S.A., Kastengren, A.L., Lightfoot, M.D.A., Danczyk, S.A., and Powell, C.F., A study of gas-centered swirl coaxial injectors using X-ray radiography, *12th ICLASS*, 2012.
- Settles, G. *Schlieren and shadowgraph techniques*. Berlin: Springer; 2001.
- Sick, V., Stojkovic, B., Attenuation effects on imaging diagnostics of hollow-cone sprays, *Appl. Optics*, 40(15) 2435-2442, 2001.
- Somogyi, D., Feiler, C.E., Study of the mixture-ratio distribution in the drops of sprays produced by impinging liquid streams, NASA, 1959.
- Sutton, G.P., Biblarz, O., *Rocket Propulsion Elements*, Wiley-Interscience, 2001.
- Taylor, G.I., The Spectrum of Turbulence, *Proc. R. Soc. Lond. A*, 164, 476-490, 1938.
- Thompson, A.C., Kirz, J., Attwood, D.T., Gullikson, E.M., Howells, M.R., Kortright, J.B., Liu, Y., Robinson, A.L., Underwood, J.H., Kim, K-J., Lindau, I., Pianetta, P., Winick, H., Williams, G.P., Scofield, J.H., *X-ray Data Booklet*, Lawrence Berkeley National Lab, 2009.

- Yang, L., Fu, Q., Qu, Y., Gu, B., Zhang, M., Breakup of a power-law liquid sheet formed by an impinging jet injector, *I. J. Multiphase Flow* 39, 2012.
- Yang, V., Habiballah, M., Hulka, J., Popp, M., *Liquid Rocket Thrust Chambers: Aspects of Modeling, Analysis, and Design*, AIAA Inc., 2004.
- Yang, V., Anderson, W., *Liquid Rocket Engine Combustion Instability*, AIAA Inc., 1995.
- Yuan, T. Huang, B., Optical Analysis of the Mixing effect in fully Developed Like-Doublet Impinging Jet Sprays, *Atomization and Sprays*, 22(5), 391-408 2012.
- Walko, D. A., Arms, D. A., Miceli, A. & Kastengren, A. Empirical dead-time corrections for energy-resolving detectors at synchrotron sources. *Nucl. Instrum. Methods Phys. Res. A*, 649(1), 81-83, 2010.
- Woodward, R.D, Pal, S., Santoro, R.J., Kuo, K.K., Recent advances in spray combustion: spray atomization and drop burning phenomena, *AIAA Inc.*, 185-210, 1995.

APPENDIX A

LIQUID MIXING STUDY

The liquid mixing study table contains the relevant parameters and results from the Newtonian mixing study. The table includes the spray input parameters; the condition number, the injector orifice diameter in millimeters, the included impingement angle, the length of the free jet in diameters, the velocity in meters per second, and the nondimensional numbers the Reynolds number and the Weber number. The experiments and analysis were Reynolds number based, the Weber number has been include for completeness. The products of the nondimensional numbers are also included to compare with the regression coefficients to determine the effect of each parameter on the output of the empirical equations. The quantities determined from the measurements are also tabulated that include the length from the injector to the theoretical jet crossing point (0 mm location), the location of liquid profile overlap relative to the theoretical crossing location in diameters, the minimum value of the mixing factor Φ and its location in diameters relative to the theoretical crossing location, and the maximum spread in the centers of mass of each liquid profile and the location of this occurrence in diameters relative to the theoretical crossing location.

Table A. Results from the water mixing study.

Condition		1	2	3	4	5	6	7	8
Diameter	[mm]	0.508	0.508	0.508	0.508	0.508	0.508	0.508	0.508
Angle	[deg]	45	45	45	45	45	45	60	60
Free Jet	[d]	14.8	14.8	14.8	14.8	14.8	14.8	5.9	10.3
Velocity	[m/s]	4.56	6.08	9.12	12.16	18.24	23.71	13.68	13.68
Re	[-]	2340	3120	4680	6240	9360	12166	7020	7020
We	[-]	147	261	587	1044	2348	3968	1321	1321
$\sin\theta * FJ$	[-]	5.65	5.65	5.65	5.65	5.65	5.65	2.95	5.17
$\sin\theta * Re$	[-]	895	1194	1791	2388	3582	4656	3510	3510
$FJ * Re$	[-]	34545	46061	69091	92121	138182	179621	41455	72545
L_ext	[d]	13.6	13.6	13.6	13.6	13.6	13.6	5.1	9.0
L_overlap	[d]	2.95	2.95	2.80	2.80	2.95	2.95	1.33	1.89
PHI min	[%]	93.6	88.2	84.4	84.2	82	83.1	80.6	81.2
L_phi	[d]	6.9	6.9	6.9	6.9	10.8	10.8	7.4	9.4
CoM max	[d]	0.04	0.16	0.04	0.28	0.47	0.57	0.41	0.53
L com	[d]	4.9	10.8	4.9	16.7	16.7	22.6	7.4	9.4
Condition		9	10	11	12	13	14	15	16
Diameter	[mm]	0.508	0.508	0.508	0.508	0.508	0.508	0.508	0.508
Angle	[deg]	60	60	60	60	60	60	60	60
Free Jet	[d]	12.8	12.8	12.8	12.8	12.8	12.8	18.7	22.1
Velocity	[m/s]	4.56	6.08	9.12	13.68	18.24	22.8	13.68	13.68
Re		2340	3120	4680	7020	9360	11699	7020	7020
We		147	261	587	1321	2348	3669	1321	1321
$\sin\theta * FJ$		6.40	6.40	6.40	6.40	6.40	6.40	9.35	11.07
$\sin\theta * Re$		1170	1560	2340	3510	4680	5850	3510	3510
$FJ * Re$		29939	39919	59879	89818	119758	149697	131273	155455
L_ext	[d]	11.1	11.1	11.1	11.1	11.1	11.1	16.2	19.2
L_overlap	[d]	1.60	1.53	1.67	1.70	1.86	1.70	2.03	1.41
PHI min	[%]	86.7	83.9	80.5	79.3	79.8	78.5	79.8	78.8
L_phi	[d]	5.9	5.9	5.9	5.9	9.8	9.8	8.6	5.4
CoM max	[d]	0.37	0.26	0.43	0.63	0.75	1.32	0.59	0.73
L com	[d]	13.8	5.9	9.8	13.8	13.8	19.7	8.9	11.3

Table A. Results from the water mixing study, continued.

Condition		17	18	19	20	21	22	23	24
Diameter	[mm]	0.508	0.508	0.508	0.508	0.508	0.508	0.508	0.508
Angle	[deg]	60	60	60	60	60	60	90	90
Free Jet	[d]	27.1	27.1	27.1	27.1	27.1	27.1	11.3	11.3
Velocity	[m/s]	4.56	6.08	9.12	13.68	18.24	22.8	4.56	6.08
Re		2340	3120	4680	7020	9360	11699	2340	3120
We		147	261	587	1321	2348	3669	147	261
sin θ * FJ		13.53	13.53	13.53	13.53	13.53	13.53	8.00	8.00
sin θ * Re		1170	1560	2340	3510	4680	5850	1655	2206
FJ Re		63333	84444	126667	190000	253333	316667	26485	35313
L_ext	[d]	23.4	23.4	23.4	23.4	23.4	23.4	8.0	8.0
L_overlap	[d]	2.46	1.28	1.28	1.28	1.33	1.34	1.45	1.02
PHI min	[%]	92.7	82.9	78.4	79.5		80.1	90.7	83.2
L_phi	[d]	7.4	7.4	7.4	7.4		7.4	3.4	3.4
CoM max	[d]	0.10	0.45	0.81	0.73	1.02	1.28	0.14	0.69
L com	[d]	7.4						3.5	9.4
Condition		25	26	27	28	29	30	31	32
Diameter	[mm]	0.508	0.508	0.508	0.508	1.016	1.016	1.016	1.016
Angle	[deg]	90	90	90	90	60	60	60	60
Free Jet	[d]	11.3	11.3	11.3	11.3	11.8	11.8	11.8	11.8
Velocity	[m/s]	9.12	12.16	18.24	22.8	3.04	4.56	6.08	9.12
Re		4680	6240	9360	11699	3120	4680	6240	9360
We		587	1044	2348	3669	130	294	522	1174
sin θ * FJ		8.00	8.00	8.00	8.00	5.91	5.91	5.91	5.91
sin θ * Re		3309	4412	6618	8273	1560	2340	3120	4680
FJ Re		52970	70626	105939	132424	36848	55273	73697	110545
L_ext	[d]	8.0	8.0	8.0	8.0	10.2	10.2	10.2	10.2
L_overlap	[d]	0.59	0.49	0.58	0.58	3.20	1.35	1.34	1.19
PHI min	[%]	77.5	74.4	75.4	75.8		87.2	84.6	80.3
L_phi	[d]	5.4	5.4	5.4	5.4		2.5	5.4	5.4
CoM max	[d]	1.52	2.85	2.70	3.01		0.16	0.23	0.41
L com	[d]	13.3	17.2	17.2			5.4	5.4	5.4

The graphical results from the Newtonian mixing study are presented below. The results include a set of plots describing the mixing behavior of each measured condition. From these data the results are tabulated found in Table A1. Line plot (a) on the left is tracking the center of mass of each liquid as it progresses downstream. This plot displays both the location of overlap, and the location and maximum spread between the two centers of mass. Each fluid is designated by its fluorescent salt tracer, Zn or Cu. Displayed in line plot (b) is the progression of the mixing factor. Line plot (c) shows the FWHM of the full spray, describing the thickness of the sheet and droplet cloud distribution; this is not to be confused with the EPL values previously mentioned.

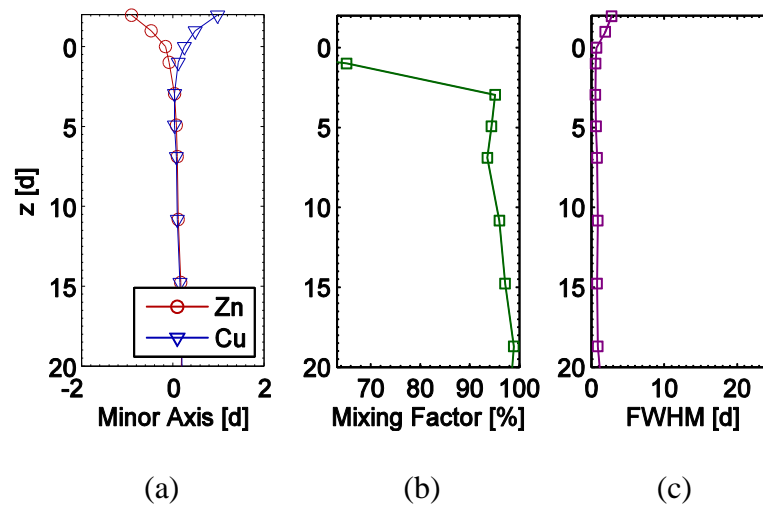


Figure A2-1. Condition 1, orifice diameter of 0.5 mm, impingement angle of 45 degrees, free jet length of 15 diameters, Reynolds number of 2300, and Weber number of 150.

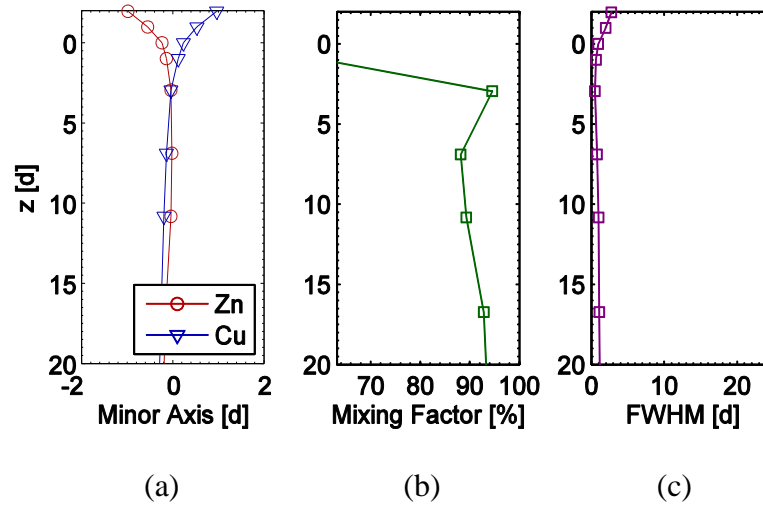


Figure A2-2. Condition 2, orifice diameter of 0.5 mm, impingement angle of 45 degrees, free jet length of 15 diameters, Reynolds number of 3000, and Weber number of 260.

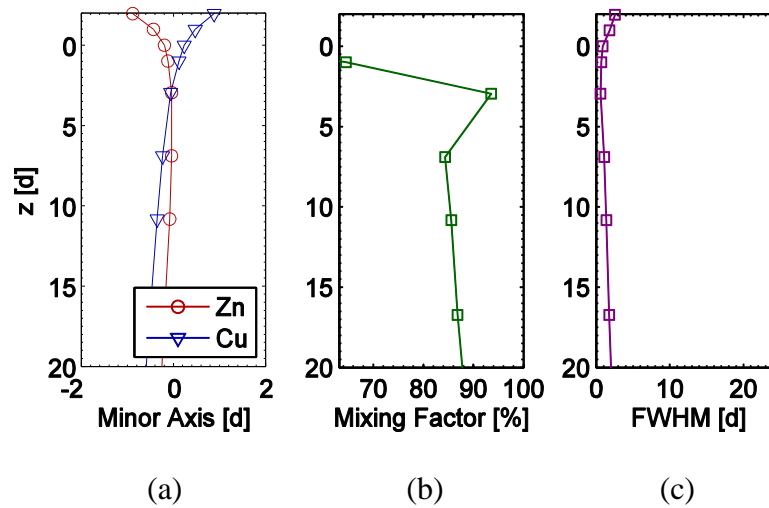


Figure A2-3. Condition 3, orifice diameter of 0.5 mm, impingement angle of 45 degrees, free jet length of 15 diameters, Reynolds number of 4700, and Weber number of 590.

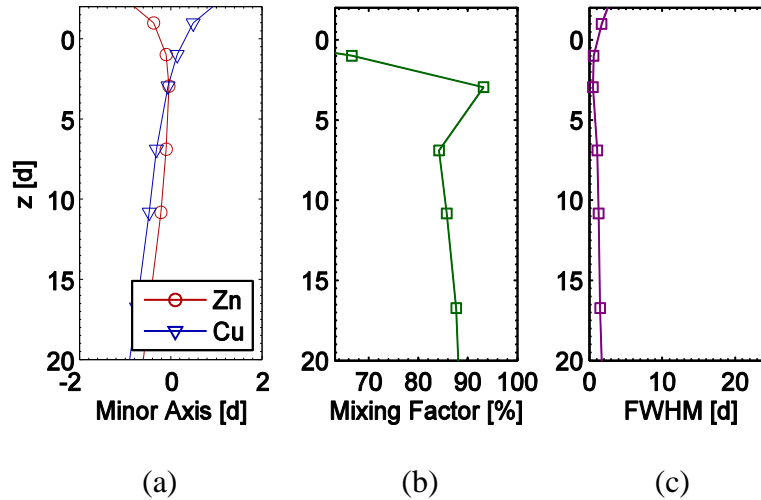


Figure A2-4. Condition 4, orifice diameter of 0.5 mm, impingement angle of 45 degrees, free jet length of 15 diameters, Reynolds number of 6200, and Weber number of 1000.

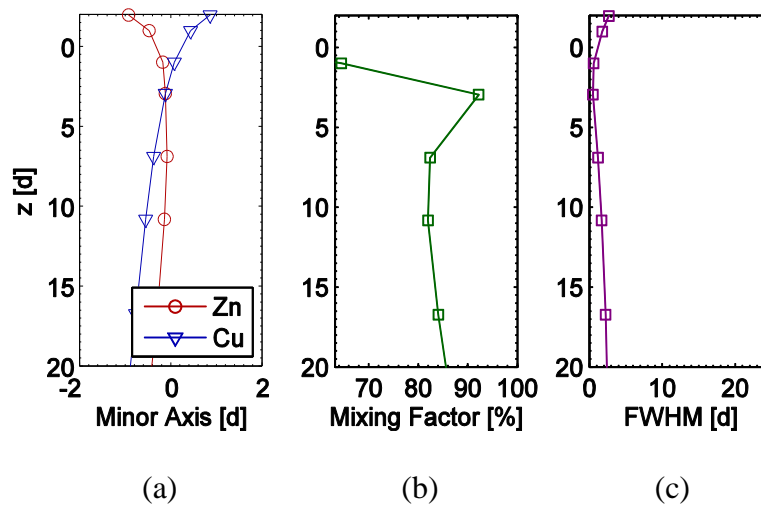


Figure A2-5. Condition 05, orifice diameter of 0.5 mm, impingement angle of 45 degrees, free jet length of 15 diameters, Reynolds number of 9400, and Weber number of 2300.

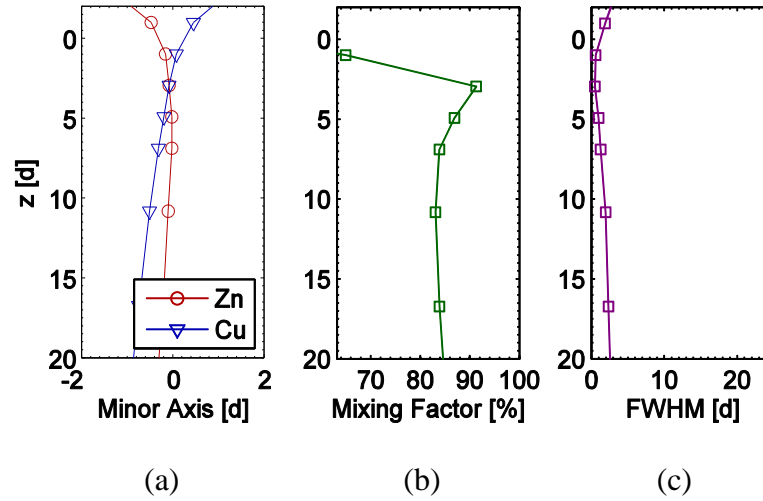


Figure A2-6. Condition 6, orifice diameter of 0.5 mm, impingement angle of 45 degrees, free jet length of 15 diameters, Reynolds number of 12200, and Weber number of 4000.

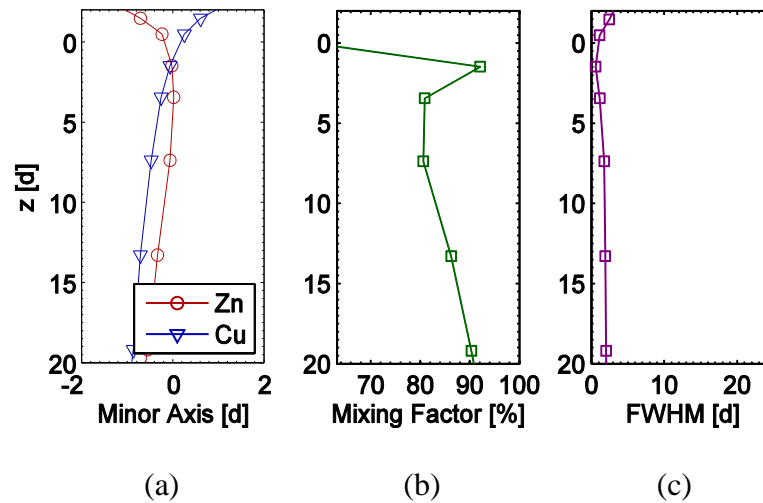


Figure A2-7. Condition 7, orifice diameter of 0.5 mm, impingement angle of 60 degrees, free jet length of 6 diameters, Reynolds number of 7000, and Weber number of 1300.

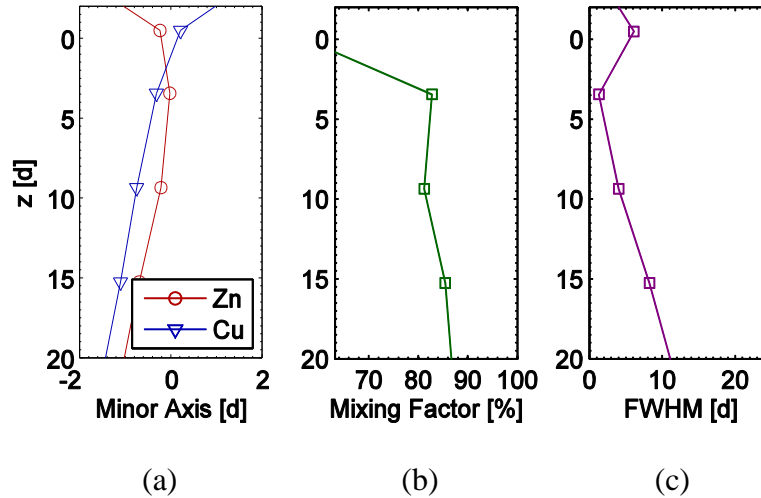


Figure A2-8. Condition 8, orifice diameter of 0.5 mm, impingement angle of 60 degrees, free jet length of 10 diameters, Reynolds number of 7000, and Weber number of 1300.

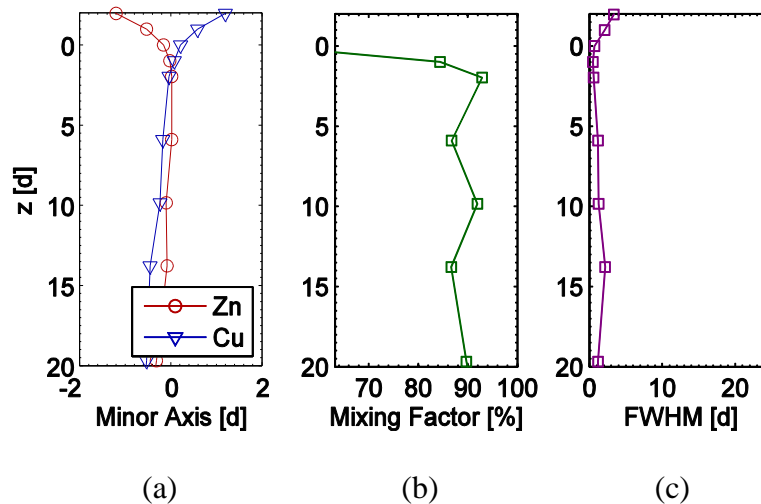


Figure A2-9. Condition 9, orifice diameter of 0.5 mm, impingement angle of 60 degrees, free jet length of 13 diameters, Reynolds number of 2400, and Weber number of 150.

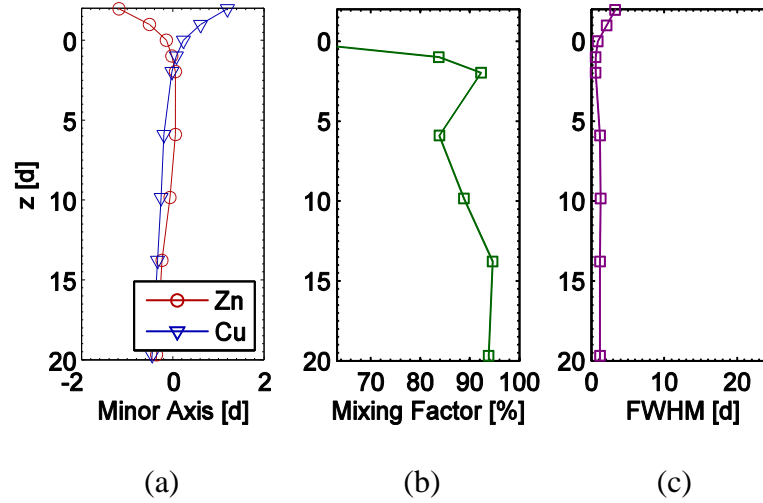


Figure A2-10. Condition 10, orifice diameter of 0.5 mm, impingement angle of 60 degrees, free jet length of 13 diameters, Reynolds number of 3100, and Weber number of 260.

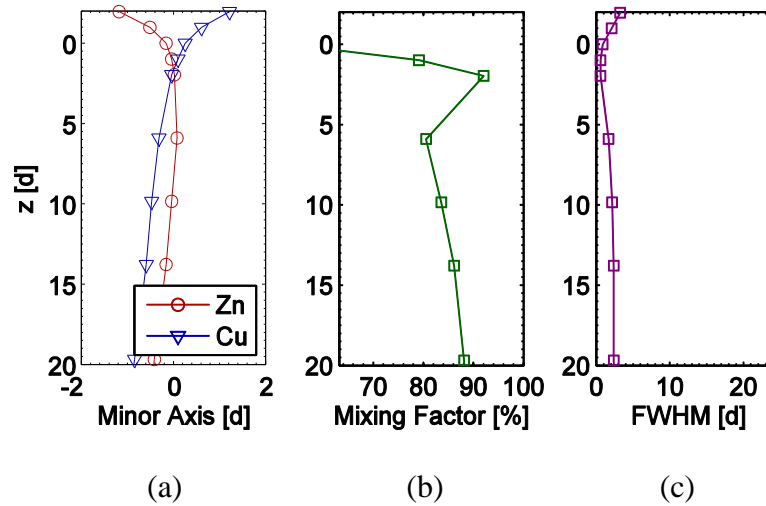


Figure A2-11. Condition 11, orifice diameter of 0.5 mm, impingement angle of 60 degrees, free jet length of 13 diameters, Reynolds number of 4700, and Weber number of 590.

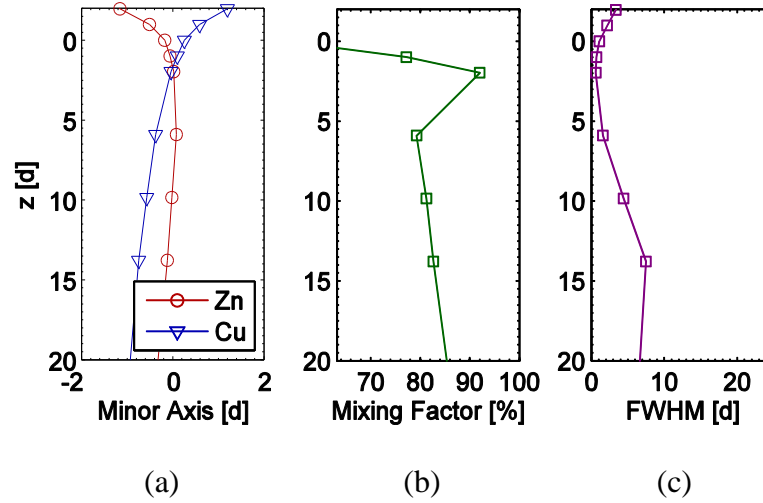


Figure A2-12. Condition 12, orifice diameter of 0.5 mm, impingement angle of 60 degrees, free jet length of 13 diameters, Reynolds number of 7000, and Weber number of 1300.

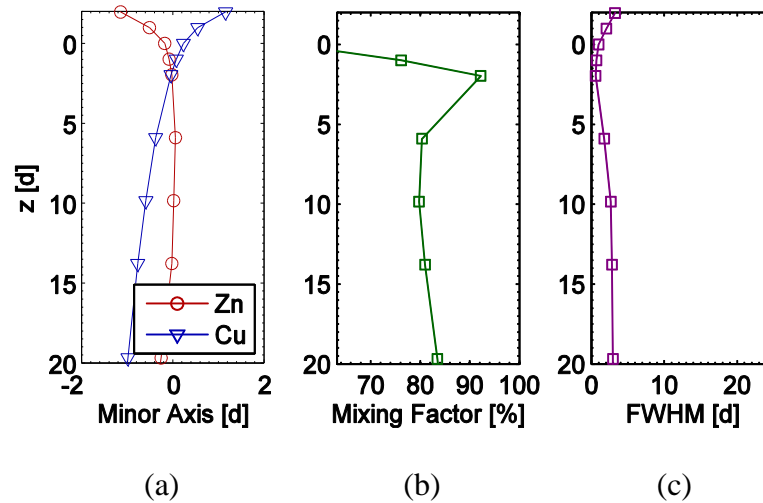


Figure A2-13. Condition 13, orifice diameter of 0.5 mm, impingement angle of 60 degrees, free jet length of 13 diameters, Reynolds number of 9400, and Weber number of 2300.

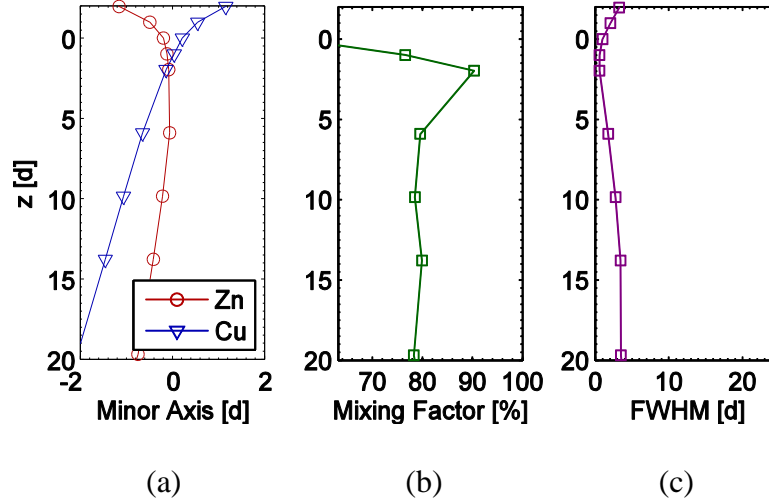


Figure A2-14. Condition 14, orifice diameter of 0.5 mm, impingement angle of 60 degrees, free jet length of 13 diameters, Reynolds number of 11700, and Weber number of 3700.

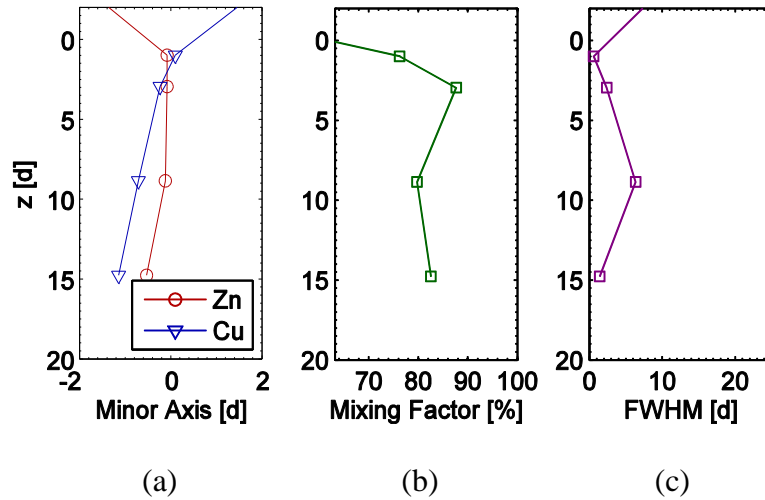


Figure A2-15. Condition 15, orifice diameter of 0.5 mm, impingement angle of 60 degrees, free jet length of 19 diameters, Reynolds number of 7000, and Weber number of 1300.

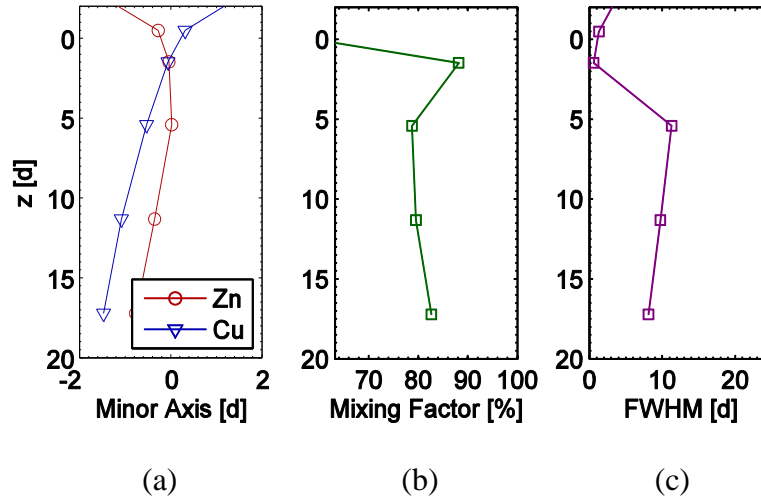


Figure A2-16. Condition 16, orifice diameter of 0.5 mm, impingement angle of 60 degrees, free jet length of 22 diameters, Reynolds number of 7000, and Weber number of 1300.

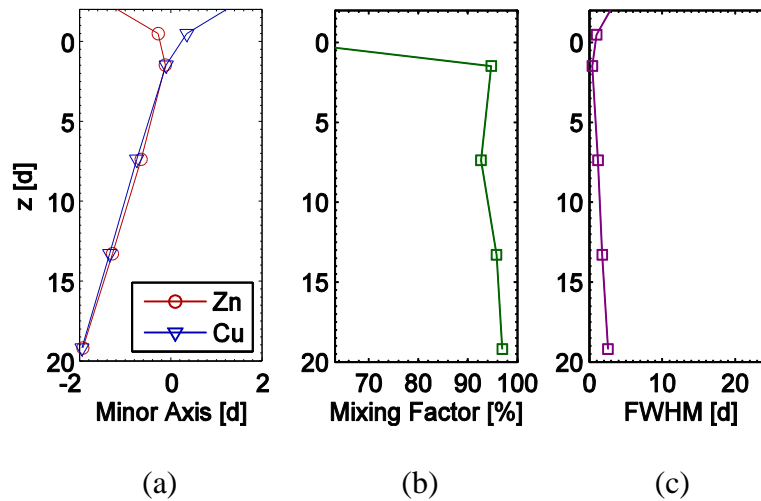


Figure A2-17. Condition 17, orifice diameter of 0.5 mm, impingement angle of 60 degrees, free jet length of 27 diameters, Reynolds number of 2300, and Weber number of 150.

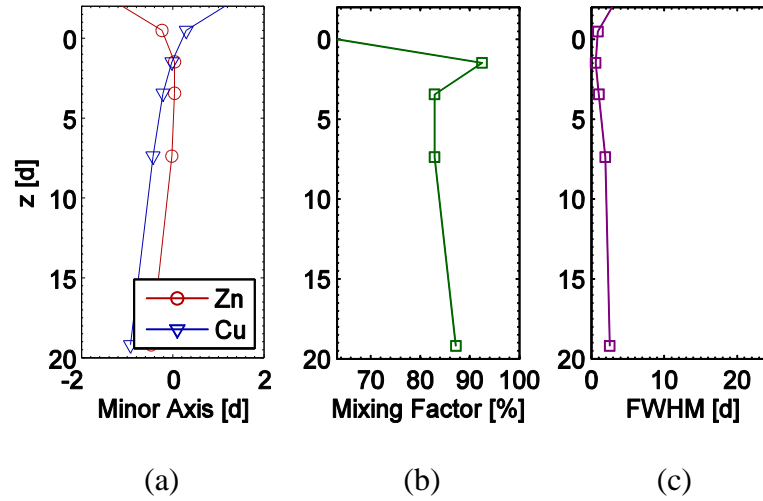


Figure A2-18. Condition 18, orifice diameter of 0.5 mm, impingement angle of 60 degrees, free jet length of 27 diameters, Reynolds number of 3100, and Weber number of 260.

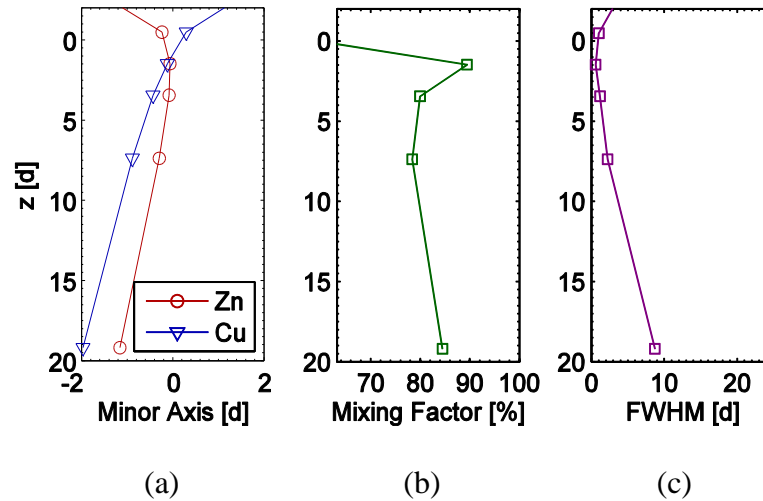


Figure A2-19. Condition 19, orifice diameter of 0.5 mm, impingement angle of 60 degrees, free jet length of 27 diameters, Reynolds number of 4700, and Weber number of 590.

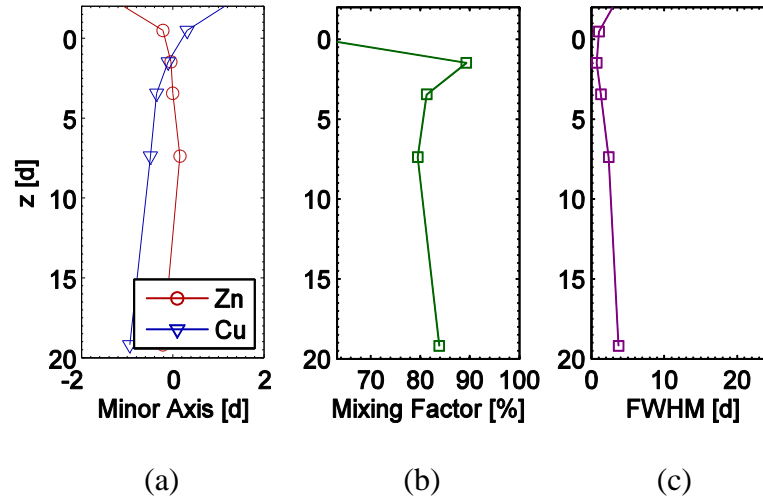


Figure A2-20. Condition 20, orifice diameter of 0.5 mm, impingement angle of 60 degrees, free jet length of 27 diameters, Reynolds number of 7000, and Weber number of 1300.

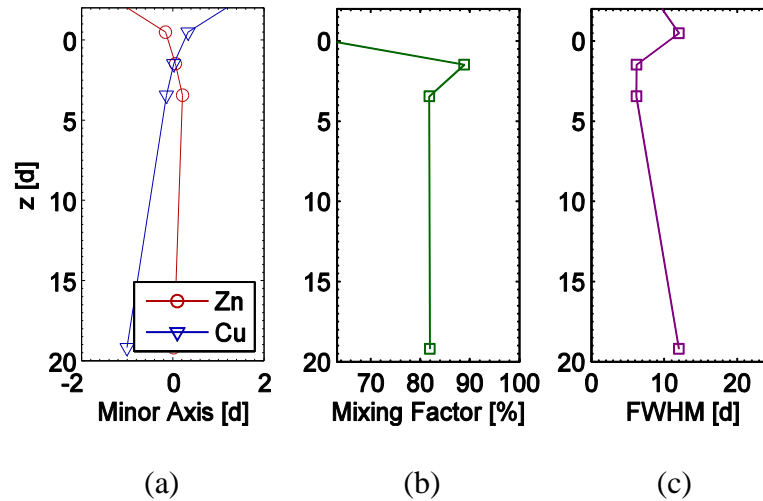


Figure A2-21. Condition 21, orifice diameter of 0.5 mm, impingement angle of 60 degrees, free jet length of 27 diameters, Reynolds number of 9400, and Weber number of 2300.

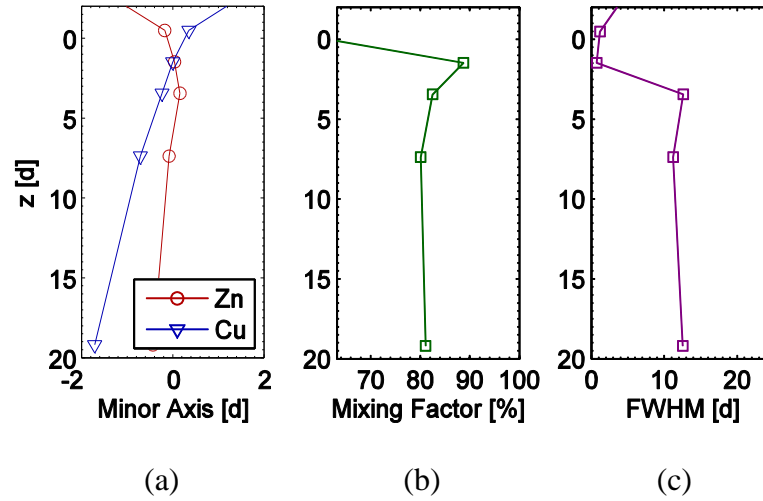


Figure A2-22. Condition 22, orifice diameter of 0.5 mm, impingement angle of 60 degrees, free jet length of 27 diameters, Reynolds number of 11700, and Weber number of 3700.

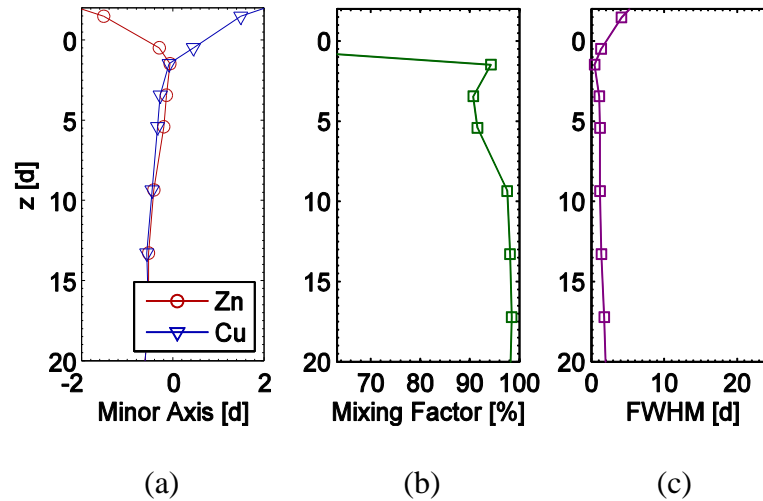


Figure A2-23. Condition 23, orifice diameter of 0.5 mm, impingement angle of 90 degrees, free jet length of 11 diameters, Reynolds number of 2300, and Weber number of 150.

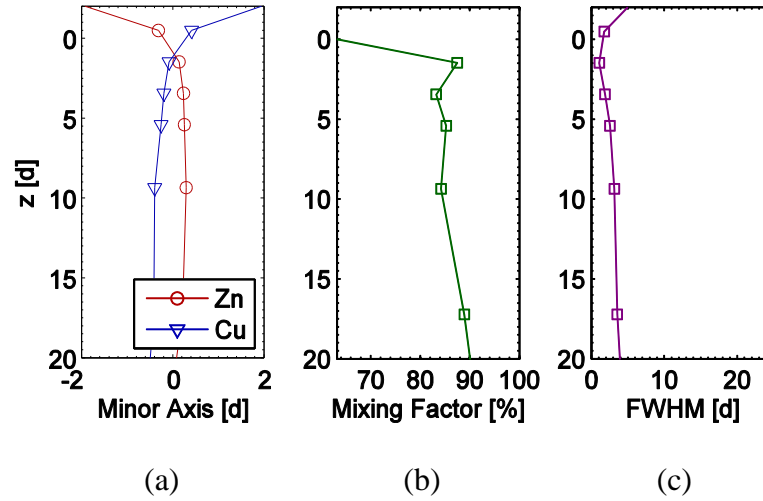


Figure A2-24. Condition 24, orifice diameter of 0.5 mm, impingement angle of 90 degrees, free jet length of 11 diameters, Reynolds number of 3100, and Weber number of 260.

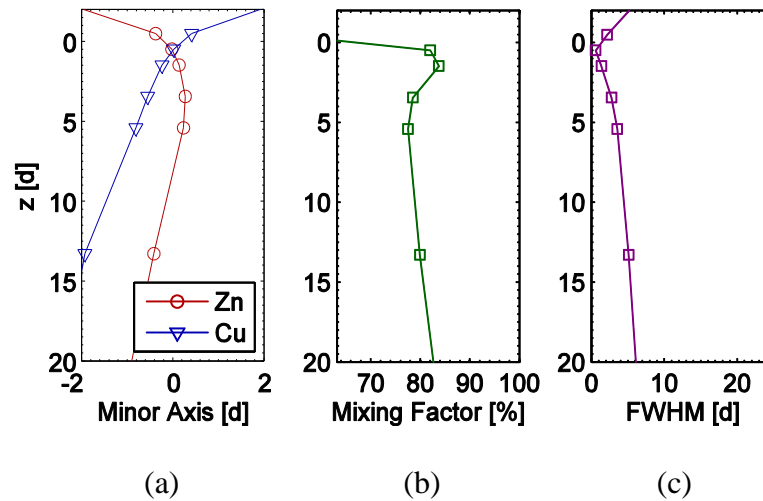


Figure A2-25. Condition 25, orifice diameter of 0.5 mm, impingement angle of 90 degrees, free jet length of 11 diameters, Reynolds number of 4700, and Weber number of 590.

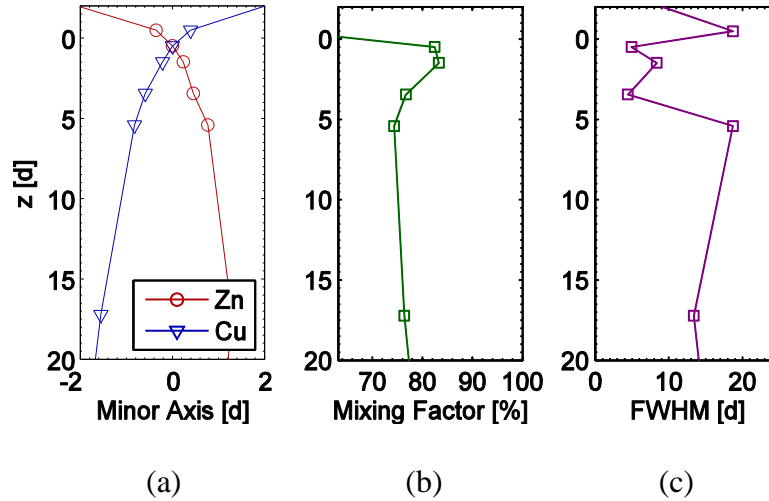


Figure A2-26. Condition 26, orifice diameter of 0.5 mm, impingement angle of 90 degrees, free jet length of 11 diameters, Reynolds number of 6200, and Weber number of 1000.

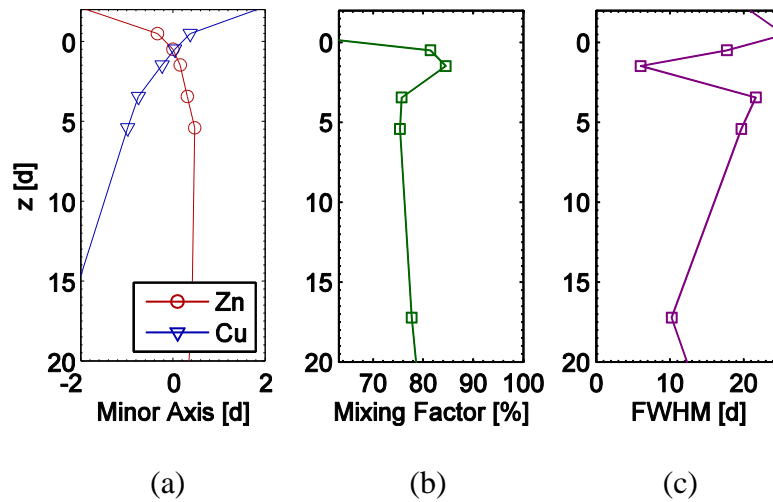


Figure A2-27. Condition 27, orifice diameter of 0.5 mm, impingement angle of 90 degrees, free jet length of 11 diameters, Reynolds number of 9400, and Weber number of 2300.

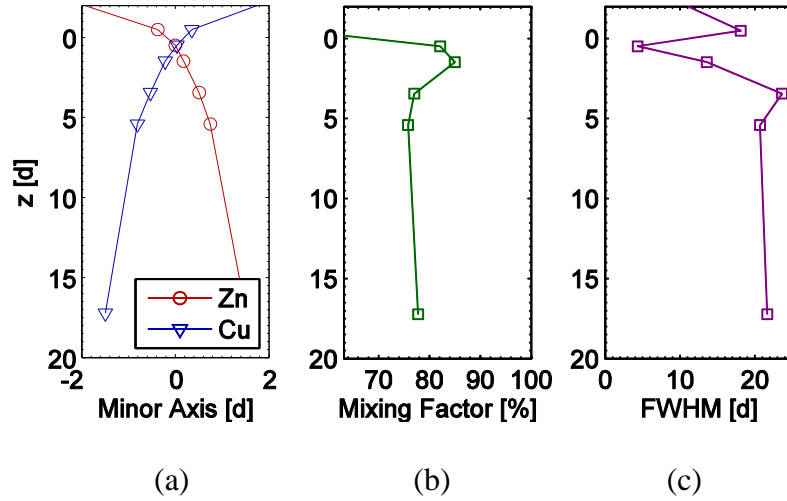


Figure A2-28. Condition 28, orifice diameter of 0.5 mm, impingement angle of 90 degrees, free jet length of 11 diameters, Reynolds number of 11700, and Weber number of 3700.

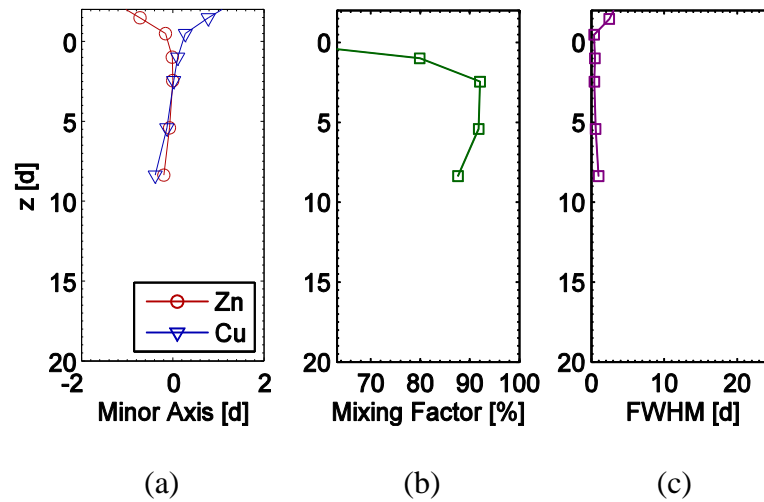


Figure A2-29. Condition 29, orifice diameter of 1.0 mm, impingement angle of 60 degrees, free jet length of 12 diameters, Reynolds number of 3100, and Weber number of 130.

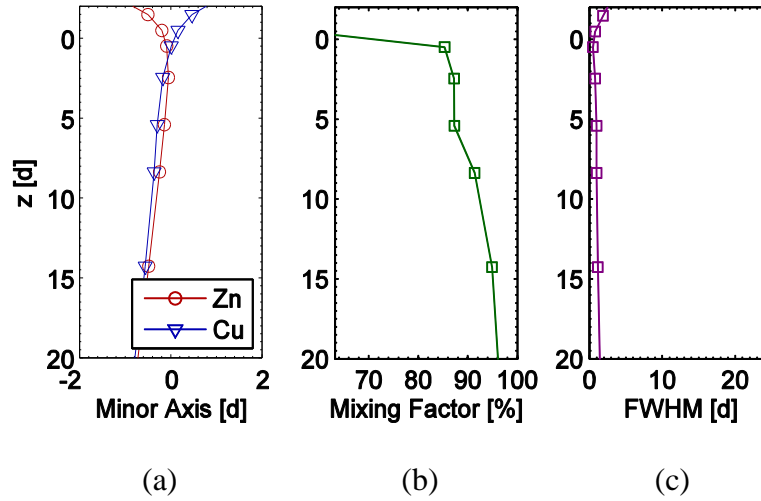


Figure A2-30. Condition 30, orifice diameter of 1.0 mm, impingement angle of 60 degrees, free jet length of 12 diameters, Reynolds number of 4700, and Weber number of 290.

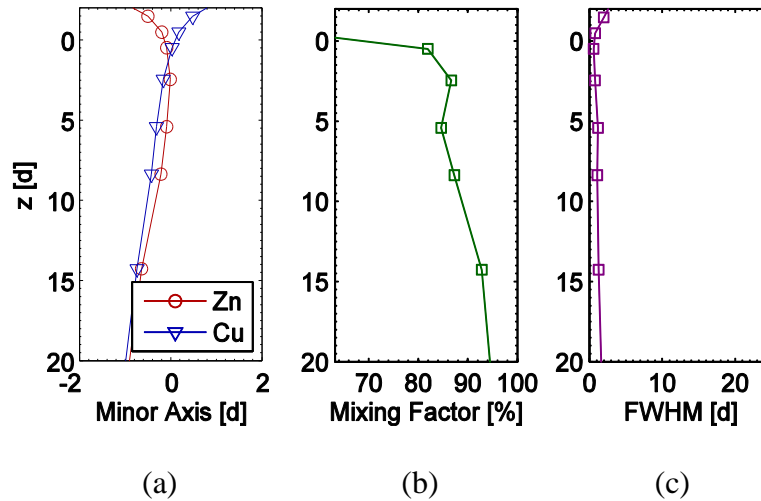


Figure A2-31. Condition 31, orifice diameter of 1.0 mm, impingement angle of 60 degrees, free jet length of 12 diameters, Reynolds number of 6200, and Weber number of 520.

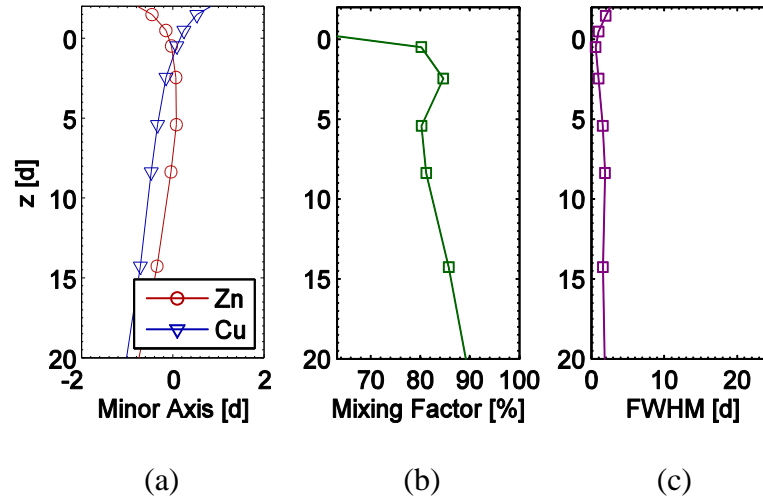


Figure A2-32. Condition 32, orifice diameter of 1.0 mm, impingement angle of 60 degrees, free jet length of 12 diameters, Reynolds number of 9400, and Weber number of 1200.

APPENDIX B

SPRAY SYSTEM STANDARD OPERATING PROCEDURE

Analysis of Hazards

- 1. Pressure Hazards:** The HPSS will be leak tested to 2000psi, and will be run at 1500psi. The components of the gas handling system include gas pressure regulators, valves, safety valves, and fittings. Remediation of this hazard is documented below in “Implementation of Hazard Controls”, Section 1.
- 2. Chemical Hazards:** Potassium iodide may be used as a contrast enhancement agent, and the following metal salts will be dissolved in water and the metal ions excited for fluorescence measurements; Cobalt Nitrate, Cobalt Sulfate, Cupric Nitrate, Cupric Sulfate, Nickel Nitrate, Nickel Sulfate, Zinc Nitrate, and Zinc Sulfate. Gelling agent, hydroxypropyl cellulose will be used for gel spray experiments. While the gases used in these experiments are all inert, they pose a risk of asphyxiation if not properly exhausted from the hutch. Moreover, the beryllium window on the energy-dispersive detector is fragile and can be broken if mishandled. Remediation of this hazard is documented below in “Implementation of Hazard Controls”, Section 2.
- 3. Noise Hazards:** At high gel flow rates and when leak testing the HPSS, the pressures will reach 2000psi. These pressures will need to be purged during the leak test and to refill the HPSS. Remediation of this hazard is documented below in “Implementation of Hazard Controls”, Section 3.
- 4. X-Radiation Hazards:** The x-ray facilities contain areas of potential radiation exposure, there are several controlled areas, and radioactive sources may be present.

Remediation of this hazard is documented below in “Implementation of Hazard Controls”, Section 4.

5. **Mechanical Hazards:** The x-ray facilities contains a number of trip hazards and head hazards. It is also shared laboratory space in which sharp glass and metal objects are frequently used by other experimenters. Remediation of this hazard is documented below in “Implementation of Hazard Controls”, Section 5.

6. **Electrical Hazards:** The electrical equipment to be used is all wall powered 120 volt AC. The HPSS valves are run on 24 volt DC, and the monitoring equipment (linear potentiometers and pressure sensors) run on 12 volt DC. Remediation of this hazard is documented below in “Implementation of Hazard Controls”, Section 6.

Implementation of Hazard Controls

1. Pressure Hazards

- The HPSS is be fitted with an ASME rated, non-adjustable pop safety valve with a rating of 2000 psig, which is less than the lowest pressure rating of the components in the high pressure spray system.
- Pressurization of the HPSS will be performed from outside the hutch, minimizing the risk to workers if a component of the system fails.
- The stored energy of HPSS has been minimized by reducing the gas volume that will be under pressure. The volume under pressure will consist of supply lines, fittings, valves, flow meters, and the nozzle supply tube.
- Shop air used to open and close the high pressure ball valves will not exceed 90 psi.

- Pressure tests have been performed for the LVDT seal, tested to 1.5 times working pressure (3000 psi) and the pressurized cylinders, tested to 1.5 times working pressure (6000 psi).
- All other fittings are Swagelok or Parker, and are stainless steel.
- A 185 psi, ASME Stamped, pressure tank is used to load gel into the pressurized cylinders, when the cylinders are at ambient pressure. The 185 psi pressure tank also stands as a backup for pump failure. The gear or diaphragm pump can be replaced with the pressure tank.
- Workers will wear approved safety glasses and face shields while near the gas handling system.

2. Chemical Hazards

- Nitrogen asphyxiation may occur when continuously running the HPSS due to the purging frequency. Running at the highest rate the system will be purged every 5 minutes, the dead volume of Nitrogen to be purged is 275L. This equates to 2 cfm far less than the capacity of the exhaust system (1200 cfm), ensuring that the gases in this experiment will not build up in the hutch.
- Pressurization of the HPSS will occur from outside the hutch, minimizing the exposure of workers to the gases.
- Potassium Iodide may be used in the course of the experiments. The Appendix contains the MSDS for every chemical used.
- Zinc Nitrate will be used in the course of the experiments. The Appendix contains the MSDS for every chemical used.

- Cupric Nitrate will be used in the course of the experiments. The Appendix contains the MSDS for every chemical used.
- Cobalt Nitrate will be used in the course of the experiments. The Appendix contains the MSDS for every chemical used.
- Iron Nitrate will be used in the course of the experiments. The Appendix contains the MSDS for every chemical used.
- Nickel Nitrate will be used in the course of the experiments. The Appendix contains the MSDS for every chemical used.
- Workers will exercise care in the handling of the detector. If any breakage of the beryllium window occurs, workers will immediately exit the hutch and report the incident to APS and ES ESH personnel.
- Cab-O-Sil M5 and hydroxypropylcellulose are used to make gels. MSDS's can be found in the Appendix.
- Slic-Tite PTFE is used as pipe dope, MSDS can be found in Appendix.
- Copper anti-seize and silicone grease are used to lubricate the HPSS, MSDS's can be found in the Appendix.

3. Noise Hazards

- The HPSS will be pressurized while personnel are present to conduct a leak test, to ensure safety and accuracy of results. The leak test procedure can be found in the Procedures section.
- While running the gel sprays the HPSS will need to be routinely filled and cleaned, this process can be found in the procedures section, and the pressurized nitrogen will occur inside the hutch while the doors are closed and no personnel are present.

- During normal operating conditions the high pressure nitrogen will be purged through Swagelok mufflers. However the high pressure relief valves are not muffled and release directly to the environment.
- Hearing protection will be available at the hutch if the experiment produces excessive noise. All workers have been trained in the correct use of hearing protection PPE.

4. X-Radiation Hazards

- All experimenters have been trained as APS users and have received Sector Orientation. All radiation control measures shall be strictly followed.

5. Mechanical Hazards

- The APS hutch contains a number of trip hazards and head hazards. Before setup of our equipment begins, a thorough inspection of the hutch will be made by the experimenters. Trip hazards will be minimized, head hazards will be padded, and any sharp objects will be removed from the hutch.

6. Electrical Hazards

- The equipment will go through a thorough inspection prior to being operated inside the hutch

Procedures

Mixing Solution (contrast enhancing agent or metal salt)

1. Don PPE: safety glasses, nitrile gloves
2. Setup mixing station.
 - a. Place near water source
 - b. Plug in scale and mixer
3. Measure out one Liter of water using the scale

- c. Add water to mixing bowl
- 4. Measure out appropriate amount of KI using the scale

Setting up and Running Liquid Spray Equipment

- 1. Secure spray tank to the translation stage
- 2. Secure injector in spray tank, and align with source and detector.
- 3. Secure flow meter, if applicable
- 4. Plumb spray tank outlet to liquid pump inlet, plumb pump to injector, ensure tight connections.
- 5. Add liquid to chamber
- 6. Static leak test; tighten any leaking connections
- 7. Connect electrical; plug pump into wall and turn pump on.
- 8. Dynamic leak test
 - a. If a connection leaks turn off pump
 - b. Tighten leaky connection
 - c. Turn pump on and continue search for leaking connections.

Mixing Gel

- 1. Don PPE: safety glasses, nitrile gloves
- 2. Setup mixing station.
 - a. Place near water source
 - b. Plug in scale and mixer
 - c. Connect vacuum chamber and pump, and plug in pump
- 3. Measure out one Liter of water using the scale
 - a. Add water to mixing bowl

4. Measure out appropriate amount of gel using the scale
 - a. Add small amounts of gel at a time to mixing bowl as the gel is stirred in.

High Pressure Leak Test

1. This procedure requires two people to be present. The first person controls the system pressure, while the second person inspects the system for leaks.
2. Double check all connections
3. Aware personnel
4. Don PPE: safety glasses, face shield, ear protection
5. Ensure the pistons are removed from the cylinders, and cap the gel lines prior to the injector. This is done to ensure all lines in the system are leak tested.
6. Set valves: Main Valves open, Pressure Valves Open, and Vent Valves Closed
7. Start with system at atmospheric pressure.
8. Increase pressure by 50 psi, check every connection with soapy water.
 - a. If any connections leak,
 - i. Purge system: stop flow of gas from tank to High Pressure Spray System, then open Vent Valves.
 - ii. Tighten any loose connections.
 - iii. Restart at Step 7.
 - b. If no connections leak repeat Step 8 until system holds 1600psi for high pressure lines or 90psi for low pressure lines.

Filling and Refilling High pressure Spray System with Gel

1. The 185 psi pressure tank is used to fill the HPSS.

2. Ensure the Pressure Valves from the high pressure source are closed, the Vent Valves are open and the Main Valves leading to the injector are closed. The spray system is at equilibrium with the environment for the exception of the supply lines.
3. Add appropriate amount of gel to 185 psi pressure tank, secure lid.
4. Connect the 185 psi pressure tank to the pressure line. Adjust pressure to the 185 psi pressure tank to push the gel into the cylinders. Use LVDT's as a reference to ensure a complete filling of both cylinders.
5. Once both cylinders have been filled close all three valves connecting the 185 psi pressure tank to the high pressure gel lines.

Setting up and Running HPSS

1. Equipment and personnel are allowed inside the hutch.
2. Secure spray tank to the translation stage.
3. Secure injector in spray tank, and align with source and detector.
4. Assemble the HPSS in final location with feet extended to the ground
5. Connect the pressure transducers and LVDT's to the data acquisition board.
6. Plumb spray tank outlet to collection bucket and ensure tight connections.
7. Plumb exhaust, or secure muffler.
8. Plumb gel loading pump.
9. Plumb low pressure (90psi) lines to shop air
 - a. Once lines are connected open valve
 - b. Spray connections with soapy water to
10. Plumb high pressure (2000psi) lines to nitrogen bottle
11. Cap injector lines prior to injector.

12. Connect the pneumatic valve control box.
13. Close the vent valve, close the pressure valves, open the main valves
14. Leak test high pressure lines to 2000psi using High Pressure Leak Test procedure.
15. Return the HPSS to atmospheric pressure, with the exception of the high pressure supply lines. Exhaust valve open, pressure lines closed, main valves open
16. Uncap injector lines and plumb to injector.
17. Close main valves
18. Fill high pressure cylinders following procedure.
19. Search and close the hutch.
20. Close vent valves, close main valves, close pressure valves.
21. Set supply lines to desired pressure, when the pressure valves are opened the system will be ready to discharge, when the main valves are opened the gel will flow to the injector. The main valves can be operated by either circuit; the control box or through the in house control system.
22. The HPSS is ready for use.
23. Flow gel for the desired experiment.
24. When gel cylinders are empty, close main valves (both circuits must be open), close pressure valves, open exhaust valves system line pressure will drop to atmosphere as dead volume is released through the mufflers.
25. Start back at Step 17 to continue flowing gel.